TECHNISCHE UNIVERSITÄT MÜNCHEN

TUM School of Natural Sciences

Functional ligands for optimization of device performance and stability of perovskite solar cells

Yuqin Zou

Vollständiger Abdruck der von der TUM School of Natural Sciences der Technischen Universität München zur Erlangung des akademischen Grades einer

Doktorin der Naturwissenschaften (Dr. rer. nat.)

genehmigten Dissertation.

Vorsitz: Prof. Dr. Andreas Weiler
Prüfer der Dissertation:
1. Prof. Dr. Peter Müller-Buschbaum
2. Prof. Dr. Aliaksandr Bandarenka

Die Dissertation wurde am 03.05.2023 bei der Technischen Universität München eingereicht und durch die TUM School of Natural Sciences am 23.05.2023 angenommen.

Abstract

Metal halide perovskite solar cells (PSCs) have been intensively developed due to their excellent optoelectronic properties and show great development prospects. However, the detrimental defects present in the perovskite films could trap charge carriers and act as attachment sites for oxygen and water molecules to penetrate the active layer of perovskite, compromising the final device performance and long-term operational stability. In this thesis, several effective additives are adopted to modify the surface of the active layer and incorporate them into the bulk of the perovskite layer, to passivate the detrimental defects in the thin films and improve the device performance and its long-term stability. Grazing-incidence small-angle/wide-angle X-ray scattering (GISAXS/GIWAXS) are used as important characterization methods to investigate the effect of additives on perovskite grain orientation and its film morphology and to observe the variation in perovskite crystal structure and crystal morphology of perovskite solar cells under operational conditions. This thesis investigates the relationship between grain orientation and charge carrier dynamics in thin films and dissects the degradation mechanisms of PSCs based on different grain orientations under operational conditions, which could provide insights for achieving higher efficiency and stability of PSCs.

Zusammenfassung

Metallhalogenid-Perowskit-Solarzellen wurden aufgrund ihrer hervorragenden optoelektronischen Eigenschaften intensiv entwickelt und weisen große Entwicklungsperspektiven auf. Die in den Perowskitfilmen vorhandenen schädlichen Defekte könnten jedoch Ladungsträger einfangen und als Anlagerungsstellen für Sauerstoff- und Wassermoleküle dienen, um in die aktive Perowskitschicht einzudringen, wodurch die endgültige Leistung und die langfristige Betriebsstabilität beeinträchtigt werden. In dieser Dissertation werden mehrere wirksame Additive verwendet, um die Oberfläche der aktiven Schicht zu modifizieren und sie in das volumen der Perowskitschicht einzubauen, um die schädlichen Defekte in den Dünnschichten zu passivieren und die Leistung und ihre Langzeitstabilität zu verbessern. Kleinwinkel-/Weitwinkel-Röntgenstreuung unter streifendem Einfall (GISAXS/GIWAXS) werden als wichtige Charakterisierungsmethoden verwendet, um die Wirkung von Additiven auf die Perowskit-Kornorientierung und seine Filmmorphologie zu untersuchen und die Variation der Perowskit-Kristallstruktur und Kristallmorphologie von Perowskit-Solarzellen unter Betriebsbedingungen zu beobachten, indem GIWAXS

und GISAXS in-situ genutzt werden. Diese Arbeit zielt darauf ab, die Beziehung zwischen Kornorientierung und Ladungsträgerdynamik in dünnen Filmen zu untersuchen und den Degradationsmechanismus von PSCs basierend auf unterschiedlichen Kornorientierungen unter Betriebsbedingungen zu analysieren, was einige einfache Erkenntnisse für das Erreichen einer höheren Effizienz und Stabilität von PSCs liefern könnte.

Contents

List of abbreviations

DWBA:	distorted wave Born approximation
LMA:	local monodisperse approximation
FTIR:	Fourier transformed infrared spectroscopy
ITO:	Indium-doped tin oxide
GISAXS:	grazing incidence small angle X-ray scattering
GIWAXS:	grazing incidence wide angle X-ray scattering
SEM:	scanning electron microscopy
AFM:	atomic force microscopy
XPS:	x-ray photoelectron spectroscopy
UPS:	ultraviolet photoelectron spectroscopy
XRD:	x-ray diffraction
PL:	photoluminescence
TRPL:	time-resolved fluorescence
TAS:	transient absorption spectroscopy
UV-vis:	ultraviolet-visible absorption spectra
TPV:	transient photovoltage
TPC:	transient photocurrent
OCVD:	open circuit voltage decay
EIS:	ectrochemical impedance spectroscopy
SCLC:	space-charge-limited current
VBM:	valence band maximum
CBM:	conduction band minimum
J-V:	current density-voltage curve
J_{SC}:	short circuit current
V_{OC}:	open circuit voltage
FF:	fill factor
PCE:	power conversion efficiency
MPP:	maximum power point
Li-TFSI:	lithium bis(trifluoromethane)-sulfonimide
PCBM:	[6,6]-Phenyl C_{61} butyric acid methyl ester
PTAA:	poly[bis(4-phenyl)(2,4,6-trimethylphenyl)amine
TBP:	4-tert-butylpyridine
HBL:	hole blocking layer
EBL:	electron blocking layer
DMF:	*N*, *N*-dimethylformamide
DMSO:	dimethyl sulfoxide
CB:	chlorobenzene

1 Introduction

Global energy shortage has always been a key and hot topic of great concern to all sectors of society. As human beings made great achievements and significant leaps in social, economic, and technology, the ensuing global energy crisis and environmental pollution problem have gradually come into the limelight and triggered intense discussions. On the one hand, non-renewable energy sources such as natural gas, crude oil, and coal are being exhausted and global storage is shrinking, which is difficult to meet the future needs of the sustainable development of global human beings. Moreover, the use of these non-renewable energy sources causes serious environmental pollution. The massive emission of greenhouse gases has caused climate change, melting glaciers, and threatening animals living in the Arctic and Antarctic. On the other hand, soaring energy prices have put a lot of pressure on the daily lives of people, it is difficult for people with meager incomes to pay record-high energy fees. In addition, while the smart life brings convenience to people's lives, it also invariably increases their dependence on electricity. The high energy price will undoubtedly cause inconvenience in their daily life.

Developing clean and renewable energy sources to gradually replace the consumption of non-renewable energy has become an important strategy to promote the adjustment of the energy structure and cope with climate deterioration. Common renewable energy such as hydroelectricity, wind power, solar energy, bioenergy (biogas), geothermal energy, etc., have attracted the attention of many countries and are being vigorously developed according to geographical locations and environmental conditions. Among them, wind power and solar photovoltaic power generation are developing rapidly and are being commercialized on a large scale. These renewable energy sources have a higher replenishment rate than consumption rate and produce less pollution to the environment. Therefore, the development and utilization of renewable energy are gaining increasing attention in many countries, especially from these countries that are facing energy shortages.

Solar photovoltaics is to use the photovoltaic effect of semiconductor materials to convert light into electricity. [1] When photos impinge on metals or semiconductors, the electrons absorb energy and are released from the surface of the metal or semiconductor. These electrons are attracted towards positively charged plate and produce photoelectric

current. In 1954, the Bell Laboratory in the United States fabricated monocrystalline silicon solar cells and achieved a photoelectric conversion efficiency (PCE) of 6 %. [2]

In recent years, with the continuous exploration in the field of solar cells. The efficiency of solar cells has achieved a tremendous development. According to the composition of materials, solar cells can be mainly classified into the following categories:

The first-generation silicon-based solar cells, mainly refer to solar cells with monocrystalline silicon, polycrystalline silicon, and amorphous silicon as light-absorbing. They are the solar cells with the most mature technology and have relative high-efficiency conversion at present. The efficiency reported by the laboratory is over 26 % and has been commercialized. [3, 4] The high efficiency of silicon-based solar cells relies on high-purity silicon materials, which are expensive. At present, with the continuous improvement in processing technology, the manufacturing cost decreases a lot.

The second-generation multi-compound thin film solar cells, mainly include gallium arsenide (GaAs), indium phosphide (InP), copper indium gallium selenide (CIGS), and cadmium telluride (CdTe) solar cells. [5] These cells have high photoelectric conversion efficiency, stable device performance, and thin light-absorbing layer, which greatly reduce the consumption of raw materials. The active layers of most multi-compound thin film solar cells contain some rare elements and heavy metals, which limit the large-scale production and commercial application. [5–7]

The third-generation is the new type of solar cells, mainly including perovskite solar cells, dye-sensitized solar cells, organic solar cells, quantum dot solar cells, etc. This type of solar cells has abundant raw material storage, low materials and fabrication costs, high power conversion efficiency, and could achieve flexible solar cell manufacturing. Among these new types of solar cells, perovskite solar cells exhibit excellent optoelectronic properties, such as long charge carrier diffusion length, tunable band gap, high light absorption coefficient, as well as can be fabricated into the single-junction and multi-junction solar cell architecture, which show huge development prospects and are considered as the most promising solar cells. At present, the highest efficiency of single-junction cells reported in the laboratory is 25.7 %, [8] which is gradually approach the highest efficiency of silicon-based cells. [3]

PSCs are a class of solar cells that use metal halide perovskite materials as the light-absorbing layer. In 2009, it was used as a sensitizer in dye-sensitized solar cells and achieved a power conversion efficiency (PCE) of 3.8 %. [3] In 2011, Park et al. prepared $CH_3NH_3PbI_3$ into 2-3 nm nanocrystals and used it in dye-sensitized cells, achieving a PCE of 6.5 %. [9] In 2012, Kim et al. introduced solid-state hole transport material (Spiro-OMeTAD) into PSCs and prepared the first all-solid-state perovskite solar cell with a

PCE of 9.7 %. [10] In 2013, Gratzel et al. adopted a two-step deposition method to prepare perovskite thin films and achieved a PCE of more than 15 %. [11] In 2014, Yang et al. improved the PCE to 19.3 % by using Y to modify the TiO_2 surface. [12] In 2017, Seok et al, introduced additional iodide ions into the organic cation solution to form the perovskite layers through an intramolecular exchanging process, and achieved a certified PCE of 22.1 % in small cells and 19.7 % in 1-square-centimeter cells. [13] With the deep research of perovskite solar cells, the highest certified efficiency reported by perovskite solar cells is as high as 25.7 % today. [8]

The rapid development achieved in perovskite solar cells shows great development prospects and commercial value. But the perovskite materials are unstable and easily degrade by chemical reaction or ions diffusion between functional layers when exposed to moisture, oxygen, and heat conditions. [14–16] Moreover, it still has a distance to achieve the theoretical efficiency. In the future development, the research of PSCs mainly focuses on achieving high-efficiency approaches to the Schockley-Queisser limit, [17] achieving large-scale commercial applications, and improving the long-term stability of perovskite solar cells operated under ambient conditions. At present, many effective methods, such as tuning the perovskite component and modifying the interface of the charge blocking layer or perovskite active layer, designing and developing new film formation methods, as well as optimizing the film morphology, [18–20] have been devoted and achieved remarkable achievements in device efficiency and stability.

In addition to the above-mentioned approaches to optimize device stability, a more in-depth understanding of the degradation mechanism is also important. Tracking the crystal structure and film morphology evolution of device under operating conditions is crucial to the exploration of degradation mechanism, which could provide new insights for adopting appropriate and effective measures to improve device stability. Additionally, the intrinsic link between the crystal orientation and the charge carrier kinetics is also needs to paid attention to achieve better photovoltaic device performance.

The main goals of the present thesis is to address the improvement of methylammonium lead iodide ($MAPbI_3$, denoted as MAPI)-based device stability, the regulation of crystallization behavior and crystal orientation during film formation, and the tracking of the crytsal structure and film morphology evolution occurring on the PSCs under operating conditions. In this thesis, Chapter 2 introduces the theoretical background, including the crystal structure of perovskite, the working principles and parameter characterization of perovskite solar cells, the stability of perovskite materials, and the basic principles of X-ray scattering methods used to study the perovskite thin film structure. Chapter 3 introduces some characterization methods used in this thesis. Chapter 4 introduces the

preparation methods of perovskite thin films and the corresponding devices involved in this thesis. Followed by the research results discussed in chapter 5 to chapter 7.

The degradation of the perovskite component starts from the up to the bottom of the active layer, so the resistance of the upper interface to ambient conditions is crucial to the stability of the PSCs. Moreover, the interface recombination and charge carrier transport losses occurring at the interface also effect the charge carrier extraction efficiency, thus impair the device performance of the perovskite solar cells. Therefore, in chapter 5, an anionic surfactant, sodium dodecylbenzene sulfonate (SDBS), is used to optimize the upper interface of MAPI. The SDBS located at grain boundaries and the surface of the active layer can passivate un-coordinated lead ions, stabilize the cubic phase of the perovskite film, as well as protect the perovskite components from water-induced degradation.

In addition to the grain boundaries and the defects at the interface that could cause charge carrier loss, the crystal orientation of perovskite crystal is also correlated to the charge carrier kinetics of polycrystalline materials, which will affect the photocarrier transport across the absorber and relative interface, as well as the subsequent photovoltaic performance of PSCs. [20] Then, in chapter 6, the relationship between the crystal orientation distribution and the charge carrier dynamics in the device is explored by constructing CsBr-doped mixed-cation perovskite phases. By GIWAXS measurements, the crystal orientation is studied. It shows that the introduction of CsBr modulate the crystal orientation distribution of perovskite crystal during crystallization, and affect the extraction and transport properties of photogenerated charge carriers.

As mentioned above, the inhibition of perovksite degradation is essential to its stability and commercial application. Tracking the crystal structure and morphology variation of perovskite films under operating conditions is meaningful and could provide new insights into the degradation mechanism. In chapter 7, GISAXS and GIWAXS are used to investigate the effects of ionic liquids on the crystallization behavior of thin films from a microscopic perspective, and track the changes in crystal structure and morphology of ionic liquid-containing devices under operation. Additionally, the stability of PSCs under different conditions is also explored.

The final chapter 8 summarize the major findings of this thesis and gives a brief outlook for further studies.

2 Theoretical Background

This chapter introduces the theoretical background of materials, devices, and characterizations conducted in this thesis, mainly including the crystal structure of the perovskite, the working principle of the perovskite solar cells, parameter characterization of perovskite solar cells, stability of perovskite materials and X-ray scattering.

2.1 The perovskite crystal structure

The ideal perovskite crystal formula is ABX_3, which is generally a cubic or octahedral structure, as shown in the Figure 2.1.

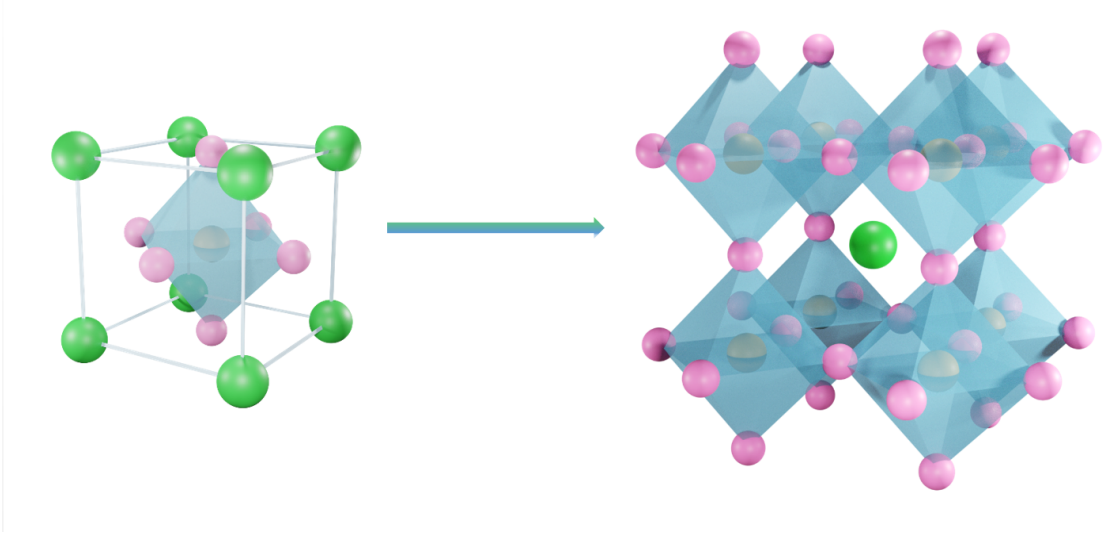

Figure 2.1: Crystal structure of cubic perovskite with molecular formula ABX_3

In PSCs, the A ions usually refer to organic amine cations or alkali metal ions, such as $CH_3NH_3^+$ (MA^+) ($R_A = 0.180$ nm), $NH_2CH{=}NH_2^+$ (FA^+)($R_A = 0.230$ nm) and Cs^+. B ions refer to divalent metal cations, mainly Pb^{2+} ($R_B = 0.119$ nm) and Sn^{2+} ($R_B = 0.110$ nm). X ions are halogen anions, namely I^- ($R_X = 0.220$ nm), Cl^- ($R_X = 0.181$ nm), and Br^- ($R_X = 0.196$ nm). The ABX_3 structure can be approximately regarded as the result

of close packing. In the cubic close packing arrangement, A and X are arranged according to the cubic close packing. In the crystal structure of perovskite, B ions are located at the center of the octahedron and coordinate with X ions to form [BX_6] octahedrons with a coordination number of 6. X ions are located at the 6 vertices of the octahedron with a coordination number of 2, and there are two B ions adjacent to it. Ions fill the center of the voids between the octahedra, surrounded by 12 X ions to form a coordination cuboctahedron [AX_{12}] with a coordination number of 12.

Adjacent octahedrons form an extended spatial three-dimensional network structure through common vertices. Therefore, such classic perovskite materials are also called three-dimensional perovskite materials. For perovskite materials, the tolerance factor t and the octahedral factor μ are the important parameters to evaluate whether it maintains a stable ABX_3 structure

$$t = \frac{R_A + R_X}{\sqrt{2}(R_B + R_X)}, \mu = \frac{R_B}{R_X} \tag{2.1}$$

where R_A, R_B, and R_X refer to the radii of A ion, B ion, and X ion, respectively. Usually, when 0.81<t<1.11 and 0.44< μ <0.90, the ABX_3 compound is a perovskite structure. [21] The greater the gap between t and 1, the greater the lattice distortion, and the crystal gradually becomes tetragonal or even orthorhombic. [22, 23] When t=1, the crystal is a cubic lattice with the highest symmetry (α phase). When t is between 0.89 and 1.00, the lattice is a rhombohedral structure (trigonal system). when t <0.96, the symmetry changes to an orthorhombic structure. [24] Additionally, under external conditions such as temperature, electric field, and pressure, the perovskite materials also undergo transitions in the crystal structure. Generally, as the temperature decreases, the crystal structure will change to a low-symmetry crystal form. When temperatures are below 165 K, the perovskite structure is an orthorhombic phase. When the temperature is between 165 K and 327 K, the perovskite exhibits a tetragonal phase. When the temperature is increased to 327 K, the disorder of the molecules increases, and the perovskite exhibits a cubic phase . [22, 23] Besides, organic-inorganic hybrid perovskites are also common and widely used perovskite components, which combine the respective advantages of organic and inorganic materials.

2.2 The working principle of perovskite solar cells

Perovskite solar cells are composed of electrodes, charge-blocking layers, and the perovskite active layer. The working principle is shown in Figure 2.2. [25]

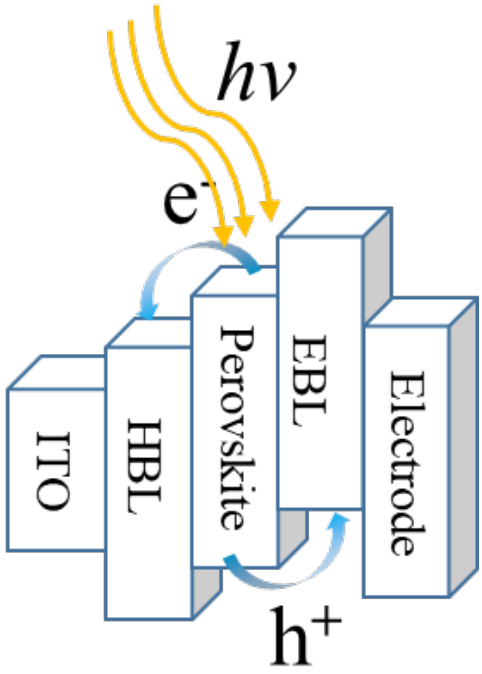

Figure 2.2: Schematic diagram of the working principle of perovskite solar cells

Under light, perovskite material absorbs photons and generates excitons, that is, a pair of electron and hole which are attracted through electrostatic interactions to form a bound state. Due to the low exciton binding energy of perovskite materials, under operating conditions of perovskite solar cells, most excitons generated in the photoactive layer are separated into free charge carriers: electrons and holes. [26] Due to the quasi-Fermi energy level being different in the p-n junction, grain boundaries, and semiconductor interface, a built-in electric field is created. The generated electrons and holes will drift in opposite directions under the effect of the built-in electric field. [26] These free charge carriers are transported through the perovskite active layer and into the charge blocking layer: electron blocking layer(ETL) and hole blocking layer (HBL). The extracted charge carriers are further collected by the corresponding electrodes. [27] It is the energy gradient between the materials inside the device and the built-in electric field that ensure the electrons and holes follow their respective transport paths to the external circuit, thus creating a potential difference between the two electrodes and subsequently forming a photocurrent. [26, 27]

During the operation of perovskite solar cells, in addition to the generation and transport of the charge carriers, charge carrier recombination also occurred in the bulk and on the interface of perovskite materials.

The charge carriers recombination process that occurs in the perovskite layer is mainly divided into monomolecular recombination, bimolecular recombination, and Auger recombination according to the kinetics characteristics. [26, 28]

$$\frac{dn}{dt} = -k_1 n - k_2 n^2 - k_3 n^3 \tag{2.2}$$

where n refers to photogenerated charge carrier concentration, k_1, k_2, and k_3 refers to the rate constant of monomolecular recombination, bimolecular recombination, and Auger recombination, respectively. Monomolecular recombination is the most dominant form of charge carrier recombination in perovskite materials, and usually refers to trap-assisted recombination. [29] That is, the trap in the material captures free carriers and releases energy through crystal vibration and other ways, mostly belonging to non-radiative recombination. Although most of the trap energy levels in perovskite materials are located near the conduction band minimum or valence band maximum. [30] But there are also some traps with deeper energy levels that become trap states for trapping charge carriers. Their energy level depth, density, distribution, capture cross-section, and so on, affect the rate of single-molecule recombination. [31] Therefore, improving the perovskite preparation method is important to reduce the effect of trap states and inhibit the occurrence of monomolecular recombination.

Bimolecular recombination is a recombination process that occurs between free electrons and holes and releases the energy via radiative transition, so it belongs to radiative recombination. [32] In general, the rate of bimolecular recombination is much smaller than that of monomolecular recombination, and its rate constant does not depend on the preparation method of perovskite materials. [31]

Auger recombination refers to the process in which the energy released by electron-hole recombination is absorbed by another electron, and generally has little influence on perovskite solar cells under standard lighting conditions and can be ignored. [28]

The charge carrier recombination that occurs at the interface mainly includes the recombination on the perovskite grain boundary and the interface between the perovskite and the charge blocking layer. [33] In some cases, if the perovskite thin film coverage is poor, the HBL and the EBL could contact each other and occur recombination. Additionally, many defects exist on the perovskite surface, grain boundaries, and the interface between the perovskite and charge blocking layer, and acted as trap centers to induce charge carrier recombination, thus negatively affecting the device performance. [34]

Therefore, the preparation of high-quality perovskite films, passivation of grain boundaries and surface defects, and selection of better charge blocking layers are important to improve device performance.

2.3 Parameter characterization of perovskite solar cells

The performance of perovskite solar cells is usually characterized by the current density-voltage (J-V) curve under light conditions. It is obtained by applying a continuously varying external bias voltage to the solar cell and recording the current density at different bias voltages. A typical J-V curve is shown in Figure 2.3.

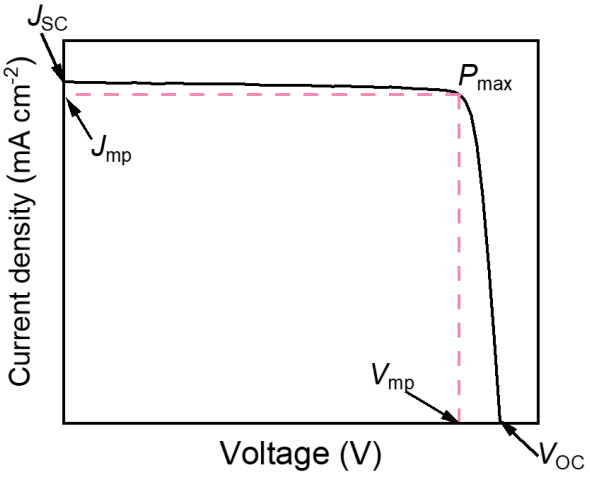

Figure 2.3: Current density-voltage curves and performance parameters of perovskite solar cells

When measured under dark conditions, the J-V curves are called dark current curve, which reflects the rectification characteristics of the solar cell as a diode. When measured under light conditions, the commonly used light conditions are AM 1.5 G simulated sunlight, the curve is the current density-voltage curve of the solar cell in the light field. For evaluating the device performance of the perovskite solar cells on the J-V curve, there are four main parameters: short-circuit current (J_{SC}), open-circuit voltage (V_{OC}), fill factor (FF), and PCE.

J_{SC}, under light conditions and no external bias voltage applied, the device is in a short-circuit state. The current density through the cell is called short-circuit current density. The main factors that affect the J_{SC} are the band gap of the perovskite material (the range of light absorption wavelengths), the thickness of the perovskite layer (the degree of light absorption), and the charge transport properties of the material itself.

V_{OC}, under light conditions, when the current through the device is zero, the device is in an open-circuit state. The voltage across the cell is called open-circuit voltage. The open-circuit voltage is mainly determined by the band gap of the perovskite material. In addition, the potential barrier between the charge blocking layer and the perovskite layer, as well as the charge carrier recombination occurring in the device, could also affect the V_{OC}.

FF, is the ratio of the maximum output power (P_{max}) per unit area of the cell to the product of the open-circuit voltage and the short-circuit current density. The fill factor is mainly affected by the series resistance (the inverse of the slope of the curve at the V_{OC} point) and the parallel resistance (the inverse of the slope of the curve at the J_{SC} point) in the solar cell. When the series resistance decreases or the parallel resistance increases, the FF increases.

$$FF = \frac{J_{mp}V_{mp}}{J_{SC}V_{OC}} \tag{2.3}$$

PCE, is the ratio of the maximum output power (P_{max}) per unit area of the device to the incident light irradiance P_{in}. PCE is the most intuitive parameter to evaluate the performance of perovskite solar cells.

$$PCE = \frac{P_{max}}{P_{in}} = \frac{J_{mp}V_{mp}}{P_{in}} = \frac{J_{SC}V_{OC}FF}{P_{in}} \tag{2.4}$$

In addition to *J-V* curves, incident photon-to-charge carrier efficiency IPCE is another important parameter characterizing device performance, defined as the ratio of the number of electrons generated by incident light irradiation on the device to the number of incident photons, which is calculated as follows

$$IPCE = \frac{N_e}{N_p}100\% = \frac{J(mA/cm^2)}{P_{in}(mW/cm^2)}\frac{1240}{\lambda(nm)}100\% \tag{2.5}$$

where N_e is the number of collected electrons, N_p is the number of incident photons, and λ is the wavelength of incident light.

IPCE reflects the utilization of devices for lights with different wavelengths and their charge carrier transfer properties. By integrating the IPCE data at different wavelengths, the short-circuit current density of the device can be obtained.

$$J_{SC} = -q\int_{\lambda_1}^{\lambda_2} IPCE(\lambda)\Phi_{ph,\lambda}d\lambda \tag{2.6}$$

where q is the fundamental charge, $\Phi_{ph,\lambda}$ is the photon flux corresponding to the wavelength.

The short-circuit current density obtained by integration can evaluate the reliability of the short-circuit current density derived from *J-V* curves. The closer the two values are, the more reliable the short-circuit current density obtained from *J-V* is.

2.4 Stability of perovskite materials

When the hybrid perovskite materials are exposed to high temperature or humidity conditions, their lattice is easily destroyed, leading to the decomposition of the perovskite material. Because perovskite materials are sensitive to temperature and humidity, thermal stability and humidity stability are the key factors that determine whether hybrid perovskite materials can be commercialized as solar cells.

2.4.1 Thermal stability of perovskite materials

As stated in Section 2.1, the tolerance factor t is an important factor that can be used to initially judge whether the perovskite structure is stable or not. When the t value is in the range of 0.78 to 1.05, a stable perovskite structure can be formed. [35] The t can be adjusted by replacing or introducing atoms with different radii to obtain a more stable crystal structure, with a consequent impact on its stability in the environment. The work lists the phase transition temperature of some perovskite crystals. [23]

When the organic cation A in perovskite structure is replaced by inorganic cations such as Cs^+ and Rb^+, the thermal stability of the perovskite materials could be greatly improved. Unlike $CH_3NH_3PbI_3$ that suffers from significant change in morphology, electrical conductivity and chemical composition after exposed to air or nitrogen conditions at 85°C for 24 h, [36] $CsPbI_3$ does not form a perovskite structure (an orthorhombic crystal system) at room temperature. But when the temperature is increased to 634 K, the orthorhombic $CsPbI_3$ undergoes a phase transition and transforms into a cubic perovskite structure. [37] The element Rb, which is homologous to Cs, also be introduced into the perovskite structure to form a stable cubic crystal of perovskite $RbPbI_3$ at high temperatures. This indicates that all-inorganic perovskite materials can withstand higher temperatures than organic-inorganic hybrid perovskite materials.

Another effective way is to replace MA ion with another organic cation formamidine ion ($HN{=}CH(NH_3)^+$). $FAPbI_3$-based devices show higher thermal stability compared to $CH_3NH_3PbI_3$-based devices. Snaith et al. placed the $FAPbI_3$ and $CH_3NH_3PbI_3$ films at 150°C for 60 min, the $CH_3NH_3PbI_3$ film degraded into yellow PbI_2 while $FAPbI_3$ retained its previous dark color, showing better thermal stability. [38] Docampo et al. performed the thermal decomposition test of perovskite containing different A cations and showed that the thermal decomposition temperature of perovskite containing FA was over 50 °C higher than that of perovskite containing MA. [39] Thus, the use of FA-based perovskite with higher thermal decomposition temperature is helpful for the thermal stability improvement of the perovskite solar cells.

2.4.2 Humidity Stability of Perovskite Materials

Wang et al. systematically investigated the effect of water vapor on the perovskite material $CH_3NH_3PbI_3$ and reported the degradation mechanism of the perovskite material. [40,41] Under humidity conditions, the water vapor dissolves the perovskite, the $CH_3NH_3^+$ cation is deprotonated by H_2O to generate CH_3NH_3I, a mixture of CH_3NH_2 and HI. HI, on the one hand, can react with O_2 to generate H_2O and I_2. On the other hand, HI itself is unstable and easily decomposed to H_2 and I_2. Therefore, once the water vapor is absorbed by $CH_3NH_3PbI_3$, the subsequent decomposition reaction will proceed spontaneously, the corresponding chemical reaction equation is shown below

$$CH_3NH_3PbI_3(s) \rightleftharpoons PbI_2(s) + CH_3NH_3I(aq), \quad (1a)$$

$$CH_3NH_3I(aq) \rightleftharpoons CH_3NH_2(aq) + HI(aq), \quad (1b)$$

$$HI(aq) + O_2(g) \rightleftharpoons 2I_2 + 2H_2O(l), \quad (1c)$$

$$2HI(aq) \rightleftharpoons 2H_2(g) + I_2(s). \quad (1d)$$

Figure 2.4: Chemical reaction equation under moisture condition. [41]

where s stands for solid state, aq stands for aqueous solution, l stands for the liquid state, and g stands for the gas state.

From the above decomposition reaction equation, it is clear that besides H_2O, O_2 and UV light are also important influencing factors for the decomposition of perovskite. They indicated that there are two pathways for HI decomposition: (1) reaction with O_2, see Figure 2.4c. (2) decomposition under the UV light, see Figure 2.4d. The consumption of HI accelerates the whole decomposition reaction.

To improve the stability of the perovskite material to moisture, two-dimensional materials with large groups are widely used in perovskite components. Sargent's group studied the effect of incorporating long organic chains into three-dimensional perovskites through density functional theory and found that in addition to the hydrophobic effect of long organic chains, it can also constrain organic ions and $[PbI_8]^{6-}$ octahedrons. [42] However, the doped organic long-chain molecules form a low-dimensional layered perovskite structure with low carrier mobility, resulting in difficulty in interlayer carrier migration. Therefore, devices based on two-dimensional perovskite materials exhibit lower efficiency. [43]

The degradation of perovskite materials starts from the upper interface, so the dimensionality reduction treatment of the upper interface is regarded as an effective method to treat to improve the charge carrier mobility. You et al. used PEAI organic molecules to form a thin two-dimensional perovskite layer between the perovskite layer and the charge blocking layer, which greatly increases the efficiency and stability of the device. [44]

As stated in the 2.4.1 section, compared with MA-based perovskite, FA-based perovskite has an advantage in terms of thermal stability, but its moisture stability is at a disadvantage. [45] $FAPbI_3$ has two crystal structures according to the processing temperature: the yellow hexagonal crystal structure (δ) without photosensitivity and the black trigonal crystal structure (α) with photosensitivity. The black α-type $FAPbI_3$ can be transformed from the yellow δ-type $FAPbI_3$ at a temperature of 160°C or higher. Bein et al. prepared stable α-type $FAPbI_3$ by doping a small amount of $CH_3NH_3^+$ in FA-based perovskite materials at a lower temperature. [46] Park et al. incorporated 10 % Cs^+ into $FAPbI_3$ to form $FA_{0.9}Cs_{0.1}PbI_3$ through the Lewis alkalinity of PbI_2, which greatly improve the humidity stability of the device. [47]

For the halogen X in the perovskite structure, the introduction of Br^- ions could improves the V_{OC} and the sensitivity of perovskite materials to humidity. [48–50] with the increase of Br^- content with smaller radius, the crystal structure changes from the three-dimensional distorted structure of $CH_3NH_3PbI_3$ to the regular cubic structure of $CH_3NH_3PbBr_3$. The compact stacking of the perovskite structure prevents the degradation of perovskite materials. [48–50]

By tuning the composition of perovskite materials to obtain perovskite materials with different structures, the thermal and humidity stability of perovskite materials could be improved without affecting the device efficiency.

2.5 X-ray investigation methods

X-rays are a powerful tool to investigate the crystal structure and crytsal morphology of perovskite films. In this thesis, X-ray diffraction (XRD) and GIWAXS are used for the analysis of the crytsal structure and GISAXS is used for the crytsal morphology. A brief introduction to the theoretical background and analysis of XRD is presented in Section 2.5.1, followed by a short introduction to GIWAXS and GISAXS in Section 2.5.2 and 2.5.3, respectively.

2.5.1 X-ray diffraction

The crystal can be regarded as composed of parallel atomic planes, and the diffraction rays of the crystal should also be superimposed by the diffraction rays of the atomic planes. X-rays can be irradiated not only to the crystal surface but also to a series of parallel atomic planes within the crystal. If the phase difference between the reflection rays of two adjacent crystal planes is an integer multiple of 2π (or the wave path difference is an integer multiple of the wavelength), the reflection rays of all parallel crystal planes can be uniformly strengthened, thereby obtaining diffraction in this direction. As shown in Figure 2.5, after the incident ray [LM] is irradiated to the [AA] crystal plane, the reflection ray is [MN]. Another parallel incident ray [L_1M_2] is irradiated to the adjacent crystal plane [BB], the reflection ray is [M_2N_2]. The wave path difference between the two X-rays reaching at [NN_2] is

$$\delta = PM_2 + M_2Q \tag{2.7}$$

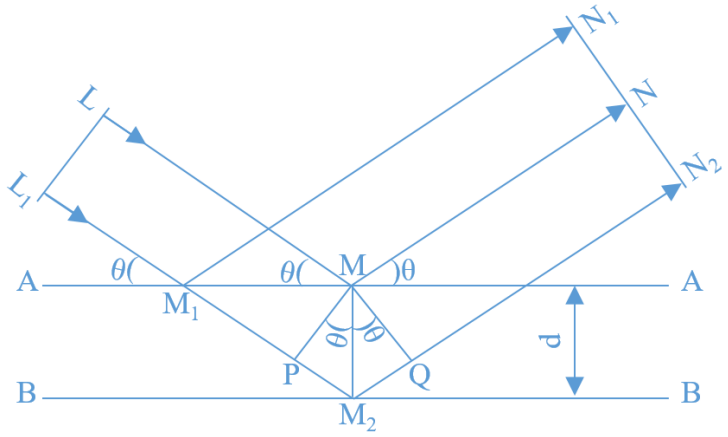

Figure 2.5: Schematic illustration of the Bragg equation

If the lattice spacing of the crystal structure is d, it can be gained from Figure 2.5

$$\delta = d\sin\theta + d\sin\theta = 2d\sin\theta \tag{2.8}$$

If the wavelength of the scattered (incident) X-rays is λ, then the condition for the mutual reinforcement of scattered rays in this direction is

$$2d\sin\theta = n\lambda \tag{2.9}$$

In the Bragg equation, θ is the angle between the incident ray (or reflected ray) and the crystal plane, which is also called the Bragg angle. The angle between the incident ray and the diffracted ray is 2θ, which is called the diffraction angle. The order of reflection is an integer n.

X-ray diffraction analysis is based on the crystal structure. Substances with different crystal structures have specific structural parameters, including lattice type, unit cell size, number of atoms (ions or molecules) in the cell and their positions. These parameters are reflected in the X-ray diffraction patterns, so each crystal provides a unique scattering pattern. Therefore, the materials and their respective crystal structure can be identified from the features such as the number of diffraction peaks, peak position, and intensity.

Additionally, the broadening degree of the diffraction spectra of X-rays is related to the coherence length of lattice plane or the size of the crystal grain. The smaller the grain, the more diffuse and broadened the diffraction rays will become. One Debye-Scherrer formula, which describes the relationship between grain size and the full-width half maximum of a diffraction peak, is

$$D = \frac{K\lambda}{B\cos\theta} \tag{2.10}$$

where K is the Scherrer constant, B is the full width half maximum (FWHM) of the diffraction peak, and typically K is 0.89. θ is the Bragg diffraction angle, λ is the X-ray wavelength, and D is the average thickness of grains perpendicular to the crystal plane.

2.5.2 Grazing incidence small-angle X-ray scattering

GISAXS can be understood as small angle X-ray scattering (SAXS) in grazing incidence geometry. Unlike the transmission geometry applied in SAXS, the X-ray beam impinges onto the sample surface at a very shallow incident angle α_i. Typical values for this incident angle are $\alpha_i < 1°$ (measured with respect to the sample surface). The scattering intensity is probed with a two-dimensional detector as a function of the exit angle α_f and out-of-plane angle Ψ with respect to the sample plane. Figure 2.6 shows a simple schematic of the scattering geometry, [51] the film surface defines the (x, y) plane and the scattering plane is defined by the (x, z) plane. The x-axis is oriented along the X-ray beam direction, the y-axis is parallel to the sample surface and the z-axis is along the surface normal. When the wavelength λ is selected, for monochromatic X-rays with a wavevector $\vec{k_i}$ and a wave number $k_0 = \frac{2\pi}{\lambda}$ being scattered along the $\vec{k_f}$ direction, the scattering vector $\vec{q}$ is given by

$$\vec{q} = \frac{2\pi}{\lambda}\begin{pmatrix} q_x \\ q_y \\ q_z \end{pmatrix} = \frac{2\pi}{\lambda}\begin{pmatrix} \cos(\alpha_f)\cos(\varphi) - \cos(\alpha_i) \\ \cos(\alpha_f)\sin(\varphi) \\ \sin(\alpha_f) + \sin(\alpha_i) \end{pmatrix} \tag{2.11}$$

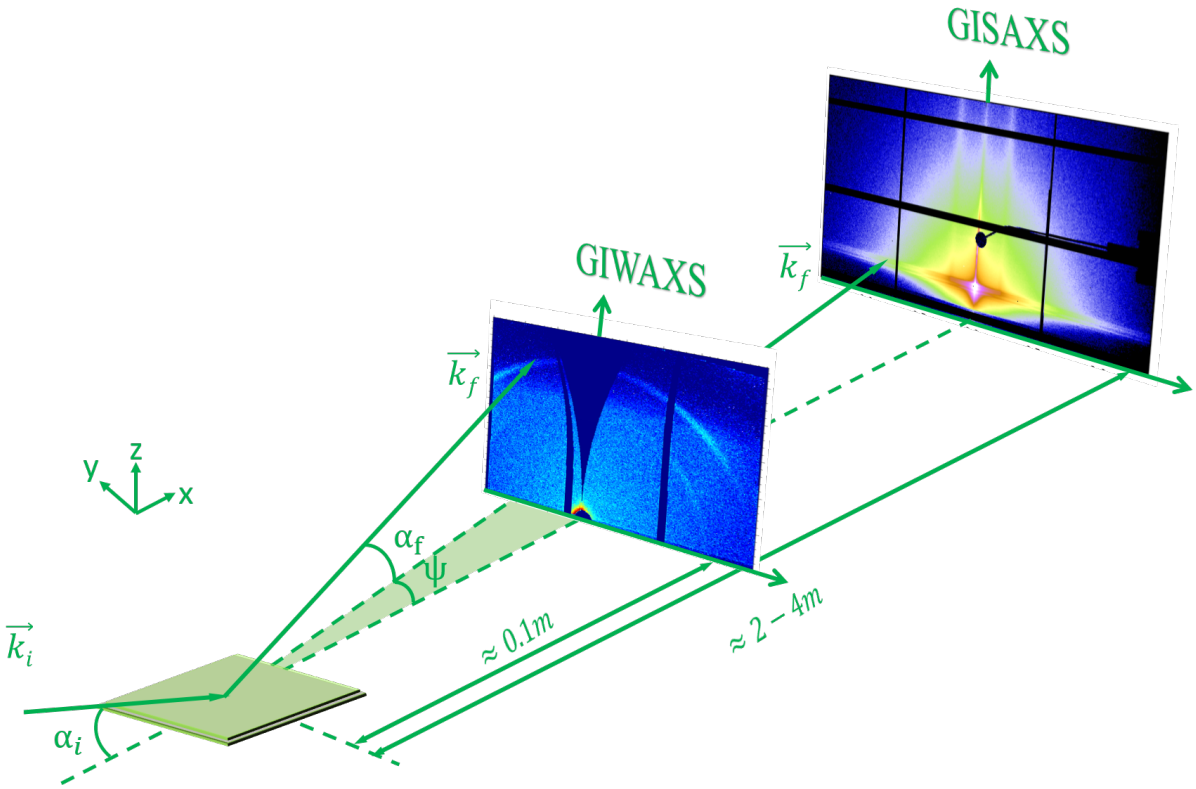

Figure 2.6: Sketch of the scattering geometry used in GISAXS or GIWAXS. The sample surface is placed in the (x, y) plane, inclined by an incident angle α_i with respect to the horizon. The exit angle is denoted α_f and the out-of plane angle ψ. The color coding visualizes differences in the scattered intensity. Typical sample-detector distances for GIWAXS and GISAXS are given as example. [51]

Integration about lateral structures of the perovskite films is given by the components q_x and q_y. Due to $q_x \ll q_y$ in GISAXS mainly the q_y dependence is used for analysis and the q_x is neglected.

For X-rays, the refractive index n is smaller than 1 and represented as

$$n = 1 - \delta(\lambda) + i\beta(\lambda) \tag{2.12}$$

With the dispersion part for X-rays

$$\delta(\lambda) = \frac{e^2\lambda^2}{8\pi^2 m_e c^2 \varepsilon_0}\rho\frac{\sum\limits_k \left[\int_0^k(\lambda) + f'(\lambda)\right]}{\sum\limits_k M_k} \tag{2.13}$$

With the absorption part for X-rays

$$\beta(\lambda) = \frac{e^2\lambda^2}{8\pi^2 m_e c^2 \varepsilon_0}\rho\frac{\sum\limits_k [f''(\lambda)]}{\sum\limits_k M_k} \tag{2.14}$$

where e is the elementary charge, λ is the wavelength, m_e is the electron rest mas, m_e is the speed of light, ε_0 is the permittivity constant, ρ is the mass density, M_k is the atomic weigh, f' and f'' are the dispersion corrections. $\int_0^k$ can be approximated by the number of electrons Z_k. The summation is used for all atoms k of a small molecule of the material under investigation.

When the incident angles is smaller than the critical angle α_c, the total external reflection of the impinging beam occurs.

$$\alpha_c \approx \sqrt{2\delta} = \lambda\sqrt{\frac{SLD}{\pi}} \tag{2.15}$$

The critical angle α_c depends on the material and the incident angle is typically smaller than one degree and in the range of the critical angle of the study material. By adjusting the incident angle α_i, the near-surface structure and the inner structure of the film can be distinguished. When the incident angle $\alpha_i < \alpha_c$, the penetration depth of the X-ray beam is limited to a few nanometers and achieves high surface sensitivity. For $\alpha_i > \alpha_c$, the X-ray beam has a large penetration depth and can probe structures within the entire depth of the film. [51]

The diffuse scattering is analyzed within the framework of the distorted-wave Born approximation (DWBA), using the so-called effective interface approximation (EIA) for the analysis of horizontal line cuts (with respect to the sample surface).

For $\alpha_i \gg \alpha_c$ and with a constant q_z, the diffuse scattering intensity in the DWBA simplifies for an EIA and the differential cross-section $\frac{d\sigma}{d\Omega}$ for diffuse scattering is given by

$$\frac{d\sigma}{d\Omega} = \frac{A\pi^2}{\lambda^4}(1-n^2)^2\left|T_i\right|^2\left|T_f\right|^2 P_{diff}(\vec{q}) \propto P_{diff}(\vec{q}) \tag{2.16}$$

where A refers to the illuminated surface area, λ refers to the wavelength, n refers to the refractive index, T_i and T_f refer to the Fresnel transmission coefficients for the incident and exiting beam, respectively, and $P_{diff}(\vec{q})$ refers to the diffuse scattering factor which contains the morphological information.

Through using a form factor $F(\vec{q})$ of the individual scattering domains and a structure factor $S(\vec{q})$ of the domain assembly, the modeling of the diffuse scattering factor can be simplified as

$$P_{diff}(\vec{q}) \propto N \left|F(\vec{q})\right|^2 S(\vec{q}) \tag{2.17}$$

where N is the number of identical and centro-symmetrical scattering objects with a random orientation under the illuminated area. The selection of the form factors depends on the type of scattering objects. Cylinders and spheres are the most common ones. The structure factor is related to the spatial arrangement of the scattering objects.

In the modeling of the form factor contribution, the shape and the polydispersity, as well as the size distribution need to be considered. The polydispersity is approximated in the so-called decoupling approximation (DA), the local monodisperse approximation (LMA), or the size-spacing correlation approximation (SSCA). [52]

In the DA, all correlations were neglected, and thus the type of the scattering objects and their positions are uncorrelated, which typically applies to small polydispersities. [53] In the LMA, neighboring objects are assumed to have the same shape and size, the scattering weight of each particle is replaced by its mean value over the size distribution. The scattering intensities from monodisperse subsystems are summed up incoherently and weighted by the size–shape probabilities. The LMA requires that the modeled layers consist of monodisperse domains. For large values of the scattering vector, the LMA is asymptotically equal to the DA. Therefore, the differences from DA typically show that the values of the scattering vector are smaller than the position of the particle correlation peak. [54]

In LMA, cross-coupling between different substructures is not included. Therefore, within the LMA, the diffuse scattering factor is proportional to

$$P_{diff}(\vec{q}) \propto \sum_k N_k \left|F_k(\vec{q})\right|^2 S_k(\vec{q}) \tag{2.18}$$

SSCA accounts for the correlation between particles, that is, size-dispersed particles are aligned along a chain. [52, 55] Such an introduction of partial correlation between the adjacent particle sizes and their distance may be important for nanostructured films with densely packed objects. It strongly modifies the shape of the diffuse scattering. In particular, the q_y position of the maximum in the scattered intensity is no longer simply related to the mean particle separation D as expected in the DA or LMA approximation. In contrast, in the SSCA, the correlation peak position decreases upon an increase in the coupling parameter. [53]

2.5.3 Grazing Incidence Wide Angle X-Ray Scattering

GIWAXS can be understood as the extension of GISAXS to the wide-angle region. Briefly, switching from GISAXS to GIWAXS could be completed by changing the sample-detector distance (SDD) from several meters to several centimeters to obtain a larger angular range on the 2D area detector. Therefore, each pixel on the detector collects intensity from a wider range of angles, which turns into more signal, but this also results in more background in each pixel. If not blocked by the beamstop, the original GISAXS is visible in the center of the reciprocal space. Similar to GISAXS, in GIWAXS measurements, different information can be accessed by tuning the ratio between the incident angle α_i and critical angle α_c for an active layer on solid support [51]

When α_i $<\alpha_c$(active layer): Obtaining the information about the crystal structure of the surface-near region of the active layer.

When α_c (active layer) $<\alpha_i<\alpha_c$ (solid support): Obtaining the information about crystal structure in the entire active layer.

When α_c (solid support) $<\alpha_i$: Obtaining the information about crystalline structures in the active layer and of the solid support.

In the analysis of GIWAXS data, the scattering signal is consisting of Debye diffraction cones for each Bragg angle 2θ, which provide information about the crystal structure and crystal orientation with respect to the substrate surface normal of the active layer. The crystal orientation is characterized by the azimuthal angle χ to the normal component q_z of the scattering vector and has four common GIWAXS pattern. [51]

For a highly crystalline film with a crystal orientation parallel to the substrate surface, the 2D detector shows pronounced Bragg peaks, as shown in Figure 2.7a.

For the film with crystal orientation parallel and perpendicular to the substrate surface, the 2D detector shows Bragg peaks along the surface normal (vertical direction) and horizontal direction, respectively, as shown in Figure 2.7b.

For a textured film with domains oriented with an angular distribution around the horizontal alignment, the 2D detector shows the broaden Bragg peaks along the vertical direction, as shown in Figure 2.7c.

For the film with randomly oriented crystallites, the 2D detector shows the Bragg peaks smear out into Debye-Scherrer rings with homogeneous intensity distribution, as shown in Figure 2.7d.

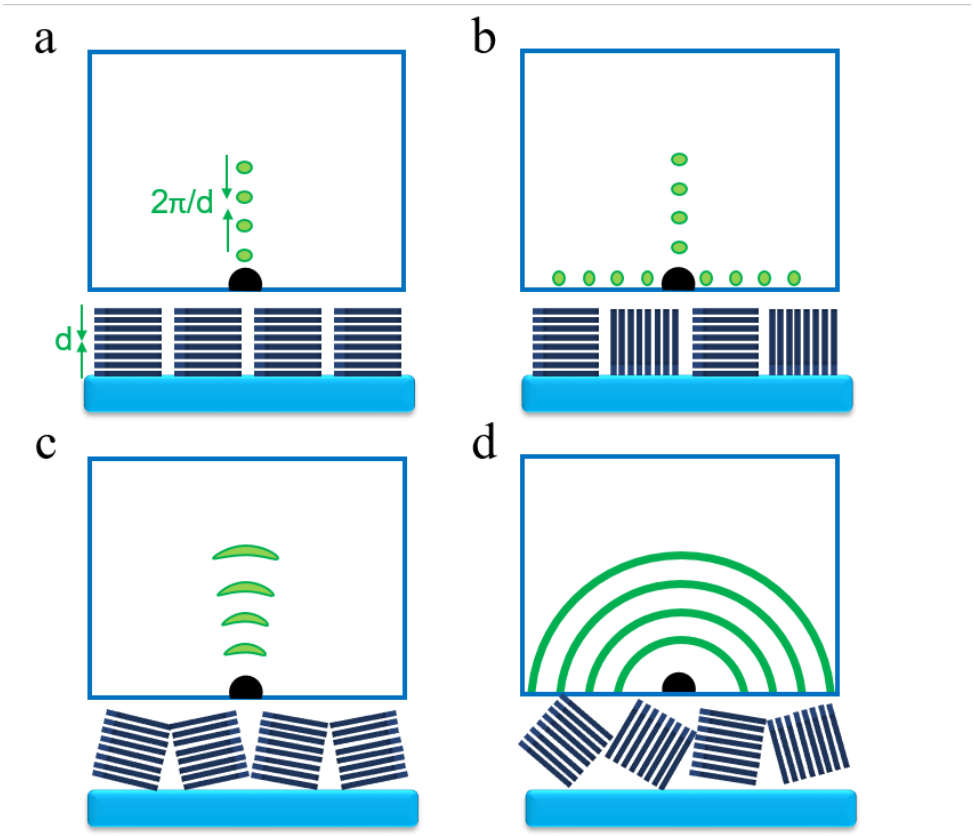

Figure 2.7: Sketch of crystal lattice planes and corresponding 2D GIWAXS data in case of (a) crystallites with vertical orientation, (b) crystallites with vertical and horizontal orientation, (c) oriented domains with an angular distribution around the horizontal alignment and (d) full randomly oriented crystallites. The GISAXS signal is blocked by a beam stop (black box) [51]

For the GIWAXS data representation, the momentum transfer from the reciprocal space to the real-space coordinate system would result in a missing wedge. Consequently, the GIWAXS data is presented in this thesis in the following ways without curvature. (1) Plotting q_z versus q_r, it requires a transformation resulting in a distortion of the detector image and missing wedge around q_r=0 or χ=0. (2) plotting total $q = |\vec{q}|$ versus the azimuthal angle χ.

$$q_r = \sqrt{q_x^2 + q_y^2} \tag{2.19}$$

For the GIWAXS data treatment, because the detector image is merely a distorted version of the reciprocal crystal lattice, corrections for solid-angle, efficiency, polarization need to be applied for complete reconstruction from raw 2D GIWAXS data into the reciprocal-space coordinate system. [56–58]

Solid-angle correction: Account for the measurement geometry, as the nominal pixel area covers different solid angles with respect to the scattering center. [58]

Efficiency correction: Because of the short SDD and the wide scattering angles, several effects need to be considered to correct the probability of scattered photos being detected by the pixel. Photons scattered at different oblique scattering angle 2θ travel through the surrounding medium at a different distance with linear mass attenuation coefficient μ_m. For the measurement conducted in a vacuum, the scattered X-rays travel in the vacuum system, no attenuation need to be considered and μ_m=0. [58]

Polarization correction: The X-rays produced by synchrotron sources have a high percentage (usually around 98%) of horizontal (linear) polarization, which causes dipole oscillations of the electron in the proved material in the polarization direction. Therefore, a part of the photon's energy is lost due to electron excitation and causes a decrease in the scattering intensity in this direction. However, even for non-polarized beams, the dipole emission profile has a slight effect on the scattering intensity.

In the 2D GIWAXS data analysis, the pseudo-XRD refers to integration over all angles theoretically resulting in a scattering pattern like powder XRD after the application of the corrections. [58] For the extraction of crystal orientation information, azimuthal (tube) cuts are carried out along the q position of the Debye-Scherrer ring of interest.

3 Characterization methods

The characterization of the perovskite film and the device performance of the perovskite solar cells represent the main focus of this thesis. Various measurement techniques are used to evaluate the properties of the perovskite films and corresponding devices, which are closely related to the analysis of the experimental results and provide important information about the underlying working mechanism of perovskite solar cells. This section deals with the experiment setups used for the measurement of photoelectric properties of the perovskite films, charge carrier dynamics, as well as device performance of PSCs.

3.1 Perovskite film characterizations

3.1.1 Scanning electron microscopy

Scanning electron microscopy (SEM) is a scanning probe technique that allows for the surface morphology and the cross-section morphology analysis of the perovskite films. All SEM images presented in this thesis are measured with FESEM Gemini NVision 40 instrument (Carl Zeiss GmBH, Jena, Germany) together with the software SmartSEM. The electron source is a filed-emission gun with a tungsten filament. The electron beam is focused on the films by magnetic and electrostatic lenses and scanned across the film surface line by line. Through the interaction of the electron beam with the sample, which is conductive material or with conductive material attached, the sample emits secondary electrons and is collected by an in-lens detector. The number of counts will be translated and represented in a 2D array as intensity, which reflects the surface morphology of the samples. The intensity mainly depends on the material itself, beam size, and the surface morphology, etc. Typically, materials with higher electronic conductivity are brighter. Prominent sharp edges, small particles and relatively steep slopes that have more secondary electron yields, appear brighter in images.

The experiment is operated at a pressure of 2×10^{-6} mbar and an acceleration voltage of 5 keV with working distances at around 3.2 mm. The SEM images are processed with Image J software, and the contrast and brightness are properly adjusted for better visibility of features. Additionally, the scale bars are added in all SEM images to clearly and quickly know the grain sizes of the perovskite crystal.

3.1.2 Surface profilometry

A surface profilometer (DektakXT Stylus Profiler, Bruker) is a simple way to measure the thickness of perovskite thin films. The obtained thickness values are primarily used for calculating the trap density in SCLC and absorption coefficients in UV-vis.

After completing all other necessary measurements, the films are scratched with a sharp tweezer and then placed at the center of the movable stage. A tip with a radius of 250 μm is pressed on the films with a contact force of 1 mg, then the scan started across the scratch with a scan speed of 35 $\mu\text{m} \cdot \text{s}^{-1}$ to obtain the height distribution of the film and then infer the thickness of the film with respect to the substrate. For each sample, the measurement would perform at multiple positions of the samples to avoid experimental error due to potential film inhomogeneity and to improve the confidence of the measurement results.

3.1.3 Atomic force microscopy

Atomic force microscopy (AFM) uses a photodiode to detect the amplitude changes of the interaction force between the tip and the surface atoms of the sample in the direction perpendicular to the surface of the sample, then to obtain the information on the surface morphology and surface roughness of the sample. There are three common measurement modes: contact mode, non-contact mode, and tapping mode. [59]

Contact mode: During the scanning imaging process, the probe tip keeps close contact with the sample surface, and the interaction force is the repulsive force.

Non-contact mode: When probing the sample surface, the cantilever oscillates at a distance of 5–10 nm above the sample surface. The interaction between the tip and the sample is controlled by van der Waals forces. Non-contact mode avoids sample damage and tip contamination.

Tapping mode: The cantilever oscillates at its resonant frequency above the sample surface and the tip only touches or taps the sample surface periodically. [60]

The AFM measurements in this thesis is carried out by using an AFM instrument (MFP-3D, Asylum Research) in tapping mode using conical-shaped tips. The scan rate is 0.4 Hz with an integral gain of 10.

3.1.4 Ultraviolet-visible absorption spectra

Ultraviolet-visible absorption spectra (UV-vis) are measured to evaluate the optical absorption properties of the perovskite film. The measurement is performed using PerkinElmer Lambda 35 instrument which is equipped with two lamps as light source, one is a deuterium lamp that provides light in the UV range of 190-326 nm, and another one is a halogen lamp that provides light covering the visible to the near-infrared region from 326 to 1100 nm. For each measurement, auto-zero (empty beam) is performed for instrument calibration, and a glass or ITO substrate is used as a reference sample. All UV-vis measurements are conducted with a scanning speed of 280 nm/min, with the wavelength range set from 400 to 900 nm. During the measurement, the incoming beam is split by the beam splitter into two beams, one probes the samples and another probes the reference samples. The ratio of the transmitted intensity through the sample and the reference is recorded. Through the measured intensity ratios, the absorbance (A) is calculated based on the Lambert-beer law. [61]

$$A(\lambda) = -\log_{10}\left(\frac{I_t(\lambda)}{I_0(\lambda)}\right) = a(\lambda)L\log_{10} e \tag{3.1}$$

where $I_0(\lambda)$ is the intensity of the reference beam, $I_t(\lambda)$ is the intensity of the incident beam after passing the sample, $a(\lambda)$ is the absorption coefficient of the specific material, and L is the length of light pathing through the sample (usually refer to the layer thickness). The obtained absorbance reflects the light absorption ability of the material at different wavelengths. Additionally, the Tauc plot can be derived from absorbance UV-vis spectra using the Tauc equation. [62, 63]

$$ahv = A(h\nu - E_g)^n \tag{3.2}$$

where A is the constant, α is the absorption coefficient of the material, hν is the photon energy, E_g is the optical band gap, and n depends on the type of transition. Because perovskite is direct band gap semiconductor, n=$\frac{1}{2}$. From the intercept of the linear portion of the $(ah\nu)^2$ vs $h\nu$, the optical band gap of the perovskite film is estimated.

3.1.5 X-ray and ultraviolet photoelectron spectroscopy

X-ray photoelectron spectroscopy (XPS) is a method to measure the energy distribution of photoelectrons and Auger electrons emitted from the sample surface when irradiated by X-ray photons using an electron spectrometer. Through collecting information on the energy and intensity of electrons excited from the material surface under incident X-rays, the material surface is qualitatively and quantitatively analyzed. Ultraviolet photoelectron spectroscopy (UPS) uses ultraviolet light to excite the surface of the sample, thereby causing photoelectrons to be emitted from the sample surface, which used to analyze the work function and valence band of conductor and semiconductor film materials. The corresponding equation is as follows

$$E_k = h\nu - E_b - \phi \tag{3.3}$$

where E_k is the kinetic energy of the photoelectron, hν is the energy of the incident photo, E_b is the binding energy of the electron that is calculated from the Fermi level, ϕ is the work function that needs to be overcome for the photoelectrons to escape the surface.

XPS and UPS are all based on the Einstein Photoelectric effect. In this thesis, XPS and UPS measurements are carried out to investigate the surface electronic properties and valence states of SnO_2 and the perovskite films. For the XPS measurement, XPS is conducted to analyze the near-surface composition using a monochromatized Al Kα source ($h\nu$ = 1486.6 eV) and a pass energy of 20 eV on a SPECS system. The spectra are fitted using Casa XPS analysis software with Shirley background. For calculating the surface atomic composition of the films, the peak area of the Pb $4f_{7/2}$ and I $3d_{5/2}$ peaks is used with the corresponding atomic sensitivity factors

$$\frac{I}{Pb} = \frac{I3d_{5/2}AtomicConcentration}{Pb4f_{7/2}AtomicConcentration} \tag{3.4}$$

For the UPS measurement: laboratory-based UPS measurements are conducted using the He I line at 21.22 eV from a commercial He gas discharge light source (Focus HIS 13). The photoemission spectra are collected using a SPECS Phoibos 150 hemispherical analyzer with a pass energy of 5 eV.

3.1.6 Photoluminescence and time-resolved fluorescence spectroscopy

Photoluminescence (PL) spectroscopy and time-resolved photoluminescence (TRPL) as contactless optical methods are performed to probe the electronic structure and charge carrier dynamics in the materials. [64] In PL measurement, the sample is excited by a certain wavelength of light, then the electrons in the ground state absorb the energy and occupy the higher energy states. Due to the excited state is unstable, the electron returns to its equilibrium state by releasing energy. In the process of returning to the equilibrium states, if the energy is released by emitting photons, this process is called a luminescent transition or a radiative transition. If the excitation energy is dissipated as heat (lattice vibration), this process is called nonradiative transition or quenching. [26, 27]

The steady-state PL spectra is collected through a Horiba Jobin Yvon Fluorolog-3 FL3-22 spectrometer with a 450W Xe lamp. The TRPL measurements are performed using a homemade device with a white light laser (NKT SuperK Extreme EXR-20), which is extended using an EXTEND-UV box. The perovskite film deposited on the ITO substrate is excited with a 350 nm laser. The output signals are recorded using a Princeton Instruments monochromator fiber connected to a low-noise Avalanche Photodiode from Excelitas. The fast and slow lifetimes are obtained by fitting the decay profiles of TRPL with bi-exponential decay functions of times, bi-exponential functions as a suitable function to mathematically describe the decay, not as a physical model. The average lifetimes τ_{ave} were calculated through the following equation

$$\tau_{ave} = (A_1\tau_1^2 + A_2\tau_2^2)/(A_1\tau_1 + A_2\tau_2) \tag{3.5}$$

where A is the amplitude fraction of each lifetime component, τ is the decay lifetime.

3.1.7 Transient absorption spectroscopy

Transient absorption spectroscopy (TAS) is a common ultrafast laser pump-probe technique, which uses an optical pump pulse to excite the sample to an excited state. By adjusting the delay time and using the probe pulse to record the exciting state particles at different delay times, the kinetic process of the transition of material molecules from excited states to other lower energy levels or ground states can be obtained. In this thesis, TAS is implemented to study the charge carrier kinetics in the perovskite films.

All samples are given glass-lid encapsulation. The output of a Ti: sapphire amplifier system (Spectra-Physics Solstice Ace) operating at 1 kHz and generating ∼100 fs pulses is used to generate the pump pulses. The 400-nm pump pulses are created by sending the 800-nm fundamental beam through a second harmonic generating (SHG) beta barium borate (BBO) crystal (Eksma Optics). The broadband white probe is provided by the Disco (Leukos Laser, STM-2-UV) and the pump-probe decay is controlled electronically. The white light is split into two identical beams (probe and reference) by a 50/50 beamsplitter. The reference beam passing through the sample does not interact with the pump, which allows for correcting for any shot-to-shot fluctuations in the probe that would otherwise greatly increase the structured noise in the experiments. Based on this arrangement, small signals with $\frac{\Delta T}{T}$ $\sim 10^{-5}$ could be measured. The transmitted probe and reference pulses are collected with a silicon dual-line array detector (Hamamatsu S8381-1024Q, spectrograph: Andor Shamrock SR-303i-B) driven and read out by a custom-built board (Stresing Entwicklungsbüro). Normalized TA kinetics are fit using bi-exponential decay.

$$y = A_1 \exp(-\frac{t}{\tau_1}) + A_2 \exp(-\frac{t}{\tau_2}) + y_0 \tag{3.6}$$

Average lifetimes τ_{ave}, were calculated by

$$\tau_{ave} = (A_1\tau_1^2 + A_2\tau_2^2)/(A_1\tau_1 + A_2\tau_2) \tag{3.7}$$

3.1.8 Fourier-transform infrared spectroscopy

Fourier-transform infrared spectroscopy (FTIR) is used to identify the organic functional groups in materials. When a beam of infrared light with a continuous wavelength passes through the substance, the vibration or rotational frequency of one group in the molecule is the same as the frequency of the infrared light, the molecule absorbs energy and transitions from the original ground state vibrational (rotational) energy level to higher vibrational (rotational) energy level. Infrared spectroscopy is an analytical method for determining the molecular structure of substances and identifying compounds based on information about the relative vibration between atoms within the molecule and molecular rotation.

The conditions for the generation of the infrared absorption spectrum are: (1) The energy of the electromagnetic wave irradiated to the molecule is equal to the difference between the two energy levels of the molecule. Then the electromagnetic wave of this frequency could be absorbed by the molecule and cause the transition of the corresponding energy level. The transition of two adjacent vibrational energy levels should satisfy

$$\Delta E = E_{(\nu+1)} - E_{(\nu)} = h\nu \tag{3.8}$$

where $h\nu$ is the photon energy.

(2) There is a coupling between infrared light and molecules, only the vibration with the dipole moment changes causes infrared absorption.

In this thesis, FTIR measurements is used to verify the coordination between sulfonic groups and lead ions on the perovskite surface. The FTIR measurements are carried out at an Equinox 55 spectrometer (Bruker) with the software Opus v 6.0. Overall, 256 scans (resolution = 2 cm^{-1}) over a wavenumber range of 500-4000 cm^{-1} are averaged to get a final FTIR spectra for each measurement.

3.2 Device characterization

3.2.1 J-V measurement

J-V measurements are the critical and direct technique to evaluate the photovoltaic performance of solar cells. In this thesis, the *J–V* data is collected using a Keithley 2611B source meter, under simulated AM 1.5 G sunlight at 100 mW cm^{-2} irradiance generated by a solar simulator (class ABA) equipped with Xenon lamp. Before measurement, the intensity of the solar simulator is calibrated with a KG5-filtered Si reference cell (Fraunhofer ISE019-2015), and the recorded intensity is used to calculate the precise power conversion efficiency. Every device contains six gold top electrodes with a dimension of 2.5×10.0 mm^2 on a substrate with a size of 25×25 mm^2. The active area is defined by a metal aperture mask (0.10 or 0.1875 cm^2) to avoid the high photocurrent caused by edge effects. The *J-V* curves are measured with a scanning speed of 50 mV s^{-1} (integration time of 100 ms) from forward to reverse scan (from 1.25 V to -0.20 V and then back from -0.20 V to 1.25 V). The cells are measured several times to reach the highest PCE for each device.

3.2.2 Electrochemical impedance spectroscopy

Electrochemical Impedance Spectroscopy (EIS) is to apply a small-amplitude AC excitation signal to the electrochemical cell according to the sinusoidal law when the electrochemical cell is in an equilibrium state (open-circuit state) or under a certain stable DC polarization condition. Then record the changing relationship of electrochemical AC impedance with frequency.

The EIS data are commonly analyzed by fitting to an equivalent circuit model. The circuit model consists of electrical elements such as resistors R, inductors, and capacitors C through serial or parallel combination, the elements in the circuit model have their physical electrochemical meaning. Thus, the result of EIS data could be used to analyze the impedance value of each element in the equivalent circuit model and its meaning.

Two commonly used electrochemical impedance spectroscopies: Nyquist plot and Bode plot. The Nyquist plot takes the real component of the impedance as the horizontal axis and the negative number of the imaginary component as the vertical axis. Each point in the spectroscopy corresponds to a different frequency, the left part is the high-frequency area, and the right part is the low-frequency area. The Bode plot is a method to represent the characteristics of electrochemical impedance spectroscopy. Including two curves, the horizontal axis is the logarithm of the frequency, and the vertical axis is the logarithm of the impedance modulus value. The other is the phase angle of the impedance.

In this thesis, EIS measurements on the whole cells are performed to provide insights into the electrical properties such as interface charge transport and contact resistance. The impedance spectroscopy in this thesis the main use is the Nyquist plot, the equivalent circuit model adopted is shown in Figure 3.1.

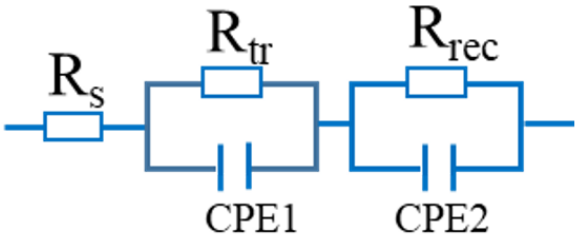

Figure 3.1: Electrical equivalent circuits used for impedance spectra.

The Nyquist plots are analyzed with an equivalent circuit model mainly composed of series resistance (R_s) and two components for transfer resistance (R_{tr}) and recombination resistance (R_{rec}) forming a parallel circuit with capacitors (C_{tr} and C_{rec}). The R_s primarily reflects the electrical contacts, wires and sheet resistance of the electrodes, the R_{tr} ascribed to the high-frequency element reflects the charge extraction/transfer properties at the ETL-perovskite or perovskite-HTL interface, and the R_{rec} assigned to the low-frequency one in EIS is related to the charge carrier recombination arising from defect densities.

For the EIS measurement, it is performed on the PSCs in dark conditions using a scanning frequency between 1 and 10 Hz, and an AC amplitude of 5 mV (EC-Lab V11.36).

3.2.3 Open circuit voltage decay measurement

Open circuit voltage decay (OCVD) is a useful method to detect the voltage variation in a device with contact. The photovoltage V in solar cells depends on the difference in the Fermi level of electrons and holes at their corresponding electron and hole selective contact. [65, 66] The separation is caused by the modification of a minority carrier Fermi level by a photogenerated carrier, as

$$n = n_0 \exp(\frac{qV}{k_B T}) \tag{3.9}$$

OCVD is introduced to measure the decay of open-circuit voltage to the state of dark equilibrium value (V=0). [67] The recombination times describe as follows

$$\tau_{rec} = -\frac{k_B T}{q}(\frac{dV}{dt})^{-1} \tag{3.10}$$

where τ_{rec} is the recombination lifetime of the minority carrier, q is the elementary charge, $k_B T$ is the thermal energy. Because the time constant measured by the reciprocal voltage derivative is not related to recombination. [68] In the analysis of photovoltage decays, an instantaneous relaxation time is defined to describe a general relaxation phenomenon as follows [69]

$$\frac{dV}{dt} = -\frac{1}{\tau_{ir}}V \tag{3.11}$$

When the voltage decay obeys an ideal relaxation exponential law, the characteristic time τ_{ir} is a constant. If not, then is a function of the voltage which describes as

$$\tau_{ir}(V) = (-\frac{1}{V}\frac{dV}{dt})^{-1} \tag{3.12}$$

τ_{ir} (V) is the instantaneous advance of the relaxation which different from the recombination lifetime τ_{rec}. [67] The representation of τ_{ir} (V) provides the discriminative ability to separate different types of relaxation dynamics. [69]

For the OCVD measurement in this thesis, a laser diode (central wavelength: 520 ± 5 nm, RGB Laser systems, NovaPro) is used as the excitation source, and the beam power is tuned through a neutral density filter (Daheng Optics, GCO-074M). The device is paralleled with a homemade CMOS switch (response time: $\sim$ 4 ns, intrinsic resistance: 50 Ω) and a digital oscilloscope (Lecroy, HDO4054A). The temporal sequence is synchronized and controlled by a digital delay and pulse generator (Stanford Research Systems, DG535), and the temporal evolution of the photoelectric signals is recorded by the oscilloscope (coupling resistance 1MΩ). The OCVD measurements are conducted by illuminating the cells for ∼5 s until the V_{ph} reached a constant. Then the laser is turned off to induce the decay of V_{ph} at an open circuit. The large signal voltage decay of the device after light excitation is monitored by oscilloscope.

3.2.4 Transient photovoltage and transient photocurrent measurements

As a complement to the OCVD results, the small perturbation TPV is used to detect faster decay components with relaxation times in ms scale. While TPC is performed to investigate the photo-generated electron extraction and transportation in the μs time scale.

For the TPV and TPC measurements in this thesis, the device is irradiated under a continuous-wave LED laser (520±5 nm, RGB photonics, Lambda beam) to keep a steady-state photovoltage (V_{ph}). The reduction (ΔV_{ph}) in V_{ph} ($V_{ph}/V_{ph} \leq 5$ %) is achieved with a second laser (pulses at 532 nm, 7 ns). For TPV, the electric signal is recorded by a digital oscilloscope (Lecroy, HDO4054A) with 1 MΩ input impendence. The lifetime is obtained by fitting the decay profiles with bi-exponential decay function. For TPC, the input impendence is set to 50 Ω under the same illumination with TPV, the lifetime is obtained by fitting the decay profiles with mono-exponential decay function.

3.2.5 Space-charge-limited current measurements

Space-charge-limited current (SCLC) measurement is a steady-state technique to study the charge transport properties of semiconducting material, such as charge carrier trap density n_{trap}, charge carrier mobility μ, charge carrier diffusion length L_D, and so on. In the SCLC measurement, the dark current is performed under dark conditions as a function of bias voltage. In this thesis, two device structures are prepared to collect the SCLC measurement, electron-only devices based on glass/ITO/SnO_2/perovskite/PCBM/Au architecture and hole-only devices based on glass/ITO/PTAA/perovskite/Spiro-OMeTAD/Au

architecture. In general, the typical dark J-V traces shows three regions of behaviors, as shown in Figure 3.2.

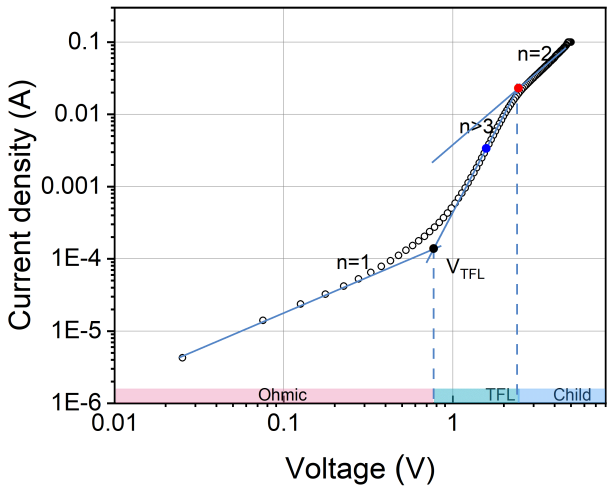

Figure 3.2: Space-charge-limited current measurement.

The first region at low bias corresponded to the Ohmic region, where the current growth linearly with increasing voltage, as confirmed by the fit to $I \propto V$ function dependence. From this region, the conductivities (σ) of the perovskite crystals could be estimated. In the second region, the current exhibits an abrupt nonlinear rise starting at V_{TFL}, known as the trap-filling limit where all the available trap states are filled by the injected charge carriers. [70] The density of trap states n_t is linearly proportional to the onset voltage V_{TFL}. From this region the n_t is calculated by the following equation [71]

$$n_t = \frac{2V_{TFL}\varepsilon\varepsilon_0}{eL^2} \tag{3.13}$$

where V_{TFL} is the trap-filled limit voltage, ε is the relative dielectric constants, ε_0 is the vacuum permittivity, e is the electron charge, and L is the thickness of the perovskite crystal.

When the bias voltage further increase, the current show a linear relationship with the square of the voltage ($I \propto V^2$), defined as Child's regime. From this region the charge carrier mobility (electron mobility μ_n or hole mobility μ_p) is calculated according to the Mott-Gurney law [72]

$$\mu = \frac{8J_D L^3}{9\varepsilon\varepsilon_0 V^2} \tag{3.14}$$

where J_D is the current density.

By combining it with the charge carrier lifetime, the charge carrier diffusion length is calculated by the following relation

$$L_D = \left(\frac{\mu\tau k_B T}{e}\right)^{\frac{1}{2}} \tag{3.15}$$

where k_B is Boltzmann's constant and T is the temperature.

By using the longer charge carrier lifetime (bulk component), a best-case carrier diffusion length is calculated. In contrast, the worst-case diffusion lengths are derived from the fast transient lifetimes (surface component). [70, 73]

3.3 X-ray diffraction

3.3.1 X-ray diffraction

XRD is applied to identify the crystallinity and crystal structure of perovskite thin films. In this thesis, the XRD measurements are carried out on a Bruker D8 Advance X-ray diffractometer. This instrument uses a copper (Cu) anode as the source to generate X-ray with a wavelength of 1.54 Å (Cu K_α) under operation at the voltage of 40 kV and the current of 40 mA.

The X-ray beam impinges on the sample at an angle θ, and the specularly reflected X-ray beam is detected by a point detector at the same angle θ. To get higher quality XRD spectra, two 0.6 mm slits are used to collimate the X-ray before impingement on the sample and before the detector.

During the entire measurement, the couple $\theta/2\theta$ mode is applied that the angle between the incident and the reflected beam is kept at 2θ. For perovskite thin films, the 2θ scan range is set from 5° to 35° with a step size of 0.04°. The instrument is controlled by the software Diffrac.commander, the XRD data of the samples is analyzed with the software Jade using the Power Diffraction File (PDF) and identified by comparing with the standard peaks from the International Centre for Diffraction Data (ICDD).

3.3.2 Grazing incidence wide-angle X-ray scattering

Information of films about crystal structure and crystal orientation is gained from static GIWAXS measurements using a LAMBDA 4.5M detector (X-Spectrum) with a pixel size of (55 × 55) μm^2. The sample-to-detector distance is 235.48 mm and the incident angle α_i is set from 0.2°, 0.4°, and 0.6° to obtain information at different depths and the whole sample to avoid information missing. The X-ray wavelength and the beam size are 11.83 keV and (28 × 24) μm^2 (horizontal × vertical), respectively. The exposure time for all

measurements is set to 1 s. To avoid radiation induced degradation during the GIWAXS measurements, lateral scanning along the sample surface is performed to distribute the X-ray dose between the individual measurement positions.

For the 2D GIWAXS data treatment, the treatment is conducted using the Matlab-based software GIXSGUI which is developed by Zhang Jiang from the Advanced Photon Source at the Argonne National Laboratory (Illinois, USA). [56] The correction is also completed with the Matlab-based software GIXSGUI. Afterwards, the radial integral is performed from 0° to 90° or -90° to 90° to obtain pseudo-XRD. The azimuthal (tube) cut is performed from 0° to 90° along the interested q position to obtain the crystal orientation.

3.3.3 Operando grazing-incidence small/wide-angle X-ray scattering

The operando experiments are conducted at beamline P03 at Deutsches Elektronen-Synchrotron (DESY, Hamburg), as shown in Figure 3.3. The energy of the monochromatic X-ray beam is set to 11.83 keV to avoid absorption edges of the perovskite (around 13 keV) and thus minimize X-ray radiation damage. [74] Two-dimensional (2D) GIWAXS data are collected with a Pilatus 300 k (Dectris, pixel size 172 μm) and LAMBDA 4.5 M (X-Spectrum, pixel size 55 μm) detectors, the incident angle is set to 0.6°. 2D GISAXS data is collected at an incident angle of 0.35° with Pilatus 2 M and Pilatus 300 k detectors. The beam center and the sample-to-detector distance (SDD = 235.48 mm) of the 2D GIWAXS data are calibrated via fits of CeO_2 powder data using the DPDAK package. [75] The beam center and the sample-to-detector distance (SDD=3562 nm) of the 2D GISAXS data are calibrated via silver behenate. The GISAXS detector images are further treated via the DPDAK package based on Python v.2.7. The reciprocal q-space GIWAXS scattering images, the line cuts, and the azimuthal integrations of the scattering data are obtained with the GIXSGUI MATLAB plug-in. [75] To calibrate the intensity of different scattering images, I normalize each frame to the intensity to the ionization energy of the incident X-ray beam.

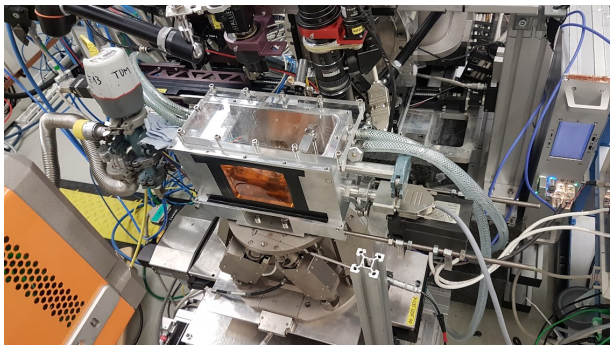

Figure 3.3: Sketch of operando GIWAXS/GISAXS experiment.

3.3.4 Modeling of GISAXS data

The horizontal line cuts of 2D GISAXS data that include the information on the lateral structure of the perovskite thin films, extracted at the Yoneda peak position, are modeled in the framework of the distorted wave Born approximation (DWBA) using the local monodisperse approximation (LMA). [51, 76, 77]

The scattering signal consisted of rotation-symmetric averages over the scattering centers in the plane of the substrate, with the substrate and film surface acting as vertical confinement, the scattering objects are modeled with a cylindrical structure with a Gaussian size distribution, referred to as the form factor. The center-to-center distance between adjacent objects is referred to structure factor. For a successful modeling of the scattering data, three kinds of cylinders with different size distribution are accounted. [77] In the 2D scattering image, vertical and horizontal line cuts are performed. In the vertical line cuts, the Yoneda peak could be observed between the sample horizon and the specular beam. In the horizontal cuts, the LMA model of the DWBA is applied to model the horizontal cuts in which the radius and the corresponding center-to-center distance can be extracted.

3.3.5 Calculation of lateral size distributions

Within the LMA, the scattering intensity is expressed as:

$$P_{diff}(\vec{q}) \propto N \left|F(q, R_i)(\vec{q})\right|^2 S(\vec{q}) \tag{3.16}$$

Considering the cylinders with different radii R_i and equal height, and $F(\vec{q}, R_i, \rho)$due to an uncorrelated distribution of the scattering centers, the form factor of the cylinders is $F(\vec{q}, R_i)$, [77] and weighted with $w_i(R)$, the calculation of the mean square of the form factor is

$$\left|F(q, R_i)\right|^2 = \frac{\int w_i(R) \left|F(q, R)\right|^2 dR}{\int w_i(R) dR} \tag{3.17}$$

To account for deviations from the (three) mean radii, $w_i(R)$ represented a Gaussian size distribution

$$w_i(R) = \frac{1}{\sigma_i \sqrt{2\pi}} \exp(-\frac{(R - R_i)^2}{2\sigma_i^2}) \tag{3.18}$$

The superposition of form factor functions calculate with their intensities represented the lateral size distribution inside the perovskite film, while the intensity scale is linearly related to the number of N_i of scattering centers with a radius R_i as

$$I(\vec{q}) \propto (\sum_i N_i w_i(R)) \left|F(q, R)\right|^2 dR \tag{3.19}$$

4 Sample preparation

In this chapter, materials, preparation processes of perovskite films and fabrication of perovskite solar cells are introduced. Section 4.1 describes the main materials used in this thesis. Section 4.2 describes the substrate preparation. Section 4.3 describes the preparation processes of the perovskite precursor solutions. Section 4.4 describes the fabrication process of the perovskite solar cells.

4.1 Materials

4.1.1 Substrate materials

P-doped silicon wafers are purchased from SiMat Silicon Materials e.K, Kaufering, Germany. The silicon wafers are polished on the side of (100) crystal planes. According to experimental requirements, the silicon wafers are cut into the size of 1.5×1.5 cm with a diamond cutter from the backside. The silicon wafers are subjected to cleaning in an acid bath for 20-30 min, then washed with deionized water several times and dried with nitrogen. Before use, the silicon wafers are functionalized with O_2 plasma for 10 min.

The standard microscope slides are made of soda-lime glass with dimensions 75×25 mm^2 and a thickness of 1 mm purchased from Carl Roth GmbH δ Co. KG, Darmstadt, Germany. According to the experimental requirement, the slides are cut into the size of 2.5×2.5 cm with a diamond cutter. Subsequently, the slides are cleaned sequentially with diluted Hellmanex solution ($V_{Hellmanex}$:V_{H2O}, 2: 98) (purchased from Sigma-Aldrich, catalog no. Z805939-1EA), deionized water, acetone (Carl Roth), and isopropanol (Carl Roth) in an ultra-sonication bath for 25-30 min, then dried with dry nitrogen. Before use, the substrates are treated with UV-oxygen for 10 min.

Indium-doped tin oxide (ITO)-coated glass substrates are purchased from Lumtec, catalog no. LT-G001, the substrate size: 25×25 mm^2, the ITO substrates are cleaned sequentially with diluted Hellmanex solution ($V_{Hellmanex}$: V_{H2O}, 2: 98), deionized water, acetone, and isopropanol in an ultra-sonication bath for 25-30 min, then dried with dry nitrogen. Before use, the substrates are treated with UV-oxygen for 10 min.

4.1.2 Materials for preparing perovskite solar cells

Tin (IV) oxide 15 % in H_2O colloidal dispersion (SnO_2 precursor solution) is purchased from Alfa Aesar, catalog no. 44592. Deionized water is purchased from Sigma Aldrich (catalog no. 8483331000), CAS number is 7732-18-5, and the molecular weight is 18.02 g/mol. [6,6]-Phenyl C_{61} butyric acid methyl ester (PCBM, 910.88 g/mol), catalog no. 684449, CAS number. 160848-22-6, is purchased from Sigma Aldrich.

Lead(II) Iodide (PbI_2, 461.01 g/mol), catalog no. L0279, CAS number. 10101-63-0. Formamidinium iodide (FAI, 171.97 g/mol), catalog no. F1263, CAS number. 879643-71-7. Lead bromide ($PbBr_2$, 367.01 g/mol), catalog no. L0288, CAS number. 10031-22-8. These materials are purchased from TCI Chemicals.

Methylammonium bromide (MABr, 111.97 g/mol), catalog no. 793507, CAS number. 6876-37-5. Cesium iodide (CsI, 259.81 g/mol), catalog no. 914819, CAS number. 7789-17-5. Cesium bromide (CsBr, 212.81 g/mol), catalog no. 915181, CAS number. 7787-69-1. Phenethylammonium iodide (PEAI, 249.09 g/mol), catalog no. 805904. Sodium dodecylbenzenesulfonate (SDBS, 348.48 g/mol), catalog no. 289957, CAS number. 25155-30-0. 1-butyl-1-methylpyrrolidinium tetrafluoroborate ($Pyr_{14}BF_4$, 229.07 g/mol), catalog no. 900809, CAS number. 345984-11-4. 1-butyl-3-methylimidazolium tetrafluoroborate ($BMIMBF_4$, 226.02 g/mol), catalog no. 711748, CAS number. 174501-65-6. 1-ethyl-3-methylimidazolium trifluoromethanesulfonate (EMIMOTf, 260.23 g/mol), catalog no. 00738, CAS number. 145022-44-2. These materials are purchased from Sigma Aldrich.

2,2',7,7'-tetrakis[*N*,*N*-di(4-methoxyphenyl)amino]-9,9'-spirobifluorene (Solarpur© SHT-263, 1225.43 g/mol), catalog no. 902500, CAS number. 207739-72-8. Poly[bis(4-phenyl)(2,4,6-trimethylphenyl)amine] (PTAA), catalog no.702471, CAS number. 1333317-99-9. Lithium bis(trifluoromethanesulfonyl)imide (LiTFSI, 287.09 g/mol), catalog no. 919977, CAS number. 90076-65-6. Tris(2-(1H-pyrazol-1-yl)-4-tert-butylpyridine)cobalt(III) tri[bis(trifluoromethane)sulfonimide] (FK 209 Co(III) TFSI, 1503.17 g/mol), catalog no. 805394. 4-tert-butylpyridine (TBP, 135.21 g/mol), catalog no. 142379, CAS number. 3978-81-2. These materials are purchased from Sigma Aldrich.

N, *N*-dimethylformamide (DMF, 73.09 g/mol), catalog no. 227056, CAS number. 68-12-2. Dimethyl sulfoxide (DMSO, 78.13 g/mol), catalog no. 276855, CAS number. 67-68-5. Chlorobenzene (CB, 112.56 g/mol), catalog no. 284513, CAS number. 108-90-7. Methanol (32.04 g/mol), catalog no. 322415, CAS number. 67-56-1. 2-Propanol (IPA, 60.10 g/mol), catalog no. 278475, CAS number. 67-63-0. These materials are purchased from Sigma Aldrich.

4.2 Substrate preparation

4.2.1 Preparation of the HBL

For SnO_2 as HBL, the tin oxide (SnO_2) precursor was prepared by dissolving tin (IV) oxide 15 % in H_2O colloidal dispersion in deionized water (V_{SnO2}: V_{H2O}, 1:4). The precursor solution was stirred for 2 h at room temperature. Afterward, the tin oxide solution (SnO_2) was filtered and spin-coated on cleaned ITO substrates at 4000 r. p. m for 30 s, followed by annealing at 150∼170 °C for 30 min.

For the ionic liquids-treated SnO_2 substrate, discussed in Chapter 7. Ionic liquids solution with different concentrations dissolved in methanol were spin-coated on the SnO_2 substrates at 6000 r. p. m for 20 s, followed by annealing at 100 °C for 10 min in the glovebox. After cooling down, the substrates were plasma-treated again for 10 min to increase surface wettability, and then transferred into a N_2-filled glovebox.

For the PCBM as HBL for the electron-only device, the PCBM solution was prepared by dissolving PCBM (20 mg) in 1 mL chlorobenzene, and stirring for 30 min. Then the PCBM solution was dynamically spin-coated on the top of the perovskite at a speed of 2000 r. p. m. for 30 s.

4.2.2 Preparation of the EBL

For Spiro-OMeTAD as EBL, the Spiro-OMeTAD solution was prepared by dissolving Spiro-OMeTAD (72.3 mg), 17.5 μL lithium bis(trifluoromethylsulphonyl)imide solution (LiTFSI) (520 mg/mL in acetonitrile), 28.8 μL tris(2-(1H-pyrazol-1-yl)-4-tert-butylpyridine)cobalt(III) tri[bis(trifluoromethane)sulfonimide] (FK 209 Co(III) TFSI) solution (180 mg/mL in acetonitrile), and 28.8 μL 4-tert-butylpyridine (TBP) in 1 mL chlorobenzene, stirring for 40 min. Then the spiro-OMeTAD solution was dynamically spin-coated on the top of the perovskite at a speed of 3500 r. p. m. for 20 s.

For PTAA as EBL for the hole-only device, the PTAA solution is prepared by dissolving PTAA (2 mg) in 1 mL toluene, stirring for 30 min. Then the PTAA solution was dynamically spin-coated on the ITO substrate at a speed of 4000 r. p. m. for 25 s, then annealed for 10 min at 100 °C.

4.3 Preparation of perovskite precursor solutions

4.3.1 Preparation of perovskite precursor solution discussed in Section 5

The MAPI perovskite precursor solution was prepared by dissolving lead iodide (PbI_2, 1.0 M) and methylammonium iodide (MAI, 1.0 M) in a mixture of anhydrous *N*, *N*-dimethylformamide (DMF) and dimethyl sulfoxide (DMSO) (*V*: *V*, 7: 3), and stirred for 2 h at room temperature. Then the precursor was spin-coated on the SnO_2/FTO substrates at 3500 r. p. m. for 30 s in a N_2-filled glove box (acceleration rate 750 r. p. m $\cdot$ s^{-1}). After the spinning started for 8 seconds, 200 μL CB was rapidly dropped on the rotating substrate. After finishing the spin-coating, the samples were placed at room temperature for 2 min and then placed on preheated hotplate to anneal at 100 °C for 30 min.

For the SDBS treated perovskite film preparation, sodium dodecylbenzene sulfonate (SDBS) powder was dissolved in isopropanol at a concentration of 1 and 2 mg/mL and then stirred for 1 h. Subsequently, the SDBS solution was spin-coated on the MAPI substrates at 4000 r. p. m. for 20 s, followed by annealing at 150 °C for 10 min.

4.3.2 Preparation of perovskite precursor solution discussed in Section 6

The MAPI perovskite precursor solution was prepared by dissolving lead iodide (PbI_2, 1.0 M) and methylammonium iodide (MAI, 1.0 M) in a mixture of DMF and DMSO (*V*: *V*, 7: 3). For the $(CsPbBr_3)_x(MAPbI_3)_{1-x}$ perovskite solution was prepared by dissolving cesium bromide (CsBr, x % M), MAI (1-x % M) and PbI_2 (1.0 M) in the same mixture solvent. After stirring for 2 h, the perovskite precursor solutions were spin-coated on the SnO_2/FTO substrates at 3500 r. p. m. for 30 s in a N_2-filled glove box. During the spin-coating, 150 μL CB was rapidly dropped on the rotating substrate after 8 seconds of the beginning of spin-coating. After finished, the samples were placed on preheated hotplate to anneal at 100 °C for 30 min.

4.3.3 Preparation of perovskite precursor solution discussed in Section 7

The $(MAPbBr_3)_{0.15}$ $(FAPbI_3)_{0.85}$ perovskite precursor solution was prepared by dissolving formamidinium iodide (FAI, 189 mg), lead bromide (PbI_2, 530.2 mg), methylammonium

bromide (MABr, 22.4 mg), and lead bromide ($PbBr_2$, 73.53 mg) in 1 mL mixed solvent of DMF and DMSO (V_{DMSO}: V_{DMF}, 1: 4). In parallel, the ionic liquids-containing perovskite precursor solution was prepared by dissolving the same components in a mixed solvent containing different ionic liquids (0.1 mmol). The obtained perovskite precursor solutions were stirred for 2 h in the glovebox and filtered (0.45 μm, PTFE) before spin-coating.

4.4 Device fabrication

The fabrication process of devices in this thesis was shown in the Figure 4.1.

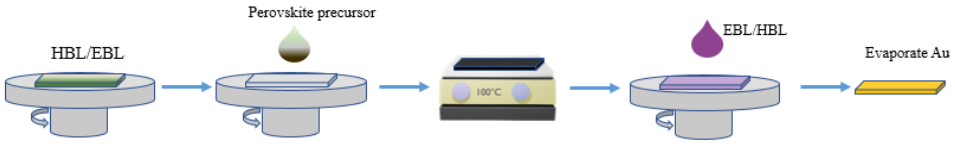

Figure 4.1: Schematic diagram of the device preparation process

4.4.1 Fabrication of n-i-p device discussed in Section 5

Before further processing, the substrates were treated with an oxygen plasma for 10 min. The diluted SnO_2 colloidal solution (1: 4 with deionized water) was spin-coated on the cleaned FTO substrates at 4000 rpm for 30 s and placed on a hotplate for annealing for 30 min at 150 °C in ambient conditions. After being cooled down to room temperature, the substrates were treated with an oxygen plasma for 10 min and then transfer to a N_2-filled glovebox for further perovskite film deposition. The MAPI perovskite precursor solution was prepared by dissolving PbI_2 (1.0 M) and MAI (1.0 M) in a mixture of DMF and DMSO (V: V, 7: 3) and stirred for 2 h at room temperature. Afterward, the perovskite precursor solution was spin-coated on the SnO_2/FTO substrates at 3500 r. p. m. for 30 s. After the spinning started for 8 s, 200 μL CB was rapidly dropped on the rotating substrate. After finishing the spin-coating, the samples were annealed at 100 °C for 30 min.

For the SDBS-treated perovskite film, the SDBS solution was spin-coated on the MAPI substrates at 4000 r. p. m. for 20 s, followed by annealing at 150 °C for 10 min. After the substrates were cooled down to room temperature, 50 µL Spiro-OMeTAD solution was spin-coated on the perovskite layers at 4000 r. p. m. for 30 s. Finally, an 80 nm thick gold electrode was thermally evaporated on the substrate under vacuum conditions with the pressure of 2×10^{-5} torr.

4.4.2 Fabrication of n-i-p device discussed in Section 6

The ITO substrates are treated with oxygen plasma for 10 min. Then the diluted SnO_2 colloidal solution (1: 4 with deionized water) was spin-coated on the cleaned ITO substrates at 4000 rpm for 30 s and annealed at 170 °C for 30 min in the air. After being cooled down to room temperature, the substrates were treated with an oxygen plasma for 10 min and then transfer to a N_2-filled glovebox for further perovskite film deposition. Afterward, the pristine MAPI and $(CsPbBr_3)_x(MAPbI_3)_{1-x}$ perovskite precursor solution were spin-coated on the SnO_2/FTO substrates at 3500 r. p. m. for 30 s. During the spin-coating, 150 µL CB was rapidly dropped on the rotating substrate after 8 seconds of the beginning of spin-coating. After finished, the samples were placed on a hotplate to anneal for 30 min at 100 °C. After the substrates were cooled down to room temperature, 35 μL Spiro-OMeTAD solution was spin-coated on the top of as-prepared perovskite layers at 5000 r. p. m. for 30 s. Finally, a 70 nm thick gold electrode was thermally evaporated on the as-prepared samples under vacuum conditions with the pressure of 1×10^{-4} torr.

4.4.3 Fabrication of n-i-p device discussed in Section 7

The SnO_2 solution was filtered and spin-coated on cleaned ITO substrates at 4000 r. p. m for 30 s, followed by annealing at 170 °C for 30 min. For the ionic liquids-treated SnO_2 substrates (IM-perovskite), ionic liquids solutions with different concentrations dissolved in methanol were spin-coated on the SnO_2 substrates at 6000 r. p. m for 20 s, followed by annealing at 100 °C for 10 min in the glovebox. After cooling down, the substrates were plasma-treated again for 10 min to increase surface wettability, and then transferred into a N_2-filled glovebox. The perovskite precursor solution was spin-coated on ITO/SnO_2 substrates at 1000 r. p. m for 5 s and 5000 r. p. m for 20 s, during the second spin-coating process, 170 μL chlorobenzene was quickly dropped into the center of the substrates at 10 s before the end of the program. Then the samples were put on a preheated hotplate to annealed at 100 °C for 60 min. After the samples cooled down to room temperature, the Spiro-OMeTAD solution was dynamically spin-coated on the top of the perovskite at a speed of 3500 r. p. m. for 20 s. Finally, an 80-nm thickness gold layer (0.9 Å s^{-1}) was thermally evaporated on the Spiro-OMeTAD layer at a pressure of 1×10^{-6} bar. Then the devices were kept in the desiccator and measured regularly until the efficiency reached stable values.

4.4.4 Fabrication of electron-only device discussed in Section 7

The SnO_2 solution was spin-coated on cleaned ITO substrates at 4000 r. p. m for 30 s, followed by annealing at 170 °C for 30 min. For the ionic liquids-treated SnO_2 substrates (IM-perovskite), ionic liquids solutions with different concentrations dissolved in methanol were spin-coated on the SnO_2 substrates at 6000 r. p. m for 20 s, followed by annealing at 100 °C for 10 min in the glovebox. Afterward, the perovskite precursor solution was spin-coated on ITO/SnO_2 substrates at 1000 r. p. m for 5 s and 5000 r. p. m for 20 s and placed on a hotplate to annealed at 100 °C for 60 min. After the samples cooled down to room temperature, the PCBM solution was dynamically spin-coated on the top of the perovskite at a speed of 2000 r. p. m. for 30 s. Finally, an 80-nm thickness gold layer (0.9 Å s^{-1}) was thermally evaporated on the PCBM layer at a pressure of 1×10^{-6} bar.

4.4.5 Fabrication of hole-only device discussed in Section 7

The PTAA solution was spin-coated on cleaned ITO substrates at 4000 r. p. m for 25 s, followed by annealing at 100 °C for 10 min. Afterward, the perovskite precursor solution was spin-coated on ITO/SnO_2 substrates at 1000 r. p. m for 5 s and 5000 r. p. m for 20 s and placed on a hotplate to annealed at 100 °C for 60 min. After the samples cooled down to room temperature, the Spiro-OMeTAD solution was dynamically spin-coated on the top of the perovskite at a speed of 3500 r. p. m. for 20 s. Finally, an 80 nm thickness gold layer (0.9 Å s^{-1}) was thermally evaporated on the Spiro-OMeTAD layer at a pressure of 1×10^{-6} bar.

5 Sodium dodecylbenzene sulfonate used as surface passivator

This chapter is largely based on the following published article: "Sodium Dodecylbenzene Sulfonate Interface Modification of Methylammonium Lead Iodide as Surface Passivation of Perovskite Solar Cells" (Zou Y et al., ACS Applied Materials Interfaces, 2020, 12(47): 52643-52651, Doi.org/10.1021/acsami.0c14732). Adopted with permission from Ref [78]. Copyright [2020] American Chemical Society. In this chapter, the PL and TRPL was measured by Ali Buyruk, GIWAXS data was meausred by Tianxiao Xiao, FTIR data was measured by Lucas P. Kreuzer.

5.1 Preface

Lead-halide perovskite materials have recently attracted significant attention for their impressive optoelectronic properties including high absorption coefficients, high defect tolerances, and long charge carrier diffusion lengths. [79–83] Moreover, low-cost and large-scale fabrication is also an essential advantage for perovskite functional films to be considered as promising candidates in various optoelectronic applications. Benefiting from these favorable properties, PSCs presented remarkable PCE values and outstanding operational stability. [84–87] In the past decade, the PCE has significantly improved from 3.8 % to a certified PCE of 25.2 %, reflecting enormous development prospects and tremendous potential for commercialization. [88, 89]

However, for achieving real-world applications, the long-term stability of PSCs under ambient conditions in terms of thermal load, light, oxygen, and moisture exposure is still a huge challenge. [11, 90–93] The instability of PSCs mainly arises from the inherently unstable nature of perovskite materials caused by component degradation, [25] defect states, [94] and un-coordinated cations and anions (I^-, MA^+ and Pb^{2+}). [34, 95] The

commonly used methylammonium (MA^+) cation has relatively poor stability and is prone to degrade and volatilize, resulting in a deterioration of the active layer components. [96] On the other hand, the free lead ions have low formation energy and accumulate at the surface and grain boundaries, which is considered to be one of the main sources of defect states. [94] To effectively solve these stability issues, various methods have been employed such as compositional engineering, [96, 97] dimension regulation, [98–100] and surface passivation. [101–103] Among all methods, surface passivation has been regarded as an effective strategy to fabricate high-performance PSCs under ambient conditions with remarkable moisture stability. For example, Fu and Jiang et al. revealed that long-chain alkyl cations, such as BA^+, PEA^+, or $FPEA^+$, bind to the surface of the perovskite and thereby reduce the surface energy. This can play a dominant role in stabilizing the perovskite phase of the crystal structure. [44, 104] However, considering the short charge carrier diffusion lengths and insulating properties, the 2D structure may impair the charge carrier transport and decrease the device efficiency. [43, 105, 106] Previous literature reported that incorporating small molecules with special functional groups into the perovskite components can also result in a significant passivation effect. [107] Zheng and Huang et al. introduced a sulfonic zwitterion to simultaneously tune the perovskite crystallization behavior and to passivate defect states of perovskite thin films. Based on this approach, they obtained highly performing PSCs with good light stability and low defect density. [108] Therefore, passivating the detrimental defects accumulating at the grain boundaries and at the surface of the perovskite thin films and improving the longevity of the device by functionalizing the film surface with functional ligands is a promising approach.

In the present study, I demonstrated the fabrication of highly stable and efficient PSCs by interface modification and surface passivation with sodium dodecylbenzene sulfonate (SDBS). I illustrated that the SDBS surfactant not only improved the resistance of the perovskite film against moisture by its hydrophobicity but also interacted with un-coordinated lead ions by its sulfonic functional groups. The introduction of SDBS can simultaneously passivated defect states, facilitated charge carrier extraction, and reduced charge carrier recombination. By introducing SDBS, the PCE of the PSCs was increased from an average of 15.23 % (without SDBS) to 17.01 % (with SDBS). In addition, I introduce a dark storage test under the ISOS-D-1 condition. [109] It demonstrated the significantly enhanced tolerance of the PSCs against oxygen, moisture, and other aggressive atmospheric components naturally present in the air. The device maintained 80 % of the initial PCE of the PSCs after three months without device encapsulation.

5.2 Working principle of SDBS for perovskite surface passivation

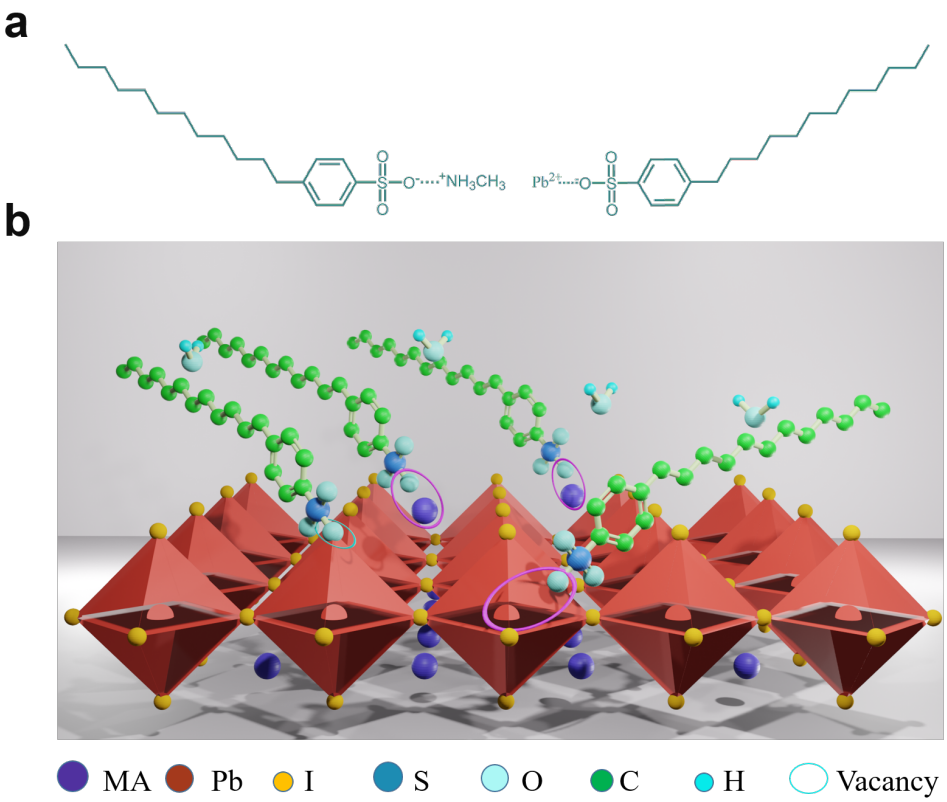

Figure 5.1: Schematic illustration of SDBS defect passivation. (a) Coordination between SDBS and MA^+, SDBS and Pb^{2+}. (b) SDBS molecules passivate defect states at grain boundaries at the film surface. Adopted with permission from Ref [78]. Copyright [2020] American Chemical Society.

SDBS was a typical anionic surfactant with a hydrophobic alkylphenyl group (long alkyl chain) and a hydrophilic sulfonic group ($-SO_3^-$). The molecular formula is $C_{18}H_{29}NaO_3S$, as seen in Figure 5.1a. SDBS was chosen as an additive to tune the perovskite crystallization and passivate the detrimental defects. As previously reported, the negatively charged sulfonic groups of SDBS can form complexes with un-coordinated Pb^{2+} and MA^+ existing on the surface of the perovskite thin film (Figure 5.1a). [108, 110, 111] The electrostatic interaction between $-SO_3^-$ and MA^+ causes the hydrophilic sulfonic group of the SDBS molecules to face the inside of the perovskite film, as shown in Figure 5.1b. This will result in a decrease of the surface tension between the EBL and the active layer, and increase the adhesion. [111–113] Due to the steric effects, the hydrophobic long alkyl chain aggregated

on the surface of perovskite film will point to the outwards for resisting the infiltration of external moisture, which improved the stability of the active layer components under humid ambient conditions. More importantly, the poor contact between the EBL (low polarization of the organic material) and the perovskite (high polarization) is not sufficiently conducive to obtaining high-performance PSCs. SDBS as an ambipolar passivation agent, with a polar part (-SO_3^-, good contact with polar perovskite surface) and a non-polar part (alkyl chain, contact with Spiro-OMeTAD), can greatly enhance contact between the polar perovskite and relatively lower polarized HTM. Thereby, SDBS minimized the barrier and accelerated the charge carrier transport, which was beneficial for obtaining high current densities. [114]

5.3 Solar cell characteristics

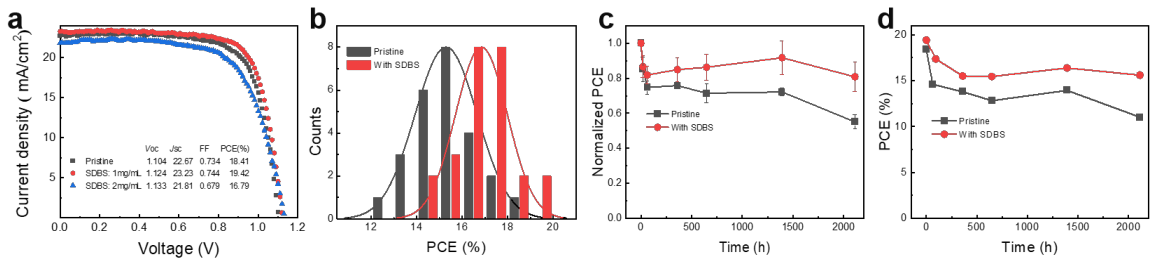

Figure 5.2: (a)*J–V* characteristics of champion MAPI devices without (black) and with (red) SDBS passivation. (b) power conversion efciency (PCE) distribution of the devices based on 25 solar cells and (c) average photovoltaic performance of non-encapsulated MAPI devices in ambient environment as a function of storage time based on 4 solar cells. (d) Photovoltaic performance of the champion PSCs without (black) and with (red) SDBS passivation as a function of storage time in ambient environment. Adopted with permission from Ref [78]. Copyright [2020] American Chemical Society.

MAPI was selected to investigate the effect of SDBS on device performance. SDBS (1 and 2 mg/mL) was deposited on the surface of the MAPI thin films followed by an annealing step to prepared PSCs with SDBS modification. The current-voltage (*J*-*V*) characterizations of the champion pristine and SDBS modified PSCs as measured under AM 1.5G illumination were shown in Figure 5.2a.

The best-performing pristine device shown a PCE of 18.41 % with an V_{OC} of 1.10 V, a J_{SC} of 22.67 mA cm^{-2}, and a FF of 0.74. The PSC treated with 1 mg/mL SDBS shown improved performance with a champion PCE of 19.42 % due to an enhanced V_{OC} of 1.12 V, a J_{SC} of 23.23 mA cm^{-2}, and an FF of 0.75. With the SDBS concentration further

increased, the device performance started to deteriorate. The PSC treated with 2 mg/mL SDBS shown a poor PCE of 16.79 %.

The statistical distribution of the PCE of the PSCs with and without SDBS (1 mg/mL) modification based on 25 devices were shown in Figure 5.2b. The average PCE significantly increased from 15.23 % to 17.01 % after the SDBS modification. Moreover, the width of the PCE distribution was narrowed by the SDBS modification, which indicated that the reproducibility was improved. Besides the device efficiency characterization, I further investigated the stability of non-encapsulated devices under ISOS-D-1 conditions. The PCE tracking based on four devices (Figure 5.2c) shown a significant improvement in stability for the SDBS-modified PSCs. The SDBS-modified PSCs retained 80 % of their initial average PCE for up to 2112 h, whereas the pristine PSCs retained only 55 % under these conditions. In particular, at the beginning of the stability test, the pristine PSCs suffered from a serious decrease in PCE. The stability test of the champion devices confirmed these findings as shown in Figure 5.2d. The improved ambient stability of the SDBS-modified PSCs was attributed to the hydrophobic character of SDBS long alkyl chains. [113]

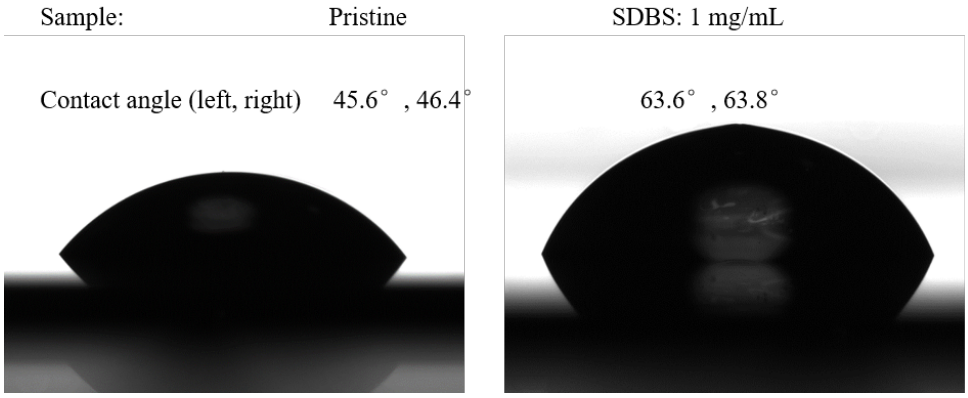

Figure 5.3: Contact angle measurement of glycerol on MAPI films without SDBS (left) and with (right) SDBS passivation. Adopted with permission from Ref [78]. Copyright [2020] American Chemical Society.

With contact angle measurements, the changed hydrophobicity was evaluated. The contact angles were measured with glycerol, also a common polar solvent, instead of water, considering that water will accelerate the degradation of perovskite components by causing chemical modification. [115, 116] As seen in Figure 5.3, the contact angle of the perovskite film increased from 46.0° to 63.7° after SDBS passivation, which means that SDBS can improve the film resistance against moisture. These findings were in good agreement with previous reports. [108, 117, 118]

5.4 Optoelectronic characterization

To verify the coordination between sulfonic groups and lead ions on the perovskite surface, Fourier-transform infrared (FTIR) spectroscopy measurements were done on MAPI films without and with SDBS modification (Figure 5.4a). SDBS was measured as a reference as well. Thereby, the peaks appearing in the spectra at 2858 cm^{-1} and 2926 cm^{-1} were assigned to the asymmetric and symmetric -CH_2 stretching from SDBS. The peaks located at 1046 cm^{-1} and 1191 cm^{-1} were attributed to the S=O stretching from the sulfonic group of SDBS. Different from the pristine sample, these peaks were also found in the FTIR spectra of the SDBS-modified MAPI films, which proofed that SDBS remained on the surface of the perovskite layer. The peak located at 1010 cm^{-1} was attributed to the coordination complex between Pb^{2+} and the S-O stretching vibrations from SDBS, where the oxygen in the sulfonic group contains two lone electron pairs and the 6p orbitals of Pb contain empty orbitals. Compared to pure SDBS that the stretching vibration peak position of S-O was located at 1012 cm^{-1}, there was a slight shift in the peak position by -2 cm^{-1}, which can be attributed to the complexation in the perovskite layer. Hence, the S-O^- could provide lone electron pairs to occupy the empty orbitals of Pb, which given rise to a coordination complex and inhibited the formation of morphological defects during the processing of the perovskite film. [108, 110]

To explore the impact of SDBS on the active layer band gap, I measured UV-vis absorption spectra of the MAPI films without and with SDBS modification (Figure 5.4b). I compared two different SDBS concentrations (1 and 2 mg/mL). A slight red-shift occurred in the UV-vis spectra for the SDBS passivated perovskite films, which increased with SDBS concentration increase, as shown in the inset in Figure 5.4b. Thus, the SDBS modification decreased the band gap of the perovskite thin film. To further confirm the influence of SDBS on the apparent band gap of the perovskite layer, I collected steady-state PL, as seen in Figure 5.4c. The red-shift in the PL increased with an increasing amount of SDBS. After SDBS passivation, the PL peak position red-shifted about 10 nm, which indicated that the SDBS passivated sample has a lower optical band gap and consequently allowed for more light absorption than the pristine MAPI sample from the sunlight spectrum. Moreover, the 1 mg/mL SDBS passivated MAPI films exhibited a large rise in the steady-state PL intensity in comparison to the pristine film and if 2 mg/mL SDBS was used. Thus, a moderate amount of SDBS (1 mg/mL) significantly reduced the trap state density acting as non-radiative recombination centers in the MAPI film, which will contribute to the improved FF of the PSCs. Using an excess of SDBS (2 mg/mL) introduced additional defects, which counterbalance the reduction of trap states.

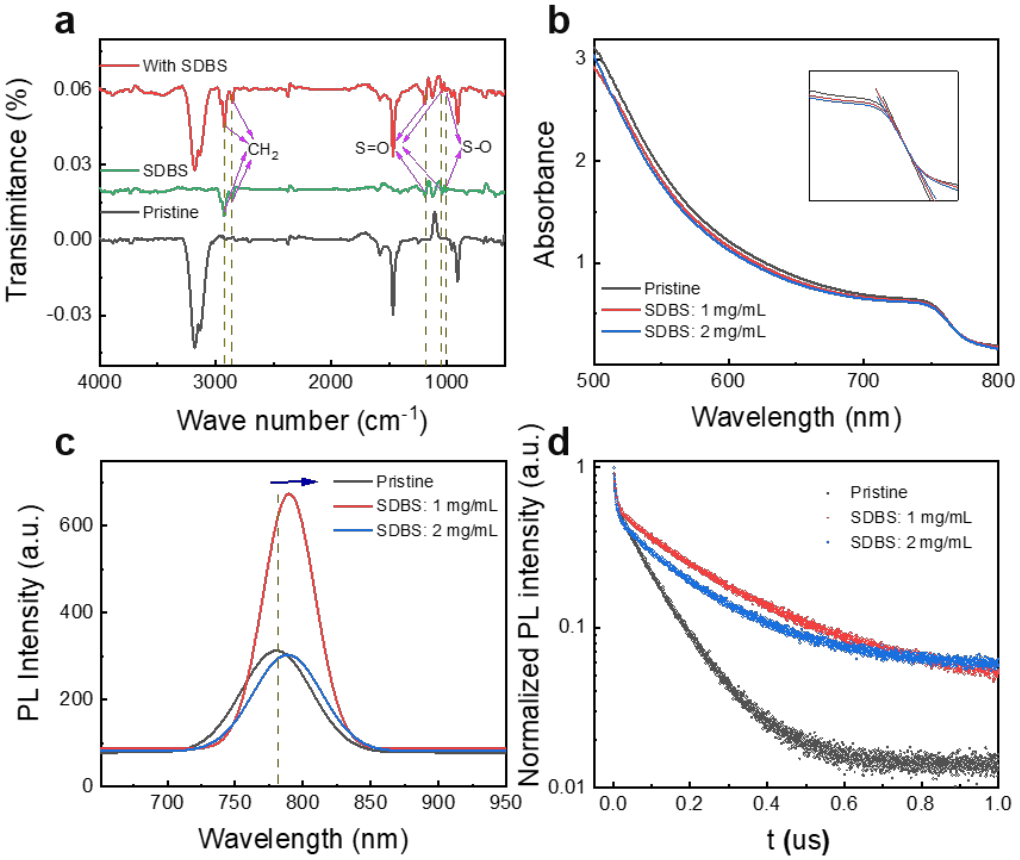

Figure 5.4: (a) FTIR spectra of MAPI (black), pure SDBS (green), and MAPI passivated with SDBS (1 mg/mL). The spectra were shifted along the y axis for clarity. The dashed lines indicated the stretching vibration peak of CH_2 and the asymmetric S=O stretching vibration. (b) UV-vis absorption spectra, (c) steady-state PL spectra and (d) time-resolved photoluminescence (TRPL) decay of MAPI films without (black) and with SDBS treatment (1 mg/mL in red, 2 mg/mL in blue). The fits to the TRPL data were shown with grey lines using a biexponential rate law. Adopted with permission from Ref [78]. Copyright [2020] American Chemical Society.

To study the charge carrier recombination dynamics and compare the trap density of the perovskite films, TRPL measurements were performed (Figure 5.4d). The TRPL curves were fitted with a bi-exponential decay function, which was composed of two parts: the fast-decay component τ_1 and the slow-decay component τ_2. [64, 119] The fit results were obtained when using the following equation

$$I_{pl} = A_1 \exp(-\frac{t}{\tau_1}) + A_2 \exp(-\frac{t}{\tau_2}) \tag{5.1}$$

where A_i refers to the fractional amplitude and τ_i refers to the time constant of the

exponential functions were shown in Table 5.1. [64] The average lifetimes were calculated and listed in Table 5.1 through the following equation

$$\tau_{ave} = (A_1\tau_1^2 + A_2\tau_2^2)/(A_1\tau_1 + A_2\tau_2) \tag{5.2}$$

The amplitude of the fast decay component (A_1) increased from 29.2 % to 45.5 % with increasing SDBS amount, accompanied by a minor decrease in the related time constant (τ_1). The amplitude of the slow decay component (A_2) decreased from 70.8 % to 55.5 % and the time constant (τ_2) increased from 103 ns to 251 ns for the SDBS passivated films. These changes indicated that the SDBS modification on the one hand was the origin of additional defects itself, but on the other hand also effectively passivated some deeper defects of the pure MAPI, which caused the increase in the amplitude A_1 and a decrease in the lifetime τ_1. For further illustration, I also calculated the average lifetime τ_{ave} (Table 5.1). The τ_{ave} values for samples with 0, 1, and 2 mg/mL SDBS passivation were 98.83, 244.67, and 192.53 ns, respectively. The increase in the average lifetime of SDBS passivated films mean that the defects in the perovskite film were significantly passivated and that charge carrier trapping was strongly suppressed. Thus, the SDBS modification effectively reduced the trap-density and suppressed the charge carrier recombination. In more detail, using 1 mg/mL SDBS was more beneficial than 2 mg/mL as excess SDBS acted as defects by itself. With respect to PSCs, the longest τ values were beneficial for the device performance due to the better balance between defect passivation and charge carrier collection, which demonstrated that 1 mg/mL SDBS was the best-suited amount for gaining an improved PCE.

Sample	Without SDBS	SDBS: 1mg/mL	SDBS: 2mg/mL
A_1	29.2±0.1	38.2±0.1	45.5±0.1
τ_2	12	11	10
A_2	70.8±0.1	61.8±0.3	55.5±0.2
τ_2	103	251	200
τ_{ave}	98.83	244.67	192.52

Table 5.1: Fit parameters of the TRPL data using a biexponential decay model. Adopted with permission from Ref [78]. Copyright [2020] American Chemical Society.

5.5 Structure characterization

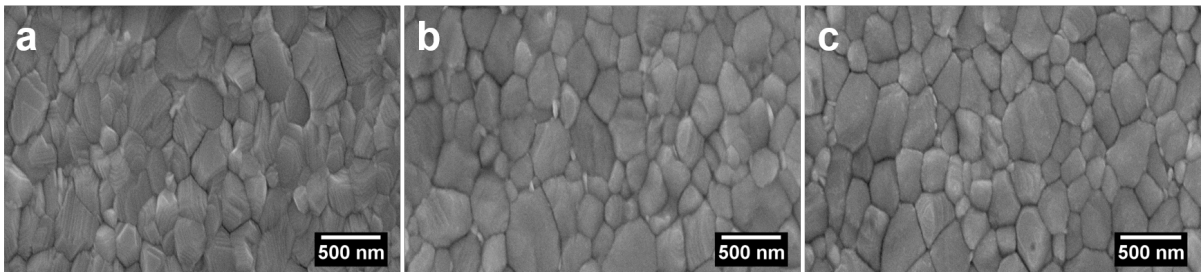

Figure 5.5: Scanning electron microscopy (SEM) images of the MAPI films prepared (a) without and with SDBS treatment using a concentration of (b) x = 1 and (c) x = 2 mg/mL. Adopted with permission from Ref [78]. Copyright [2020] American Chemical Society.

The effect of SDBS on the morphology of the perovskite films was probed with top-view SEM, as shown in Figure 5.5. Only minor changes were seen with SEM. Thus, the SDBS surface passivation did not affect the surface morphology of the perovskite films.

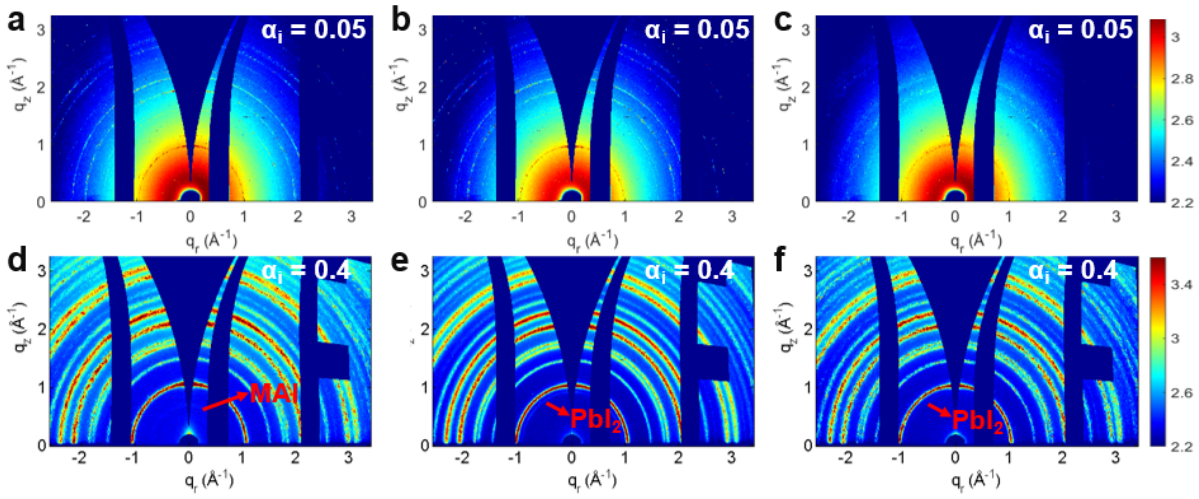

Figure 5.6: 2D GIWAX data of MAPI films with different SDBS concentrations: (a,d) 0 mg/mL, (b,e) 1 mg/mL and (c,f) 2 mg/mL measured at an incident angle (a-c) $\alpha_i = 0.05°$ and (d-f) 0.40°. Adopted with permission from Ref [78]. Copyright [2020] American Chemical Society.

GIWAXS was used to study the crystal structure of perovskite thin films. [120–122] The 2D GIWAXS data were shown in Figure 5.6. The GIWAXS data were collected at two different incident angles ($\alpha_i = 0.05°$ and 0.40°) to realize two different penetration depths of the X-rays providing surface-sensitive and volume-sensitive structure information, respectively. [123] Irrespective of the SDBS treatment, the diffraction patterns shown

pronounced intensity rings of the tetragonal MAPI perovskite structure, e.g. at q = 1.03 $Å^{-1}$ and q = 2.08 $Å^{-1}$. [124] The diffraction rings of SDBS passivated MAPI films exhibited a relatively more homogeneous azimuthal intensity distribution at q = 1.03 $Å^{-1}$ compared with the pristine MAPI film, indicating that SDBS passivation promoted the isotropic orientation distribution of the crystallites on the expense of the face-up orientation. [125]

The tube cuts performed along q = 1.03 $Å^{-1}$ contain the (002) and (110) Bragg peaks, which correspond to the Debye-Scherrer rings formed from the reflection of the (002/110) lattice planes of the MAPI crystals. For further analysis, the azimuthal intensity distributions were fitted with a Gaussian function, in which standard deviation (σ) was used to describe the orientation distribution width.

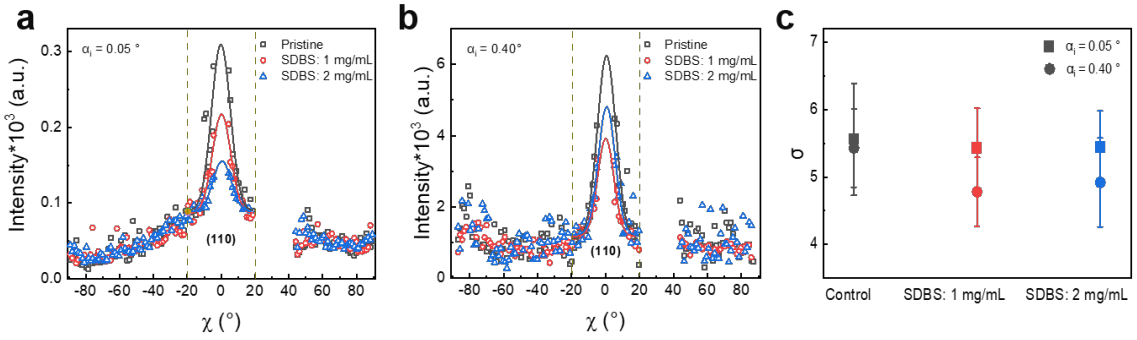

Figure 5.7: Tube cuts of the 2D GIWAXS data in case of (a) α_i = 0.05° and (b) α_i = 0.40° of the (002/110) Bragg peak around q =1 $Å^{-1}$ for the MAPI films without (black rectangles) and with 1 mg/mL (red circles) and 2 mg/mL (blue triangles) SDBS. The solid lines are fits based on a Gaussian function with the dashed lines indicate the fitting region. c) Corresponding azimuthal widths from the Gaussian fits in case of α_i = 0.05° (rectangular symbols) and α_i = 0.40° (circle symbols). Adopted with permission from Ref [78]. Copyright [2020] American Chemical Society.

As shown in Figures 5.7a and b, all films shown a preferential orientation around χ= 0°, meaning that the crystals were predominantly adopting a face-up orientation instead of an edge-on orientation. Herein, I also made a statistical analysis of the width of the orientation distribution (Figure 5.7c). At α_i = 0.05°, the scattering signal reflected structure information from the surface-near region. [126] The azimuthal peak widths did not change significantly from 5.56° ± 0.83, 5.43° ± 0.59 to 5.44° ± 0.54 for the samples with 0, 1, and 2 mg/mL SDBS, respectively (Figure 5.7c), implying that the crystal orientations did not change with increasing SDBS concentration. In contrast, at α_i = 0.40°, due to the larger penetration depth, the scattering signal given the information on the entire perovskite film. The azimuthal σ values were 5.43° ± 0.58, 4.78° ± 0.51, and 4.92° ± 0.66

for the samples with 0, 1, and 2 mg/mL SDBS, respectively (Figure 5.7c). This decrease in the azimuthal σ values indicated that the crystal orientation was more narrowly spread inside the perovskite film after SDBS passivation. Thus, the SDBS passivation effected the crystal orientation of the crystals located deeper inside the perovskite films and has only a slight effect on the crystals located in the surface-near. I attributed the applied soaking time before spin coating SDBS and the thermal annealing after spin coating to enable the penetration of SDBS inside the perovskite film, instead of only staying on the perovskite film surface.

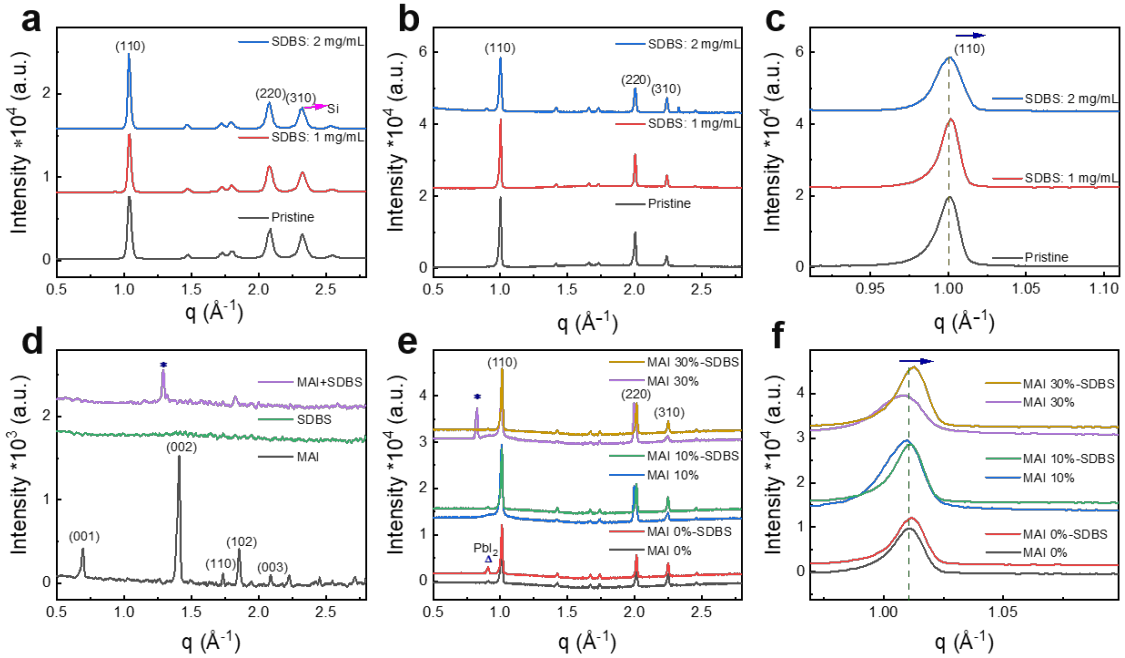

Figure 5.8: (a) Pseudo XRD data obtained from GIWAXS data integration and (b) XRD data for MAPI films without (black) and with 1 mg/mL (red) and 2 mg/mL (blue) SDBS. (c) Zoom-in to XRD pattern at the (110) Bragg peak of MAPI films without (black) and with SDBS passivation using a concentration of x= 1 (red) and 2 mg/mL (blue). (d) XRD data of pure MAI (grey), pure SDBS (green) and MAI with SDBS (purple) films. (e) XRD patterns of the MAPI films prepared with excess MAI as indicated without and with SDBS (1 mg/mL). (f) Zoom-in to XRD pattern at the (110) Bragg peak of MAPI films prepared with excess MAI as indicated without and with SDBS (1 mg/mL). Adopted with permission from Ref [78]. Copyright [2020] American Chemical Society.

It was worth noting that additional diffraction signals were found in the GIWAXS data of the pristine and the SDBS-modified perovskite films, respectively. The intensity rings located near q = 0.69 $Å^{-1}$ and q = 0.91 $Å^{-1}$ positions were attributed to the methylammonium iodide (MAI) (001) and PbI_2 (001) Bragg peaks, respectively (Figure 5.6). [127]

With SDBS modification, the MAI ring disappeared while the PbI_2 ring appeared. Hence, I hypothesized that the residual MAI may be consumed by SDBS, because the negatively charged benzenesulfonic acid ion of SDBS can easily coordinate with the positively charged MA^+ to form complexes.

By performing an azimuthal integration, I achieved pseudo-X-ray diffraction (XRD) data (Figure 5.8a). The Bragg peaks at q = 1.03 $Å^{-1}$ and q = 2.08 $Å^{-1}$ arising from the (110) and (220) lattice plane reflections of the perovskite crystals were well visible. The peak located at q = 2.32 $Å^{-1}$ was assigned to the Si peak. Irrespective of the SDBS treatment, the peak intensities and widths did not change significantly. Due to the missing wedge in GIWAXS, the pseudo-XRD data were complemented with XRD measurements (Figure 5.8b). I observed the same Bragg peaks from the tetragonal MAPI perovskite structure, which was in good agreement with the literature. [124] The position of the (110) Bragg peak shifted slightly towards higher q values (Figure 5.8c) in the case of SDBS-treated samples, which indicated that the lattice constants changed by 0.08 % after SDBS treatment. The smaller lattice constant was attributed to the penetration of SDBS into the active layer, which squeezed the perovskite crystal and impacts deep defects.

To confirm the reaction between SDBS and MA^+, XRD patterns of pure MAI, pure SDBS, MAI, and SDBS mixed films were measured and the results were shown in Figure 5.8d. The Bragg peaks located at 0.70 $Å^{-1}$, 1.41 $Å^{-1}$ and 1.86 $Å^{-1}$ belonged to MAI. [128, 129] After SDBS passivation, a new peak marked with an asterisk (*) appeared at 1.29 $Å^{-1}$. I attributed this peak to complexes, which were formed by the reaction between MAI and SDBS. To further study the interactions of SDBS and MAI, I also measured XRD of MAPI films doped with 0 %, 10 %, and 30 % MAI excess under the same SDBS concentration treatment (1 mg/ml), as shown in Figure 5.8e. Again, I found the Bragg peaks from the tetragonal MAPI perovskite structure. The small peak located at q = 0.91 $Å^{-1}$ (marked with a blue triangle) was assigned to unreacted PbI_2. Previous literature reported that a small amount of PbI_2 can passivate the defect states and improve the performance of PSCs. [130,131] In addition, I seen a peak located at q = 0.83 $Å^{-1}$ (marked with a blue asterisk) which did not match either the pure PbI_2 or MAI tetragonal phase. According to the literature, this peak can be assigned to the $(MA)_4PbI_6$ phase. [132] With the MAI concentration increase, the PbI_2 peak disappeared and the peak located at q = 0.83 $Å^{-1}$ appeared. After SDBS passivation, the peak disappeared. This finding can be well explained by an interaction of SDBS and MA^+, resulting in a reduced number of defect states caused by free MA^+ ions. In addition, as seen in Figure 5.8f, the peak at q = 1.01 $Å^{-1}$ shifted towards higher q values after SDBS passivation, which was in good agreement with previous results (Figure 5.8c).

It was worth mentioning that an indication of a phase transition was seen at (220)

Bragg peak of the MAPI film with excess MAI, as seen in Figure 5.9. [133, 134] The two Bragg peaks indexed with (004) and (220) were located at q = 1.97 $Å^{-1}$ to 2.04 $Å^{-1}$ signified the tetragonal phase of the MAPI perovskite. They appeared with increasing MAI content. [135, 136] After SDBS treatment, these peaks disappeared and merged to the (200) Bragg peak of the cubic phase at q = 2.01 $Å^{-1}$ (Figure 5.9). Thus, SDBS can stabilize the cubic phase of the perovskite and inhibit the transformation of the cubic phase to the tetragonal phase.

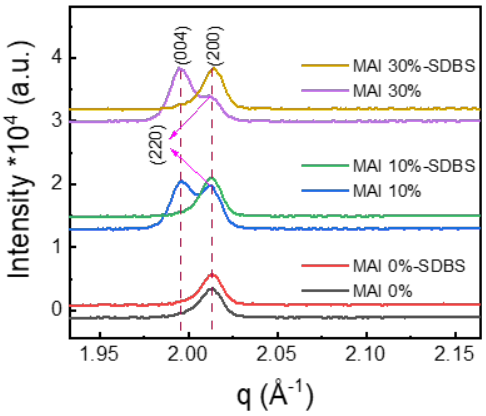

Figure 5.9: Zoom-in to XRD pattern at the (220) Bragg peak of MAPI films prepared with excess MAI as indicated without and with SDBS (1 mg/mL). Adopted with permission from Ref [78]. Copyright [2020] American Chemical Society.

5.6 Summary

In summary, I demonstrated the role of an anionic surfactant with long-alkyl-chain in improving optoelectronic properties by suppressing trap-state density and controlling the crystal orientation. The incorporation of SDBS additive can effectively passivate defects with the strong interaction between Pb^{2+} and the sulfonic group ($-SO_3^-$), and improve the ambient stability by a hydrophobic alkyl-phenyl group. Benefiting from the excellent properties of SDBS, the PCE of the SDBS-treated PSCs was further improved to over 19 % for our champion device. Moreover, also the ambient stability was significantly improved by the SDBS passivation. Under ambient conditions (30-40 % relative humidity), 80 % of its initial efficiency remained for the SDBS-treated PSCs after 2112 hours without encapsulation. Thereby, our work represented an economic pathway towards the manufacturing of high-performance PSCs in combination with the high stability of the devices.

6 Influence of CsBr doping on Crystal Orientation and Optoelectronic Properties

This chapter is largely based on the following published article: "The Influence of CsBr on Crystal Orientation and Optoelectronic Properties of $MAPbI_3$-Based Solar Cells" (Zou Y et al., ACS Applied Materials Interfaces, 2022, 14(2): 2958-2967, Doi.org/10.1021/acsami.1c22184). Adopted with permission from Ref [137]. Copyright [2022] American Chemical Society. In this chapter, TPV and TPC were measured by Shuai Yuan, UPS was measured by Johanna Eichhorn, SEM data was measured by Shanshan Yin,TRPL data was measured by Buyruk Ali, GIWAXS data was measured by Tianxiao Xiao, Manual A. Scheel, and Shambhavi Pratap, SEM-EDS was measured by Christian L. Weindl.

6.1 Preface

Metal halide perovskite-based solar cells with the general formula ABX_3 (A represents cation: methylammonium (MA^+), formamidinium (FA^+) or cesium (Cs^+); [10,45] B represents the divalent metal cation: Pb^{2+}, Sn^{2+} or Ge^{2+}; [92] and X represents the halide anion: Cl^-, Br^-, or I^- [138–140]) have captured considerable attention as superior light harvesters. These materials are regarded as excellent candidates for energy conversion due to their outstanding optoelectronic features including tunable bandgap, [111,141] low exciton binding energy, [142,143] and excellent ambipolar charge carrier transport properties. [144] In recent years, PSCs attained remarkable achievements in the field of solar energy conversion and PCE have increased from a value of 3.9 % to certified 25.5 %, coupled with promising long-time operational stability. [88,145] This rapid progress rendered PSCs not only interesting in terrestrial applications but also for use in space. [146]

Despite the huge development prospect, PSCs inevitably face dilemmas for further boosting their photovoltaic efficiency. [83] The performance of perovskite-based devices is mainly determined by the film preparation conditions, which impact the resulting structural, electronic, and optical properties of the materials. [124] Perovskites typically form polycrystalline thin-films and various detrimental defects can unavoidably manifest during the rapid crystallization process of the films, resulting in a higher defect density compared to their monocrystalline counterparts. [147–149] These defects tend to accumulate at interfaces and grain boundaries, causing non-radiative recombination, which significantly hinders the effective transport and extraction of photo-generated charge carriers. [116,150] To obtain effective photo-generated charge carrier transport and extraction, most investigations have thus far emphasized the optimization of grain size and crystallinity during the perovskite thin-film deposition process. [103, 137, 151] For instance, Huang et al. adopted solvent annealing to increase the grain size and crystallinity of the perovskite films, resulting in significant improvement of the electronic properties. [152] Top-down approaches to single crystal perovskite solar cells suffer from challenges introduced by the crystal size compared with the needed device areas. [153] However, a significant knowledge gap exists in understanding the role of the microstructure of these materials from colloidal precursors in solution on the behavior of photo-generated charge carriers. [154] It was reported that distinct differences exist in the growth orientation of different grains in a polycrystalline perovskite film, which was reflected in the anisotropy of charge carrier lifetimes and trap density distributions. [20, 155] If the grains grew preferentially along a particular crystallographic plane, an extraordinary charge carrier mobility was observed along a certain crystallographic direction. [156] Therefore, it is necessary to gain a profound insight into the underlying relationship between the crystal orientation distribution and the charge carrier transport for further improving the photovoltaic performance of perovskite devices.

In the present work, I doped the classical perovskite MAPI with different concentrations of CsBr to form a mixed cation perovskite. Distinct from the previous study that explore the defect passivation capabilities of CsBr, [157] I emphasized the influence of CsBr addition on the preferred orientation distribution of the crystallites forming the thin perovskite film. I focused on the crystal microstructure, as probed via GIWAXS measurements. In combination with TPC, TPV, and trap density of states (tDOS) measurements, I conducted an in-depth analysis on the interplay of the crystal orientation, charge carrier dynamics, and resulting optoelectronic properties of perovskite devices. Upon the incorporation of CsBr, the absorber layers exhibit a preferential crystal orientation distribution with a significant crystalline order and superb charge carrier transport properties, accompanied by a reduced charge carrier recombination. Due to the superior

optoelectronic quality, the prepared PSC based on MAPI-CsBr mixed perovskite delivers a remarkable PCE of 19.24 % and a high open-circuit voltage V_{OC} of up to 1.15 V.

6.2 The structure and preparation of perovskite solar cells

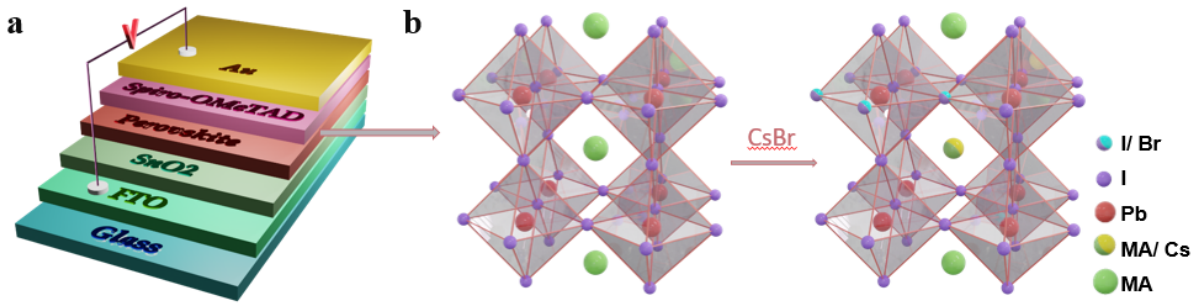

Figure 6.1: Schematic diagram of (a) the configuration of the fabricated PSCs (from bottom to top): Glass/ITO/SnO_2/perovskite/spiro-OMeTAD/Au and (b) the evolution of active layer component after doping the perovskite crystal with CsBr. Adopted with permission from Ref [137]. Copyright [2022] American Chemical Society.

The PSCs were fabricated in the common device configuration of ITO/SnO_2/perovskite/Spiro-OMeTAD/Au, as illustrated in Figure 6.1a. In terms of the active layer, I prepared the mixed perovskite components based on MAPI as the host by tuning the molar ratio of MAI: CsBr, as schematic in Figure 6.1b. Two molar ratios of MAI: CsBr (97: 3 and 94: 6) were prepared to compare, corresponding to the mixed perovskite components $(CsPbBr_3)_3$ $(MAPbI_3)_{97}$ and $(CsPbBr_3)_6$ $(MAPbI_3)_{94}$, denoted as MAPI-3 % CsBr and MAPI-6 % CsBr, respectively. The perovskite films were spin-coated by the conventional one-step solution process with CB as the antisolvent (the detailed preparation procedure can be found in the sample preparation section 4.4.2). [110]

6.3 Morphology of perovskite films

The morphology of the perovskite films is key to the photovoltaic performance of the respective PSCs. Generally, compact, smooth, and pinhole-free films are considered to have relatively low defect concentrations and superior photovoltaic performance. SEM

was applied to evaluate the surface morphology of the perovskite films doped with CsBr. As shown in Figures 6.2a and b, all films have a homogeneous, and compact morphology and a high surface coverage with crystal sizes in the range of hundreds of nanometers. No additional smaller grains were discernable inside the crystals. [158] Notably, the grain size distributions were summarized in Figures 6.2c and d, the grain sizes slightly increase upon the incorporation of CsBr, which typically implied fewer grain boundaries and less photo-generated charge carrier losses. In addition, an obvious difference in surface texture can be observed for the MAPI and MAPI-CsBr films. It was reported that such a layered texture morphology can effectively eliminate shunting paths and diffuse reflectance losses, thereby leading to an enhanced performance of the devices. [159]

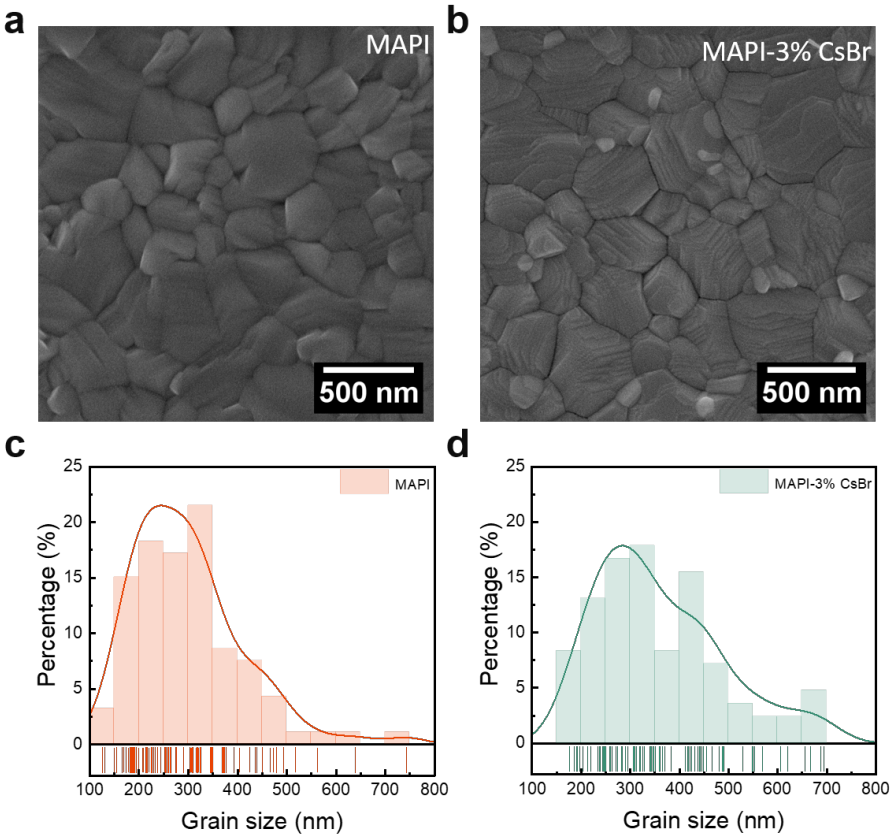

Figure 6.2: Top-view SEM images of (a) MAPI and (b) MAPI-3 % CsBr. The statistical grain size distribution of (c) MAPI and (d) MAPI-3 % CsBr films. Adopted with permission from Ref [137]. Copyright [2022] American Chemical Society.

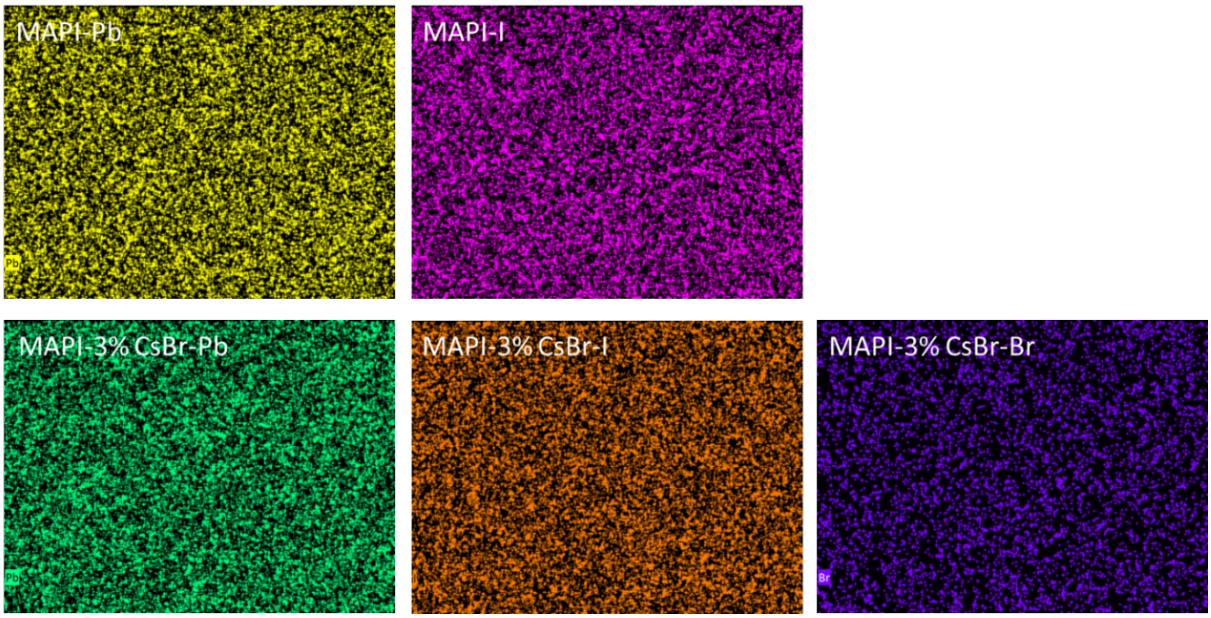

Figure 6.3: EDS mapping of Pb, I and Br component distribution in the MAPI and MAPI-3 % CsBr films. Adopted with permission from Ref [137]. Copyright [2022] American Chemical Society.

To verify the distribution of elements in the films, the elemental mapping and X-ray energy dispersive spectroscopy (EDS) analysis were performed for the MAPI and MAPI-CsBr films, as shown in Figure 6.3. As observed from the elemental mapping images of Pb, I, and Br, I confirmed that the three elements were uniformly distributed in the bulk and surface of the perovskite film. Moreover, the relative atomic ratios were determined, as shown in Figures 6.4a and b, indicating that Br was successfully incorporated into the film from the precursor solution.

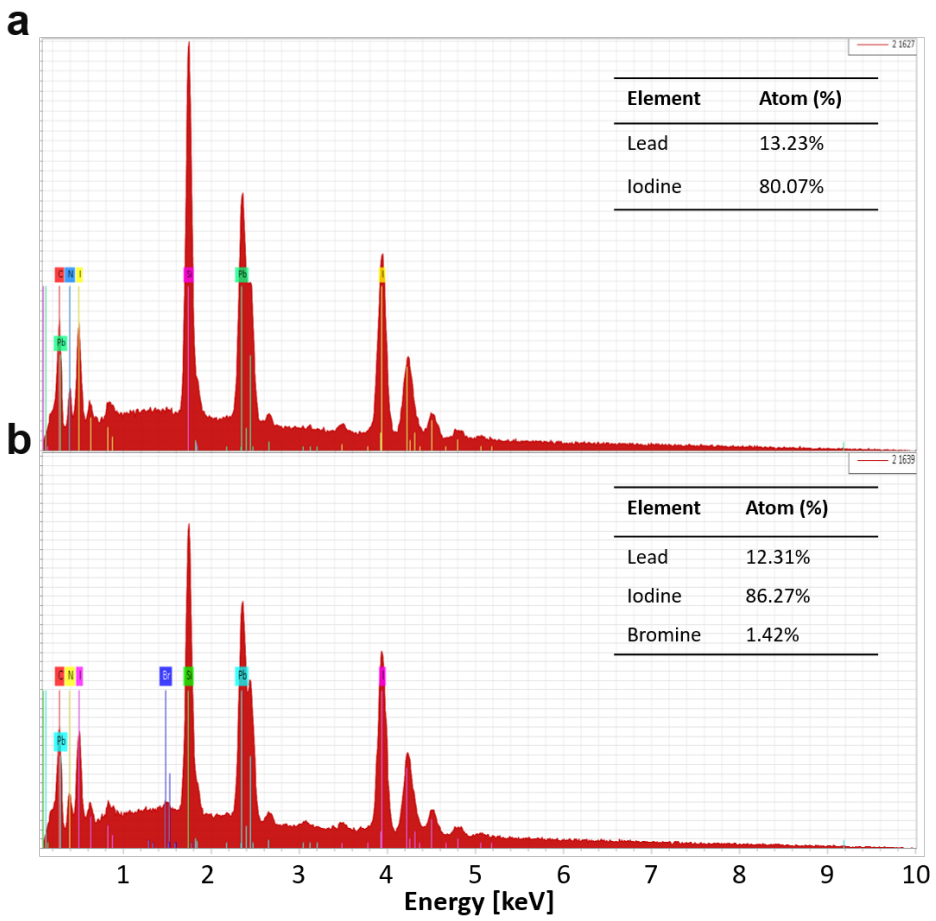

Figure 6.4: EDS data and corresponding Pb, I and Br atomic ratios of the (a) MAPI and (b) MAPI-3 % CsBr films. Adopted with permission from Ref [137]. Copyright [2022] American Chemical Society.

6.4 Crystal structure of perovskite films

XRD characterization was used to examine the crystal structure and crystallinity of perovskite films (Figure 6.5). The major peaks located at around 14.10°, 28.50°, and 31.90° were assigned to the (110), (220), and (310) Bragg peaks, respectively. All mixed perovskite films display the characteristic peaks of the tetragonal perovskite structure, illustrating the successful formation of α-phase MAPI. The relative intensities of the (220) and (310) Bragg peaks were nearly constant with respect to the corresponding (110) Bragg peak for all perovskite films, indicating that no significant preferential growth occurs with the incorporation of CsBr. However, the absolute Bragg peak intensities of the MAPI and MAPI-3 % CsBr films shown significant differences. With the incorporation of CsBr,

the intensities of the (110), (220) and (310) Bragg peaks become higher than for the case of the MAPI film. The detailed FWHM values of the diffraction peaks of the MAPI and MAPI-3 % CsBr films were shown in Table 6.1.

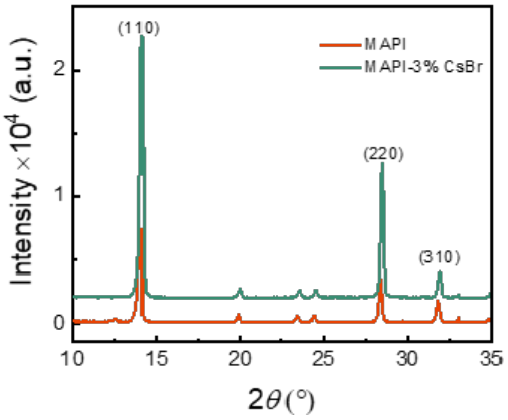

Figure 6.5: XRD data of MAPI (red) and MAPI-3 % CsBr (green). Adopted with permission from Ref [137]. Copyright [2022] American Chemical Society.

Sample	MAPI	MAPI-3 %CsBr
(001)/(110)	0.20	0.18
(220)	0.21	0.20
(310)	0.22	0.22

Table 6.1: FWHM values of characteristic Bragg peaks of the MAPI and MAPI-3 % CsBr films obtained from Gaussian fits. Adopted with permission from Ref [137]. Copyright [2022] American Chemical Society.

The lower FWHM values extracted from the Bragg peaks of the MAPI-3% CsBr film suggested that the incorporation of CsBr increases the crystal size in addition to enhance the crystallinity of the perovskite film. [160, 161] The formation of the perovskite films occurs via the combination of nucleation and crystal growth processes. When CsBr was incorporated into the perovskite precursor solution, the Br^- and Cs^+ can influence the crystallization behavior and prolong the crystallization kinetics of the perovskite films, which was beneficial for obtaining highly crystalline perovskite films with large grains. [162, 163]

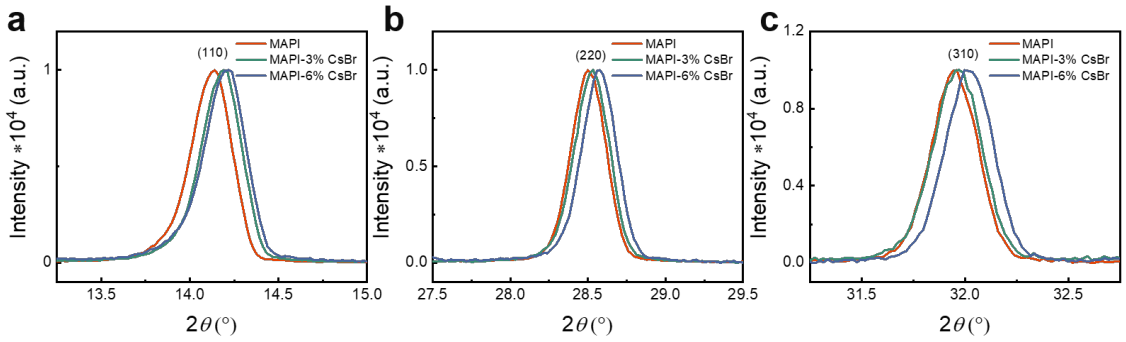

Figure 6.6: Zoom-in of XRD data of the (a) (110), (b) (220) and (c) (310) Bragg peak of the MAPI (red), MAPI-3 % CsBr (green) and MAPI-6 % CsBr (blue) perovskite films. Adopted with permission from Ref [137]. Copyright [2022] American Chemical Society.

Moreover, the peak positions of the (110), (220) and (310) Bragg peaks exhibited the same tendency to shift towards higher angles and the shift was proportional to the CsBr-doping content, as shown in Figure 6.6. The specific diffraction peak locations of the corresponding crystallographic planes were summarized in Table 6.2.

Sample	MAPI (°)	MAPI-3 %CsBr (°)	MAPI-6 %CsBr (°)
(001)/(110)	14.12	14.17	14.19
(220)	28.50	28.52	28.53
(310)	31.94	31.96	31.97

Table 6.2: Bragg peak positions in 2theta of the MAPI, MAPI-3 % CsBr and MAPI-6 % CsBr films. Adopted with permission from Ref [137]. Copyright [2022] American Chemical Society.

According to previous reports, [164] the formation of perovskite was estimated by the tolerance factor

$$t = \frac{R_A + R_X}{\sqrt{2}(R_B + R_X)} \tag{6.1}$$

where R_A, R_B and R_X are the ionic radii of A, B and X (for the perovskite structure ABX_3). When smaller extrinsic Cs^+ ions (Cs^+:1.69 Å, MA^+: 2.17 Å) were introduced into the MAPI-based perovskite, the tolerance factor (t) was changed and thus the crystal structure of the ABX_3 perovskite was influenced. The calculated tolerance factors of different perovskite compositions were shown in Table 6.3.

Perovskite	MAPI	MAPBr	CsPI	CsPBr
Tolerance factor (t)	0.91	0.93	0.81	0.82

Table 6.3: Tolerance factor of different perovskite compositions. (MA^+: 2.17, Cs^+: 1.69, Pb^{2+}: 1.19, I^-: 2.2, Br^-: 1.96). Adopted with permission from Ref [137]. Copyright [2022] American Chemical Society.

A change in the tolerance factor can inevitably lead to a mismatch of the crystal lattice constant and explain the observed peak shifts in the XRD characterization. [165] Therefore, the gradual shift of the characteristic peaks of the perovskite phase to higher diffraction angles can be attributed to the substitution of the vacant MA^+ and I^- sites in the host perovskite by Cs^+ and Br^-, which have smaller ionic radii, thereby decreasing the residual stress and decreasing the lattice constant. [157] Thus, it was suggested that CsBr is integrated into the perovskite lattice.

6.5 Optical properties of perovskite films

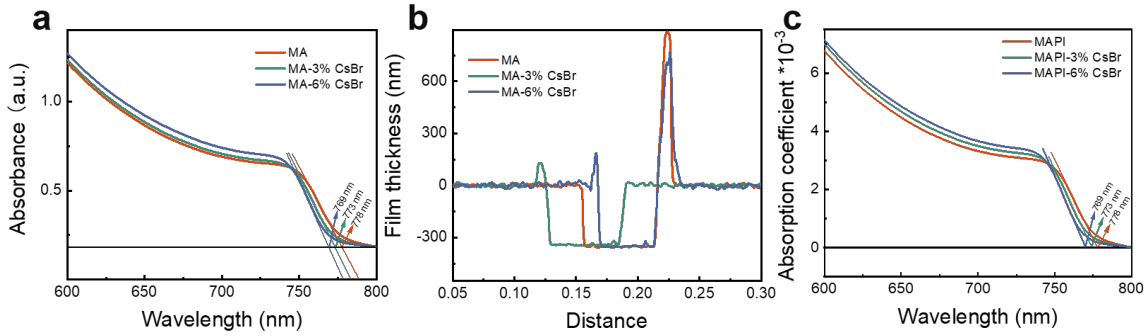

Figure 6.7: (a) UV-vis absorption spectra, (b) Thickness determination (c)UV-vis absorption coefficient of the MAPI (red), MAPI-3 % CsBr (green) and MAPI-6 % CsBr (blue) perovskite films. Adopted with permission from Ref [137]. Copyright [2022] American Chemical Society.

To evaluate the influence of the CsBr dopant on the optical properties of the perovskite materials, the absorption coefficient of the perovskite films was probed by measuring UV-vis and the film thickness, as shown in Figure 6.7a and b. The calculated absorption coefficient curves were displayed in Figure 6.7c and the corresponding calculation parameters and equations were shown in Table 6.4 with the supplementary description.

Sample	MAPI	MAPI-3 %CsBr	MAPI-6 %CsBr
Film thickness (nm)	351	346	350
On-set wavelenth (nm)	778	773	769
Band-gap (eV)	1.58	1.59	1.60

Table 6.4: Film thickness, on-set wavelength and calculated values of the band-gap for the MAPI, MAPI-3 % CsBr and MAPI-6 % CsBr films. Adopted with permission from Ref [137]. Copyright [2022] American Chemical Society.

Beer Lambert Law

$$I = I_0 \exp(-Alpha \cdot t) \tag{6.2}$$

then

$$\ln\left(\frac{I_0}{I}\right) = Alpha \cdot t \tag{6.3}$$

obtain

$$Alpha = \frac{2.303A}{t} \tag{6.4}$$

$$E_g = \frac{1240}{[incidentwavelength(nm)]} \tag{6.5}$$

$$E_g = \frac{1240}{\lambda_{in}} \tag{6.6}$$

where I_0 is incident intensity, I is the transmitted intensity, Alpha is absorption coefficient, t is the thickness of the thin film, A is the absorbance, λ is the incident wavelength (nm).

With increasing doping content of CsBr, the absorption coefficient of the films increased systematically and the absorption edge slightly blue-shifted toward the short-wavelength region. The increase in the band-gap was ascribed to two major aspects: First is the substitution of MA^+ in the host perovskite by Cs^+ with a smaller ionic radius, resulting in a decrease of lattice constant and an increase of the band-gap. [164, 166] Second, the bandgap is affected by the I/ Br atomic ratio. The introduction of Br will decrease the antibonding overlap between the np orbital of X (I or Br) and the 6s orbital of Pb, which results in a wider bandgap. [164] The enhanced absorption coefficient was beneficial for increasing the photocarrier generation rate and the increased band-gap improves the energy level alignment, respectively, thereby contributing to higher V_{OC} values.

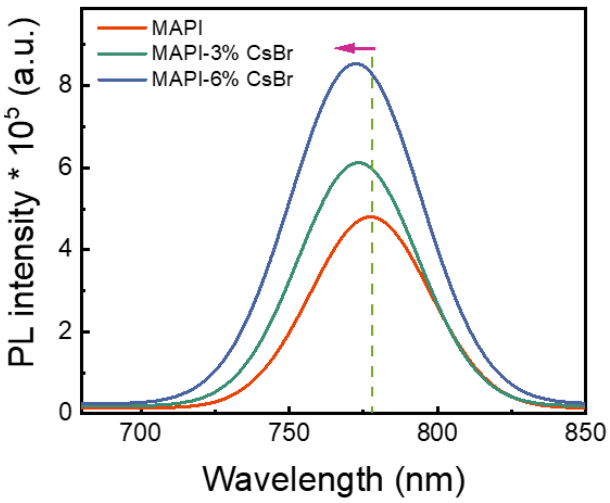

Figure 6.8: Steady-state PL spectra of MAPI (red), MAPI-3 % CsBr (green) and MAPI-6 % CsBr films (blue). Adopted with permission from Ref [137]. Copyright [2022] American Chemical Society.

In addition, the blue-shift was also observed in steady-state PL (Figure 6.8), which may be also induced by the reduction of the shallow trap density in the doped films. [155, 167] Furthermore, the steady-state PL intensities exhibited a twofold increase when increasing the CsBr-doping from 0 % to 6 %. Such enhanced PL intensity demonstrated a decrease in the rate of non-radiative charge carrier recombination, possibly due to a reduction in the grain boundaries that serve as sites of non-radiative recombination. [155] This finding was consistent with the results of the SEM and XRD measurements.

6.6 Crystal orientation of perovskite films

GIWAXS has been proven to be a versatile technique to investigate the crystal structure and the crystal orientation of polycrystalline perovskite films. [122] Herein, I applied GIWAXS measurements to study the relationship between multiple crystal orientations and the optoelectronic properties of these films. As depicted in Figure 6.9a, the corresponding 2D GIWAXS data of the MAPI film exhibited strong diffraction rings for the (110) and (220) Bragg peaks with a moderate preferential crystal orientation distribution. Upon doping MAPI with CsBr, the 2D GIWAXS patterns distinctly changed for these diffraction rings, as shown in Figures 6.9b and c, respectively.

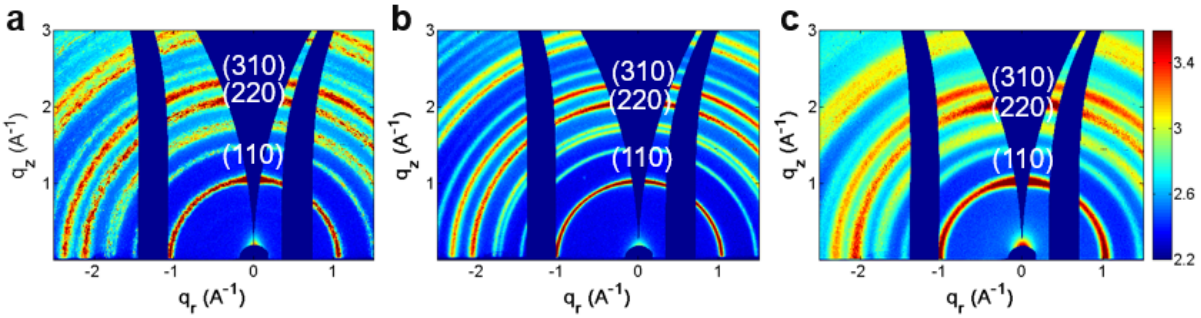

Figure 6.9: 2D GIWAXS data of (a) MAPI, (b) MAPI-3 % CsBr and (c) MAPI-6 % CsBr films with highlighted (110), (220), and (310) diffraction rings. Adopted with permission from Ref [137]. Copyright [2022] American Chemical Society.

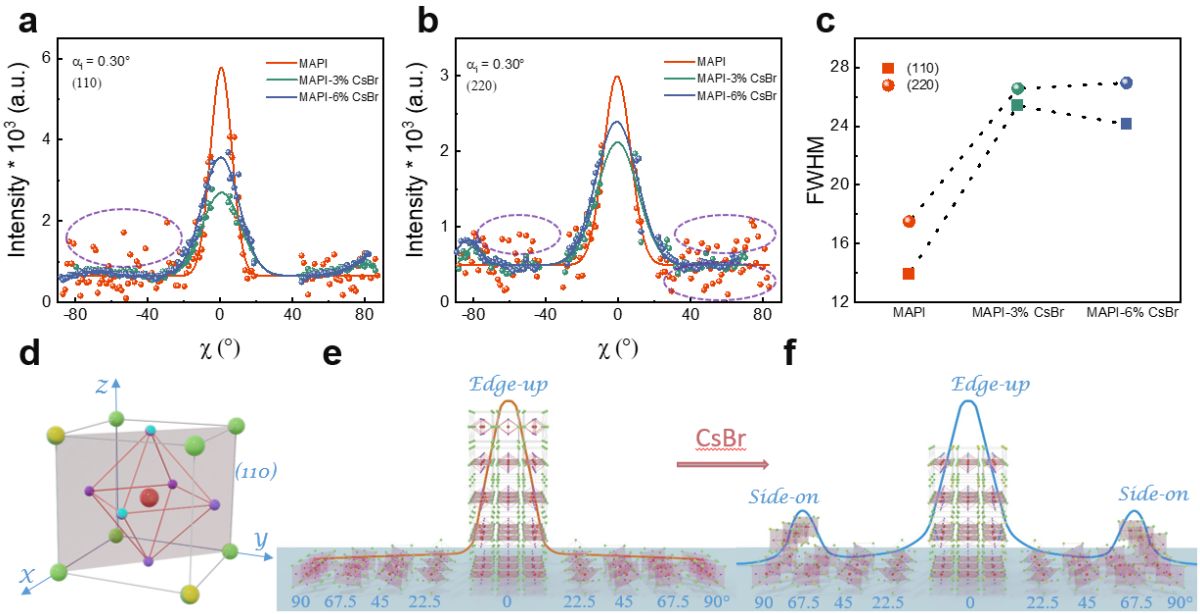

Figure 6.10: Azimuthal tube cuts of the 2D GIWAXS data in case of $\alpha_i = 0.30°$ of (a) the (002/110) Bragg peak at around q =1.00 Å^{-1} and (b) the (220) Bragg peak at around q =2.00 Å^{-1} for MAPI (red), MAPI-3 % CsBr (green) and MAPI-6 % CsBr (blue) films. The fit results based on a Gaussian function are displayed by the solid lines. (c) Corresponding azimuthal widths (FWHM) from the Gaussian fits in case of (110) Bragg peak (rectangular symbols) and (220) Bragg peak (circle symbols). (d) The crystal structure of perovskite with highlighted (110) plane. Schematic diagram of crystal stacking pattern of (e) MAPI and (f) MAPI-3 % CsBr or MAPI-6 % CsBr with the (110) plane marked in red. An edge-up orientation corresponds to the (110)-plane being parallel to the substrate. A side-on orientation corresponds to the (110)-plane being normal to the substrate. Adopted with permission from Ref [137]. Copyright [2022] American Chemical Society.

To quantitatively analyze the differences in crystal orientation distribution among these films, I performed azimuthal tube cuts along the (110) and (220) Bragg peaks of the GIWAXS data. I used a single Gaussian function to fit the respective Bragg peak orientation distribution (Figure 6.10a-c). From the perspective of mosaicity of the crystallite distribution, the MAPI perovskite film exhibited a large number of sharp intensity peaks (marked with purple dotted circles) in the range from 30° to 70° as seen from the strongly varying intensity. Each intensity peak come from a large-size crystal domain in the MAPI film contributing with a strong scattering intensity at a specific angle due to its individual orientation. In contrast, the tube cuts of CsBr-doped samples were smooth for both (110) and (220) Bragg peaks in the range from 30° to 70° and represent a wider distribution at 0°, which was caused by the concentrated distribution of the scattering peaks of the large-size crystal domain near 0°. This difference in the angular intensity distribution indicated that the doped films consisted of larger-sized crystalline domains. These domains were consequently more compact in the film and overall better aligned than the domains in the pure MAPI sample. This finding agreed well with the observations in the SEM images of the doped samples. A generally enhanced intensity at around $\chi = 0°$ in the tube cuts of all perovskite films, suggested a preferred edge-up orientation distribution irrespective of the doping. Figure 6.10d displayed the perovskite crystal structure and highlighted a typical (110) crystal plane. The "edge-up" configuration effectively described the crystal orientation preference with the (110) plane being oriented parallel to the substrate surface. In more detail, the width of the peak located at $\chi = 0°$ broadens with doping as quantified with the azimuthal full-width half-maximum (FWHM) values (Figure 6.10c). The corresponding fit results were shown in Table 6.5.

Sample	MAPI	MAPI-3 %CsBr	MAPI-6 %CsBr
(001)/(110)	13.93	25.40	24.13
(220)	17.51	26.57	26.96

Table 6.5: FWHM value of Bragg peaks extracted from fits to the azimuthal tube cuts of the 2D GIWAXS data for the MAPI, MAPI-3 % CsBr and MAPI-6 % CsBr films. Adopted with permission from Ref [137]. Copyright [2022] American Chemical Society.

Thus, the crystal orientation distribution broadens due to doping. Moreover, I also noticed that the (110) Bragg peak exhibited an orientation distribution at around 80°. In fact, this intensity was part of an intensity maximum with its center at 90° since the tube cuts contained both (110) and (100) Bragg peaks of the perovskite. The (100) Bragg peak angularly distributed at 90° indicated a side-on orientation of the crystallites. Thus, for

the case of the CsBr doped films, besides the broadened edge-on orientation also a side-on orientation was present, so the CsBr-MAPI films have a more multi-oriented crystal stacking configuration. Figures 6.10e and f sketched the stacking behaviors of the crystals in the MAPI sample and the CsBr doped MAPI samples, respectively. If all crystals grow along a particular crystallographic plane, representing one crystal orientation (such as face-up, corner-up, or side-up), then the resulting film was likely to exhibit improved charge carrier mobility and superior optoelectronic properties. Compared with the MAPI film with many randomly oriented crystalline domains, the CsBr-doped films with broadened crystal orientation distribution (edge-up and side-on) and less sharp peaks (from 30° to 70°) shown a superior charge carrier transport, as described below. Moreover, it was reported that a broadened orientation distribution of the crystallites is beneficial for both charge carrier transport and the resulting device performance. [20,156,168,169] To verify a similar effect in our case, the relevant charge carrier transport kinetics were determined with TRPL, TPC, and TPV together with the device performance.

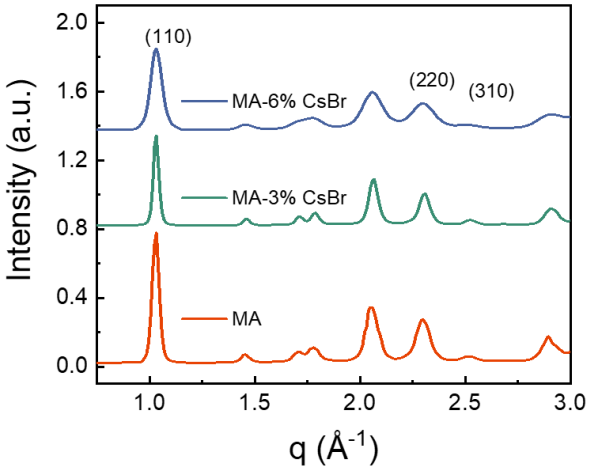

Figure 6.11: Pseudo XRD data obtained from 2D GIWAXS data integration of MAPI (red), MAPI-3 % CsBr (green) and MAPI-6 % CsBr (blue) perovskite films with labelling of the relevant Bragg peaks. Adopted with permission from Ref [137]. Copyright [2022] American Chemical Society.

Besides the tube cut analysis, also pseudo-XRD information can be gained from the 2D GIWAXS data by radial cake cut analysis (integrating over the whole Chi range), as shown in Figure 6.11. In the respective line cut data, three characteristic peaks of the tetragonal MAPI crystal structure were observed. These peaks were located at 1.00 $Å^{-1}$, 2.01 $Å^{-1}$, and 2.24 $Å^{-1}$, which matched well with the XRD measurements (Table 6.6).

Sample	MAPI	MAPI-3 %CsBr	MAPI-6 %CsBr
(001)/(110) ($Å^{-1}$)	1.029	1.031	1.032
(220) ($Å^{-1}$)	2.056	2.063	2.061
(310) ($Å^{-1}$)	2.298	2.306	2.297

Table 6.6: Bragg peak positions determined from the pseudo-XRD data obtained by integrating the 2D GIWAXS data of the MAPI, MAPI-3 % CsBr and MAPI-6 % CsBr films. Adopted with permission from Ref [137]. Copyright [2022] American Chemical Society.

6.7 Charge carrier kinetics in perovskite films and devices

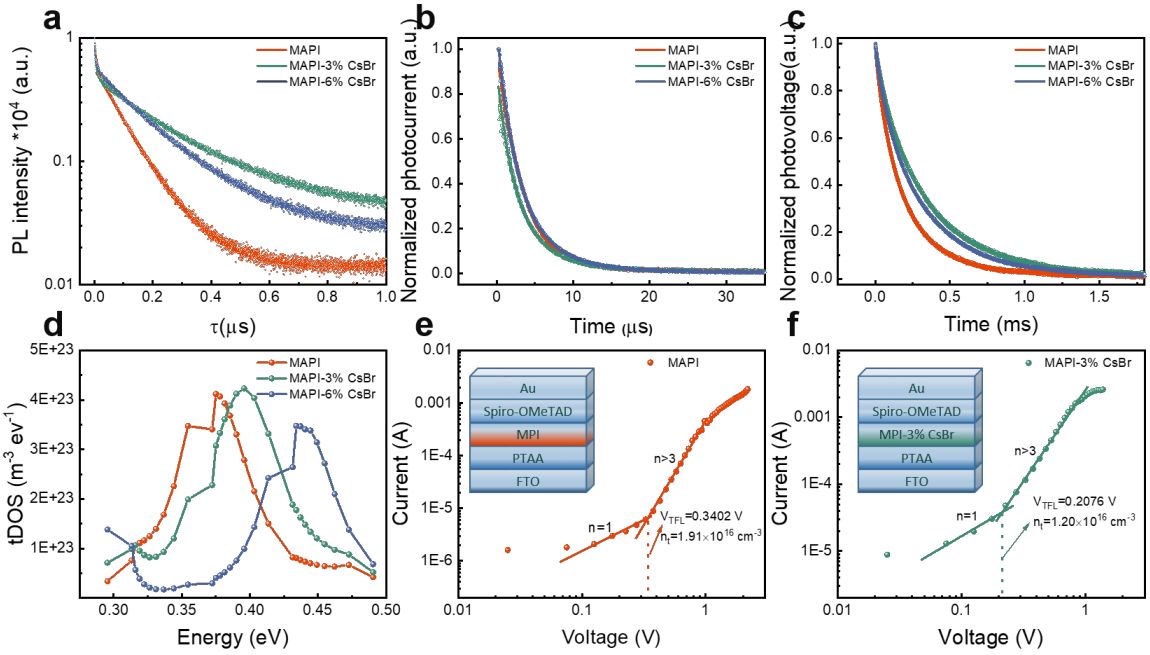

Figure 6.12: (a) TRPL decay of MAPI (red), MAPI-3 % CsBr (green) and MAPI-6 % CsBr (blue) films. The fits to the TRPL data are based on a biexponential rate law. Measurements of (b) TPC, (c) TPV and (d) tDOS deduced from C-f plots for the mixed devices. Current-voltage responses and corresponding devices structure for hole-only devices constructed from (e) MAPI and (f) MAPI-3 % CsBr devices. Adopted with permission from Ref [137]. Copyright [2022] American Chemical Society.

The effect of CsBr doping on the dynamic behavior of charge carriers was also studied in-depth. I used time-resolved TRPL to investigate the charge recombination dynamics

in the perovskite films (Figure 6.12a). The TRPL profiles were fitted by applying the bi-exponential decay model. The corresponding calculated average lifetimes and the adopted equations were displayed in Table 6.7.

Sample	MAPI	MAPI-3 % CsBr	MAPI-6 % CsBr
A_1 (%)	29.16	37.71	41.45
τ_1 (ns)	11.99	8.27	4.17
A_2 (%)	70.84	62.29	58.55
τ_2 (ns)	103.17	8244.59	180.12
$A_1 \times \tau_1$ (ns)	3.50	3.12	1.73
$A_2 \times \tau_2$ (ns)	73.09	152.35	105.46
f_1	0.05	0.02	0.02
f_2	0.95	0.98	0.98
τ_{av} amplitude weighted (ns)	77	155	107
τ_1 intensity weighted (ns)	99	240	177

Table 6.7: Average charge carrier lifetimes obtained by fits of the TRPL spectra for the MAPI, MAPI-3 % CsBr and MAPI-6 % CsBr films. Adopted with permission from Ref [137]. Copyright [2022] American Chemical Society.

With

$$f_i = \frac{A_i \tau_i}{\sum_j A_j \tau_j} \tag{6.7}$$

Intensity-weighted average lifetime

$$\tau_{ave} = \frac{a_1 \tau_1^2 + a_2 \tau_2^2}{a_1 \tau_1 + a_2 \tau_2} = f_1 \tau_1 + f_2 \tau_2 \tag{6.8}$$

Amplitude-weighted average lifetime

$$\tau_{ave} = a_1 \tau_1 + a_2 \tau_2 \tag{6.9}$$

For the CsBr-doped films, the photo-generated charge carriers decay much slower and exhibited significantly longer intensity-weighted average lifetimes (largest =240 ns in the case of 3 % CsBr) compared to the pure MAPI film (99 ns). The prolonged charge carrier lifetimes indicated that the concentration of recombination sites was significantly reduced and non-radiative carrier recombination was effectively suppressed by introducing CsBr into the perovskite. This finding agreed well with the steady-state PL measurements described above.

Furthermore, TPC and TPV were also measured to gain insight into the charge carrier-transfer kinetics and charge carrier-recombination within the materials. The measurement method was detailed in the methods section. TPC measurements were widely applied to monitor the charge carrier transport in the context of the entire device. The collected TPC data of devices based on the MAPI and CsBr-doped MAPI films were normalized and then fitted with a single-exponential function (Figure 6.12b). The extracted fit parameters were summarized in Table 6.8.

Sample	MAPI	MAPI-3 %CsBr	MAPI-6 %CsBr
τ_{ave} (μs)	3.42	3.26	3.44

Table 6.8: Fitted decay times from TPC spectra for the MAPI, MAPI-3 % CsBr and MAPI-6 % CsBr devices. Adopted with permission from Ref [137]. Copyright [2022] American Chemical Society.

The device based on MAPI-3 % CsBr film exhibited a faster charge transfer lifetime (3.26 s) compared to both the pristine MAPI film (3.42 s) and at higher CsBr doping. Thus, from the TPC data, the 3 % CsBr doping appeared to be most advantageous. The enhanced charge carrier transfer could be the result of the reduced concentration of detrimental defects and better crystal orientation distribution, resulting in more efficient charge carrier extraction and faster charge carrier transport. The finding was in good agreement with the GIWAXS results. It suggested that a broadened crystal orientation distribution (CsBr doped film: edge-up and side-on, MAPI: edge-on) was beneficial for charge carrier transport. TPV measurements correlated with electron lifetimes provided an in-depth understanding of charge carrier recombination dynamics across the entire device. The voltage-time curves and the corresponding results fitted by bi-exponential functions were shown in Figure 6.12c and Table 6.9 give the related parameters.

Sample	MAPI	MAPI-3 %CsBr	MAPI-6 %CsBr
A_1 (%)	40	19	37
τ_1 (ms)	0.09	0.10	0.10
A_2 (%)	58	78	71
τ_2 (ms)	0.27	0.37	0.36
τ_{av} (ms)	0.19	0.31	0.28

Table 6.9: Fitted decay times from TPV spectra for the MAPI, MAPI-3 % CsBr and MAPI-6 % CsBr devices. Adopted with permission from Ref [137]. Copyright [2022] American Chemical Society.

The photovoltage decay times of the devices based on MAPI, MAPI-3 % CsBr and MAPI-6 % CsBr mixed perovskite components were 0.19, 0.31, and 0.28 ms, respectively. The CsBr-doped devices were characterized by longer electron lifetimes, which results from the effective suppression of trap-assisted recombination, lower defect concentration, and superior film quality. The longest photovoltage decay time was found for 3 % CsBr, confirming also from TPV that the 3 % CsBr material was the most promising in terms of optoelectronic quality.

Thermal admittance spectroscopy (TAS) was implemented as a tool to further elucidate the trap-state distribution in the devices. I calculated the tDOS distribution from the capacitance versus frequency (*C-f*) curves measured with TAS. The trap density as a function of energy depth profiles was displayed in Figure 6.12d. Upon doping with CsBr, the device shown a relatively lower trap-state density at the energy region from 0.30 eV to 0.41 eV (shallow trap states) and a slightly higher trap-state density from 0.41 eV to 0.49 eV (deep trap states) compared to a MAPI-based device. The tDOS results demonstrated that the CsBr-doping can inhibit the generation of defects to a certain extent and has a passivation effect on shallow defects, which was in agreement with the PL characterization. The observed increase in deep trap-states can be related to lattice distortion induced by the CsBr doping. [170] Comprehensively, the introduction of CsBr played an indispensable role in the passivation of the trap-sate density, which was beneficial for improving the V_{OC} and FF values of the devices. To quantify this, the SCLC technique was used to investigate the trap density (n_{trap}) in hole-only devices (FTO/PTAA/perovskite/Spiro-OMeTAD/Au). Figure 6.12e and 6.12f displayed the current-voltage characteristics of the MAPI and MAPI-3 % CsBr devices measured under an applied bias. The curve can be divided into three regions with different n values. The Ohmic region at a low bias (n=1) can be used to calculate the conductivities of the crystals. In the trap-free regime (n=2), the charge carrier mobility of the perovskite can be estimated by Mott-Gurney's law. When n>3 (trap-filling region), the current abruptly increases at V_{TFL}. In this region, the trap density n_{trap} can be calculated using the following equation [171, 172]

$$n_t = \frac{2V_{TFL}\varepsilon\varepsilon_0}{eL^2} \tag{6.10}$$

where V_{TFL} is the trap-filled limit voltage, ε is the relative dielectric constant for MAPI (X=I, Br), ε_0 is the vacuum permittivity, e is the electron charge, L is the thickness of the perovskite crystal.

The V_{TFL} values for the MAPI and MAPI-3 % CsBr devices obtained from the *I-V* curve were 0.34 V and 0.21 V, respectively. The calculated n_{trap} of the MAPI device (1.91×10^{16} cm^{-3}) was higher than that of the MAPI-3 % CsBr device (1.20×10^{16} cm^{-3}), which can be interpreted as the defect passivation effect of CsBr.

6.8 Photovoltaic performance and stability of perovskite solar cells

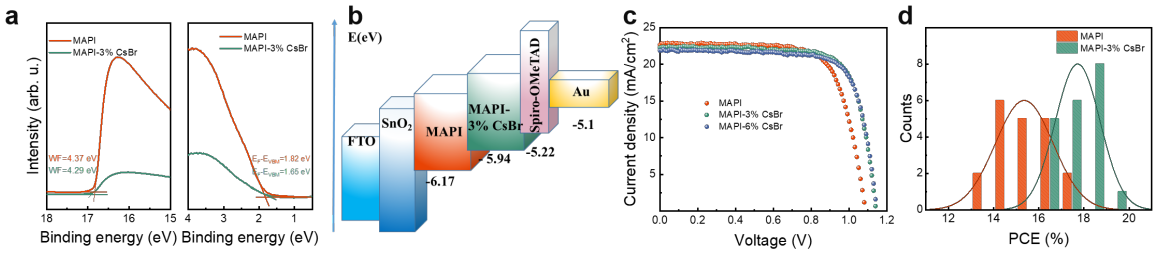

Figure 6.13: (a) UPS spectra of the MAPI and MAPI-3 % CsBr films. (b) Schematic diagram of the energy-level alignment of the devices. (c) Typical photocurrent density-voltage characteristics of devices with different CsBr content. (d) PCE distribution based on 40 solar cells for MAPI-based (red) and MAPI-3 % CsBr-based devices (green). Adopted with permission from Ref [137]. Copyright [2022] American Chemical Society.

UPS measurements were used to investigate the effect of CsBr as an additive in the perovskite precursor solution on the energy levels of the perovskite films (Figure 6.13a). The work function (WF) slightly decreased from 4.37 eV (MAPI film) to 4.29 eV in the case of the CsBr-doped MAPI. The decrease of the WF could increase the built-in potential inside the devices and was favorable to enhance the V_{OC} of PSCs. [173] Considering the WF and Fermi levels, the valence band maximum (VBM) values of the MAPI and MAPI-3 % CsBr films were calculated to be 6.17 eV and 5.94 eV, respectively. Considering the HOMO level of Spiro-OMeTAD at around 5.22 eV, the small VBM difference indicated that CsBr doping can promote a better matching of the energy levels (energy diagram was displayed in Figure 6.13b). The optimized energy band alignment between the perovskite and electron blocking layer was favorable to reducing charge carrier recombination at the interface and facilitating photoinduced charge carrier extraction and transfer. Thus, both contribute to reducing the V_{OC} loss of PSCs. This was in good agreement with the PL intensity variation and charge carrier kinetics characterization.

To explore how the crystal orientation affects the photovoltaic properties of devices, I prepared MAPI-based solar cells with different CsBr doping concentrations in the active layer. The representative J–V curves and corresponding photovoltaic parameters were displayed in Figure 6.13c and Table 6.10.

Sample	MAPI	MAPI-3 % CsBr	MAPI-6 % CsBr
V_{OC} (V)	1.09	1.14	1.15
J_{SC} (mA/cm^2)	22.88	22.20	21.84
FF	0.72	0.76	0.76
PCE (%)	17.82	19.24	18.96

Table 6.10: Summary of devices performance parameters for the champion MAPI, MAPI-3 % CsBr and MAPI-6 % CsBr devices. Adopted with permission from Ref [137]. Copyright [2022] American Chemical Society.

The best MAPI-based device exhibitd a power conversion efficiency (PCE) of 17.82 % with a relatively high short-circuit current density (J_{SC}) of 22.86 mA cm^{-2}, an V_{OC} of 1.09 V and a fill factor (FF) of 0.72. The champion device based on MAPI-3 % CsBr yielded an enhanced PCE of 19.24 %, together with a J_{SC} of 22.20 mA cm^{-2}, a V_{OC} of 1.14 V, and a high FF of 0.76. In addition, the champion device based on MAPI-6 % CsBr yielded an enhanced PCE of 18.96 %, together with a J_{SC} of 21.84 mA cm^{-2}, a V_{OC} of 1.15 V, and a high FF of 0.76. In general, many factors can affect the photovoltaic performance of the devices. In the present work, the effects of charge carrier dynamics and crystal orientation distributions on the device performance were the focus of the research. Although the charge carrier transport characteristics of the MAPI-6 % CsBr device were inferior to those of the MAPI-3 % CsBr device, its grain orientation distribution was diversified. Thus, the difference in the photovoltaic properties may be ascribed to the synergistic effect of the charge carrier dynamics and crystal orientation distribution. The PCE distribution histograms of devices based on MAPI and MAPI-3 % CsBr components (40 solar cells) was shown in Figure 6.13d. Compared to MAPI, the average PCE of MAPI-3 % CsBr-based devices was increased distinctly from 15.38 % to 17.74 %.

Figure 6.14 shown the statistical distribution results of the corresponding photovoltaic parameters of the devices based on MAPI and MAPI-3 % CsBr films. A clear improvement was observed after CsBr doping. Compared to the MAPI-based devices, the optoelectronic parameters of devices based on MAPI-3 % CsBr, particularly V_{OC} and FF were greatly enhanced. The average V_{OC} was increased from 1.05 V to 1.12 V, while the average FF was increased from 0.66 to 0.71. These results clearly illustrated that the incorporation of CsBr can effectively improve the optoelectronic properties of mixed perovskite-based photovoltaic devices. As discussed above, this remarkable improvement was attributed to the simultaneously improved charge carrier transport and suppressed charge carrier recombination.

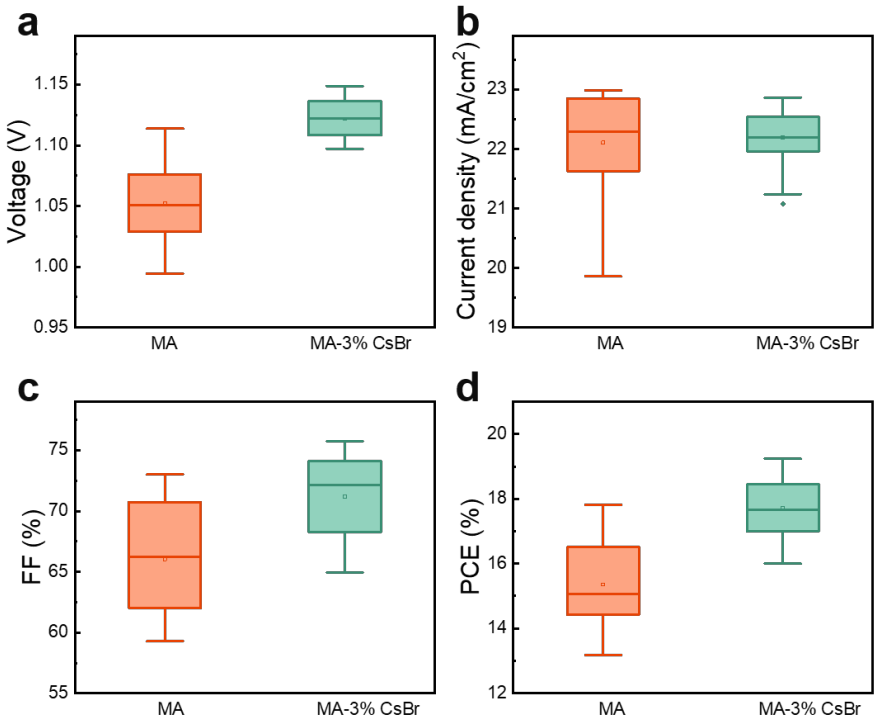

Figure 6.14: Statistical distribution of the photovoltaic parameters of the MAPI (red) and MAPI-3 % CsBr (green) PSCs based on 40 solar cells: (a) open-circuit voltage (V_{OC}), (b) short-circuit current (J_{SC}), (c) fill factor (FF) and (d) power conversion efficiency (PCE). Adopted with permission from Ref [137]. Copyright [2022] American Chemical Society.

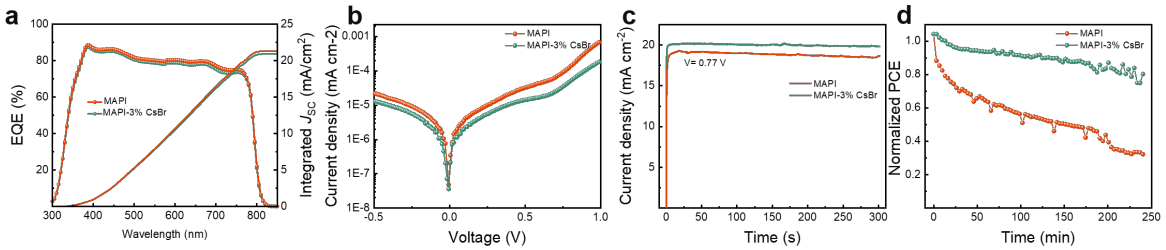

Figure 6.15: (a) EQE spectra and corresponding integrated J_{SC} curves. (b) Dark *J-V* curves. (c) photocurrent stability under constant illumination data. (d) Long-time efficiency stability under continuous illumination is measured for the MAPI and MAPI-3 % CsBr devices. Adopted with permission from Ref [137]. Copyright [2022] American Chemical Society.

External quantum efficiency (EQE) measurements were performed to crosscheck the short-circuit current density in the *J-V* measurements (Figure 6.15a). Both, the MAPI and MAPI-3 % CsBr devices were characterized by values around 90 % in the wavelength range from 300 nm to 850 nm. The integrated J_{SC} values extracted from the EQE spectra

were 21.34 mA cm^{-2} and 20.94 mA cm^{-2} for the MAPI and MAPI-3 % CsBr device, respectively, which matched well with the J_{SC} obtained from *J-V* curves, indicating good reliability of the *J-V* measurements. Moreover, dark current measurements were also performed to confirm the suppressed charge carrier recombination (Figure 6.15b). Compared with the pristine device, the MAPI-3 % CsBr device shown a lower dark current density, which suggested that the leakage paths related to charge losses were suppressed and less photocurrent was shunted. Therefore, the incorporation of CsBr can effectively inhibit charge carrier recombination and facilitate charge transfer. [174]

The device stability under ambient conditions played a crucial role in commercial applications. To examine the effect of CsBr doping on the operational stability of PSCs, I recorded the steady-state current output at the maximum power point (MPP). As seen in Figure 6.15c, the current density of the MAPI and MAPI-3 % CsBr device corresponding to its maximum power point (0.77 V) were 19.24 and 20.21 mA cm^{-2}, respectively. After illumination for 300 s, the steady-state current curve of the MAPI-3 % CsBr device remained stable without any decrease, whereas the curves of the MAPI device undergo a slight decrease. This indicated that the MAPI-3 % CsBr device has better stability than the MAPI device. I also tracked the lifetime of the MAPI and MAPI-3 % CsBr devices under an ambient atmosphere with continuous simulated AM 1.5G illumination. The *J-V* data were collected every 3.29 min and measured for 4 h. As shown in Figure 6.15d, the incorporation of CsBr can significantly improve the device's stability.

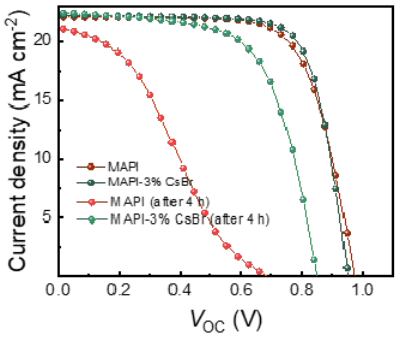

Figure 6.16: The *J-V* curves of the MAPI and MAPI-3 % CsBr devices before and after illumination for 4 h. Adopted with permission from Ref [137]. Copyright [2022] American Chemical Society.

After being exposed to continuous illumination for 4 h, the device based on MAPI-3 % CsBr preserved more than 80 % of its initial PCE and the corresponding PCE decreased from 15.76 % to 12.13 %, the corresponding *J-V* curves were shown in Figure 6.16. The PCE of the MAPI reference device presented a significant decay (from 15.10 % to 4.67 %)

and retains only 32 % of its original PCE. This implied that the incorporation of CsBr inhibited the light-activated photocurrent degradation and stabilized the perovskite light absorber to a certain degree.

6.9 Summary

In conclusion, I investigated the impacts of CsBr doping on the crystal orientation distribution and the optoelectronic behavior of the resulting perovskite films and PSCs. The incorporation of CsBr effectively promoted a self-optimization of the crystal orientation distribution, inhibited the generation of the non-radiative recombination sites, and facilitated charge carrier transfer and extraction. These CsBr doping-induced improvements in the structure and optoelectronic behavior result in an enhanced V_{OC} and superior photovoltaic efficiency of the corresponding PSCs. Best-performing devices with superior stability were observed for 3 % CsBr doping. Thus, our research on improving the perovskite crystals and reducing shallow defects to improve charge carrier dynamics provided an essential guideline for performance optimization and the further developments of PSCs.

7 Ionic liquids tailoring crystal orientation and electronic properties

This chapter is largely based on the following accepted article: "Ionic liquids tailoring crystal orientation and electronic properties for stable and high fill factor perovskite solar cells" (Zou Y et al., Nano Energy, 2023, 108449, Doi.org/10.1016/j.nanoen.2023.108449). Adopted with permission from Ref [175]. Copyright © 2023 Elsevier. In this chapter, XPS and UPS were measured by Johanna Eichhorn, TRPL was measured by Sebastian Rieger, EQE was measured by Yiting Zheng, TPV, TPC and OCVD were measured by Shuai Yuan, SEM data was measured by Shanshan Yin, GIWAXS and GISAXS were measured by Yuqin Zou, Lukas V. Spanier, and Julian E. Heger.

7.1 Preface

Metal halide PSCs have rapidly developed as highly-promising systems in the photovoltaics field, with the highest certified PCE reaching up to 25.7 %. [8, 176] However, PSCs still faced considerable challenges on the path towards commercial deployment. Current research focused strongly on further increasing the PCE towards the theoretical Shockley-Queisser (S-Q) limit, [177] enabling the fabrication of large-area devices, [178] and improving the long-term operational stability of the devices. [19, 179] The achievement of these visions was intrinsically related to overcome the inherent flaws of perovskites. Perovskite films with polycrystalline morphologies inevitably contained a large number of defects at grain boundaries and interfaces generated during crystallization. [180, 181] These defects and associated recombination pathways induced the non-radiative recombination of charge carriers, leading to a loss in the V_{OC} of the devices. [180–182] On the other hand, the perovskite components were sensitive to the external environment, particularly oxygen, light, and moisture. Long-term exposure to these influences lead

to the formation of superoxide (O_2^-) species and induces subsequent degradation of the perovskite materials. [183,184] Therefore, tailoring the crystallization process during film formation and rationally modulating the perovskite composition were powerful strategies for overcoming both, efficiency and stability limitations. Along these lines, the primary objectives can be grouped into two categories. One was to improve the film formation quality and the charge extraction efficiencies. This enabled charge carriers to be collected by the electrodes before being captured by defects, thereby lowering recombination rates. [103] The other approach was to strengthen the tolerance of perovskite materials to the external environment (moisture, light, oxygen, etc.). [183, 184] For example, constructing a protective layer on the film surface or forming stronger coordinate bonding or chemical connections between the additives and the perovskite by introducing functional ligands have been demonstrated to simultaneously stabilize the structure and passivate defects. [98, 185, 186]

Ionic liquids have been intensively investigated in energy storage devices due to their outstanding ionic conductivity and thermal stability. [187] In the PSCs field, ionic liquids have been used as additives to improve device performance and operational stability. [19, 179, 185, 188] For example, Snaith et al. used $BMPBF_4$ and $BMIMBF_4$ ionic liquids in the perovskite component to inhibit compositional segregation into impurity phases and strengthen the long-time operational stability of the devices. [19, 179] However, most previous studies have emphasized the paramount role of ionic liquids in defect passivation, energy level optimization, and phase separation suppression. Few studies have been conducted to investigate the modulation effect of ionic liquids on the crystallization kinetics during film formation from the perspective of crystal stacking mode, and in-depth explored the impact of ionic liquids on the device optoelectronic properties from the viewpoint of charge carrier kinetics (transport, extraction and recombination), as well as tracked the morphological evolution of the crystals under continuous illumination from the microscopic scale, as well as how these properties change over time to define the long-term stability.

In the present study, three different ionic liquids were selected to examine their influence on the film structure and device performance via component regulation and interface modification. By combining SEM and GISAXS/GIWAXS, I explored the role of ionic liquids in film formation, including their impacts on defining morphology and crystal orientation from a nanoscopic perspective. I found that ionic liquids promoted the development of homogenous large-grained perovskite films and enhanced the ordered arrangement of the perovskite crystals in a preferential corner-up orientation. Among the three different ionic liquids, I selected a pyrrolidinium-based ionic compound ($Pyr_{14}BF_4$) for further in-depth studies. I analyzed the kinetics of the charge carrier transport, extraction, and recombina-

tion within the perovskite films and devices utilizing a suite of transient optical and electrical measurements, revealing that the incorporation of ionic liquids increased the charge carrier mobility and extended the carrier lifetime, thereby improving charge transport and enabling efficient charge extraction. Using operando GIWAXS and GISAXS, I monitored the temporal evolution of the crystal structure, film morphology, and photovoltaic properties of the devices under operating conditions. Light-induced lattice expansion and grain fragmentation occurring in control devices under continuous illumination were prevented by the incorporation of ionic liquids. Accordingly, the $Pyr_{14}BF_4$-containing devices exhibited a high resilience under the light. Exposed to ambient conditions for up to 4368 h (6 months), the non-encapsulated $Pyr_{14}BF_4$-containing device maintained 97 % of its initial PCE value, only decreasing from 18.54 % to 18.04 %. Based on the comprehensive characterization of structural, electrical, and chemical properties of the films, I discussed the underlying mechanisms by which ionic liquids simultaneously enable high efficiency and stability perovskite devices, highlighting the importance of this strategy for further development of this class of materials.

7.2 Film morphology and crystal orientation

7.2.1 Film morphology

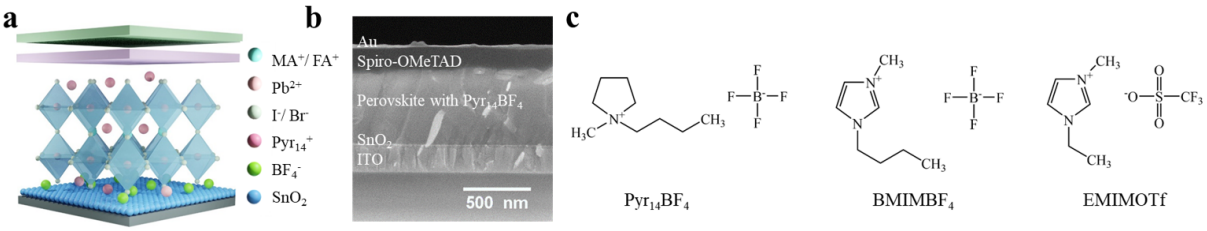

Figure 7.1: (a) Schematic of the n-i-p perovskite solar cell: ITO (grey)/SnO_2 (blue)/$(MAPbBr_3)_{0.15}(FAPbI_3)_{0.85}$/Spiro-OmeTAD (pink)/Au (green). (b) Cross-sectional SEM image of the full device stack made from $(MAPbBr_3)_{0.15}(FAPbI_3)_{0.85}$ with 1 mM $Pyr_{14}BF_4$. (c) The chemical structure of the used ionic liquids: $Pyr_{14}BF_4$, $BMIMBF_4$ and EMIMOTf. Adopted with permission from Ref [175]. Copyright © 2023 Elsevier.

Figure 7.1a depicted the planar negative-intrinsic-positive (n-i-p) device architecture, where SnO_2 and Spiro-OMeTAD were used as hole and electron blocking layers, respectively. The cross-sectional SEM image for a representative n-i-p cell based on the perovskite composition of $(MAPbBr_3)_{0.15}(FAPbI_3)_{0.85}$ containing 1 mM $Pyr_{14}BF_4$ (with

respect to one milliliter of solution) (Figure 7.1b) clearly shown the device configuration with different layers of ITO, compact SnO_2, perovskite, spiro-OMeTAD and Au. I screened out three promising and widely utilized ionic liquids as additives, 1-butyl-1-methylpyrrolidinium tetrafluoroborate ($Pyr_{14}BF_4$), 1-butyl-3-methylimidazolium tetrafluoroborate ($BMIMBF_4$) and 1-ethyl-3-methylimidazolium trifluoromethanesulfonate (EMIMOTf), to investigate their impacts on the morphology and crystal orientation during perovskite film formation.

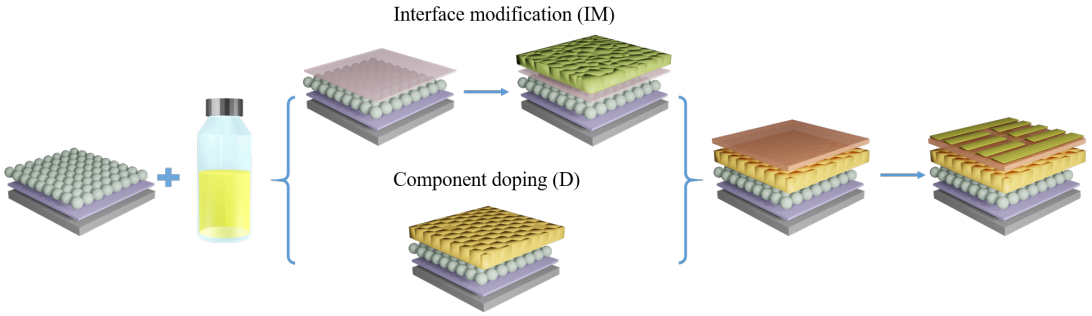

Figure 7.2: Schematic diagram of the perovskite solar cells fabrication using the interface modification (IM) or component doping (D) process. Adopted with permission from Ref [175]. Copyright © 2023 Elsevier.

The chemical structures of these three ionic liquids were depicted in Figure 7.1c. The schematic diagram of the corresponding film and device preparation process was shown in Figure 7.2. In the following, the pristine $(MAPbBr_3)_{0.15}$ $(FAPbI_3)_{0.85}$ perovskite component was denoted as control, the SnO_2 surface modified with ionic liquid solution was denoted as IM- (interface modification), and the perovskite component incorporating ionic liquids within its bulk was denoted as D- (component doping).

Figure 7.3a-d shown the SEM images of the D-series perovskite films. In general, the ionic liquid-doped perovskite films shown a better coverage and a higher uniformity compared with the control film. Statistical analysis of the grain sizes revealed that the ionic liquid-doped perovskite films exhibited a larger average grain size (Figure 7.3e-h) compared with the reference (217 nm for control, 320 nm for D-$Pyr_{14}BF_4$, 319 nm for D-$BMIMBF_4$, 272 nm for D-EMIMOTf). The formation of the perovskite thin film was influenced by nucleation and crystal growth according to the LaMer model. [178] For conventional spin-coated perovskite films, a low density of heterogeneous nuclei with a fast growth rate promotes the growth of large dendritic perovskite structures, impairing the ultimate device performance. [189] In order to form high-quality perovskite films with higher surface coverage and fewer defects, the generation of a large number of nuclei (fast nucleation) before the triggering of the crystallization process (slow crystal growth) is

crucial. Analysis of SEM images suggested that the homogenous and enlarged grains observed in the ionic liquid-containing perovskite films most likely originated from the incorporation of the non-volatile ionic liquid, which promoted the formation of uniformly distributed crystal nuclei on the substrate, while also maintaining the liquid environment for subsequent crystallization by retarding the solvent evaporation. [190] These synergistic effects of fast nucleation and slow crystallization result in the initial generation of a large number of perovskite crystal nuclei that subsequently grow. When the grains intersected, the crystal growth stagnated and a uniform and full-coverage perovskite film formed.

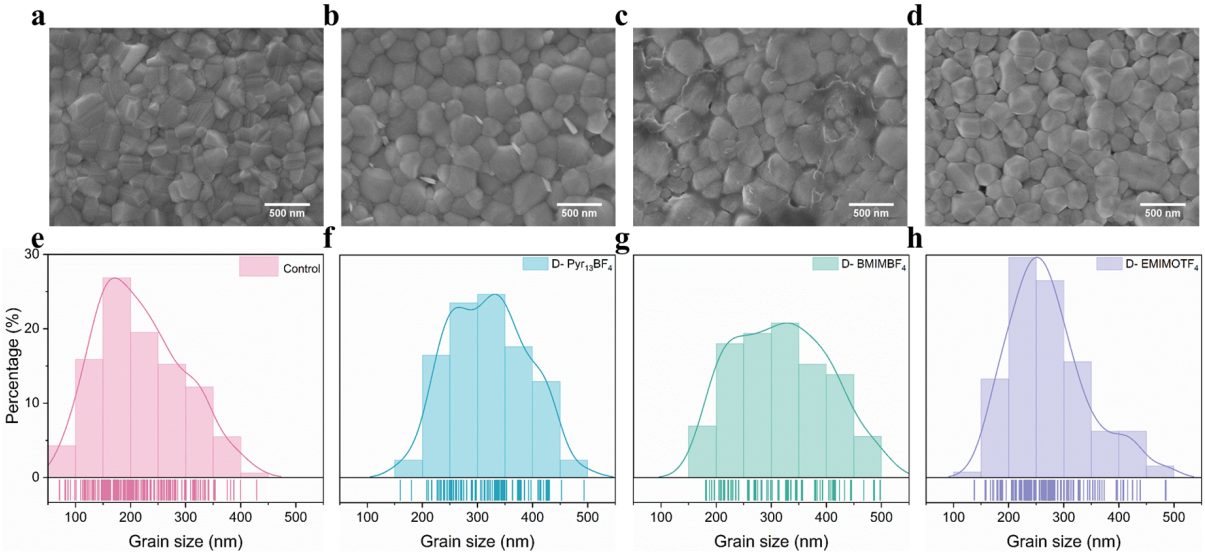

Figure 7.3: (a-d) Top-view SEM images and (e-h) statistical grain size distribution of perovskite films treated (a, e) without and with ionic liquids comprising (b, f) $Pyr1_4BF_4$, (c, g) $BMIMBF_4$ and (d, h) EMIMOTf. Adopted with permission from Ref [175]. Copyright © 2023 Elsevier.

Figure 7.4 depicted SEM images and calculated grain size distributions of perovskite films doped with different concentration of $Pyr_{14}BF_4$. The observed homogenous and large-grained perovskite films from all doping ratios further confirmed the tailoring effect of ionic liquids on the nucleation and subsequent crystal growth processes. I noted that such large-grained and homogeneous perovskite films are expected to promote long-term device stability due to the inverse correlation between superoxide generation yield (and subsequently degradation rate) and the perovskite grain size reported in the literature. [183] In the case of the ionic liquid-treated films composed of large perovskite crystallites, it exhibited longer O_2 diffusion paths to the grain interiors as well as lower photo-induced superoxide formation rates, resulting in higher device stability, as discussed in further detail below. [183]

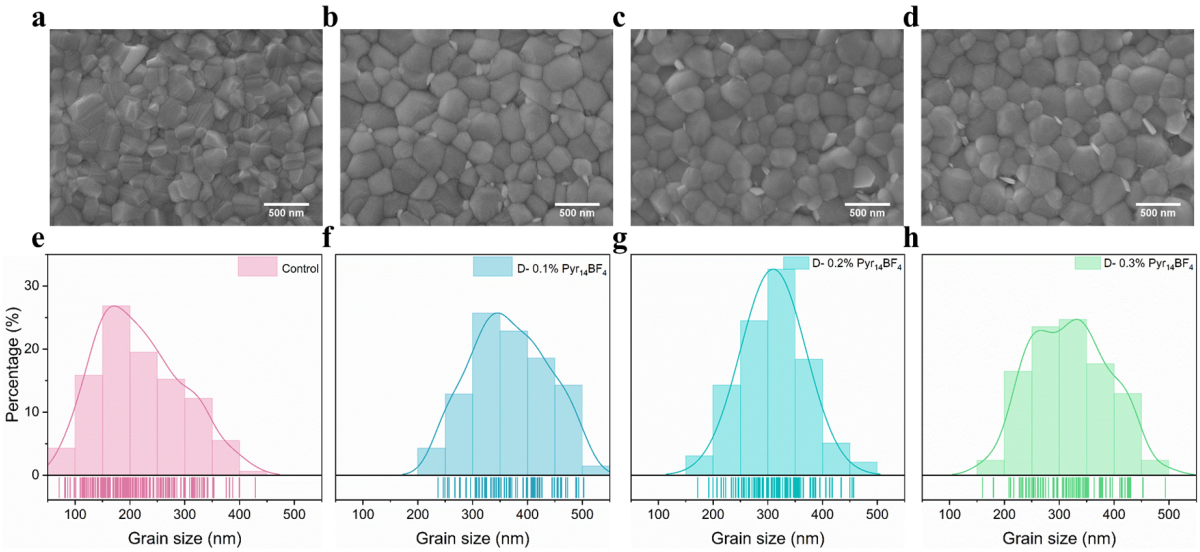

Figure 7.4: Top-view SEM images and grain size statistical distribution of perovskite films doped with different $Pyr_{14}BF_4$ concentration: (a,b) Control, (c,d) 1 mM, (e,f) 2 mM and (g,h) 3 mM. Adopted with permission from Ref [175]. Copyright © 2023 Elsevier.

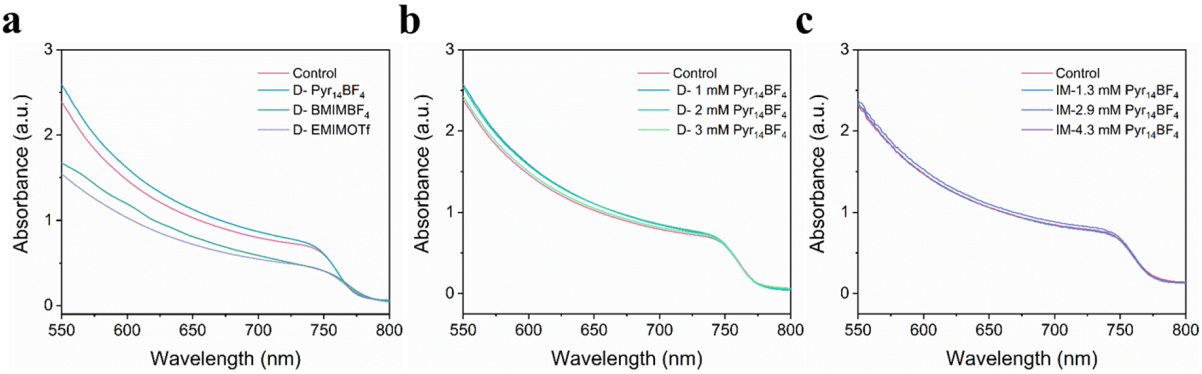

Figure 7.5: UV-vis absorption spectra of (a) perovskite films doped with different ionic liquid additives, (b) perovskite films doped with different $Pyr_{14}BF_4$ concentration and (c) perovskite films in which the SnO_2 films are modified with different $Pyr_{14}BF_4$ concentrations. Adopted with permission from Ref [175]. Copyright © 2023 Elsevier.

UV-vis absorption spectroscopy was used to examine the light-harvesting ability of the different perovskite films, as shown in Figure 7.5a-c, as well as potential changes of electronic structure induced by ionic liquid incorporation. Importantly, UV-vis revealed no significant change of the position of the absorption edge, indicating that the incorporation of ionic liquids did not have a substantial effect on the optical band gap of the perovskite films. The slightly enhanced light absorption observed in D-$Pyr_{14}BF_4$films originated

from the high crystallinity of these films, which contributed to a higher photocurrent of the related devices (Figure 7.5b), as described below. [185]

In addition, XRD patterns indicated a slight shift towards high angles in the characteristic peaks of D-$Pyr_{14}BF_4$ perovskite films with respect to the control film, while there are no discernible differences for the case of IM-$Pyr_{14}BF_4$films, as shown in Figure 7.6. Such a shift can originate from the selective interaction of the ionic liquid and precursor ions.

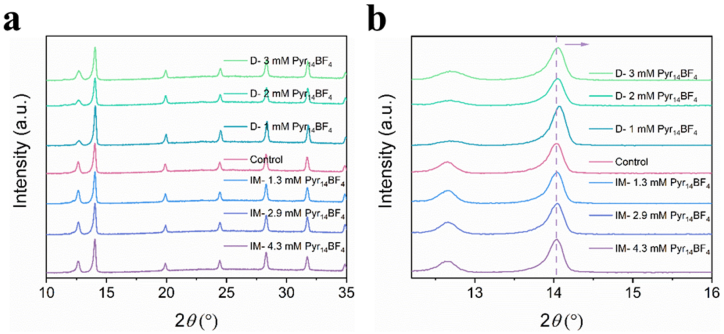

Figure 7.6: (a) XRD spectra of perovskite thin films with $Pyr_{14}BF_4$ additive. (b) Zoom-in of the XRD spectra of the perovskite (110) peaks shown in (a) to better show the peak shift and shape. Adopted with permission from Ref [175]. Copyright © 2023 Elsevier.

7.2.2 Crystal orientation

To gain deeper insights into the crystallization process, I performed GIWAXS, in which the crystal lattice spacing is associated with the position of the Bragg peaks (scattering vector q) and the crystal orientation is derived from the azimuthal intensity distribution of the Bragg peaks. [124] Figure 7.7a-d shown the two-dimensional (2D) GIWAXS data of the perovskite films doped with different ionic liquids. Azimuthal tube cuts along the (110) and (220) Bragg peaks of the GIWAXS data, fitted with Gaussian functions, were performed to quantitatively analyze the crystal orientation distribution (Figure 7.7e and f). The large-size crystal domains in the perovskite films contributed a strong scattering intensity at a particular angle due to their individual orientations. [191] The intensity distribution in the control film was broadly distributed over all angles, suggesting that the crystal orientation was nearly randomly distributed. However, in the case of the ionic liquid-doped films, the scattering signal of large-size crystal domains contributed pronounced intensity at $\chi = 35°$ and 65°, indicating preferential crystal growth with a corner-up orientation.

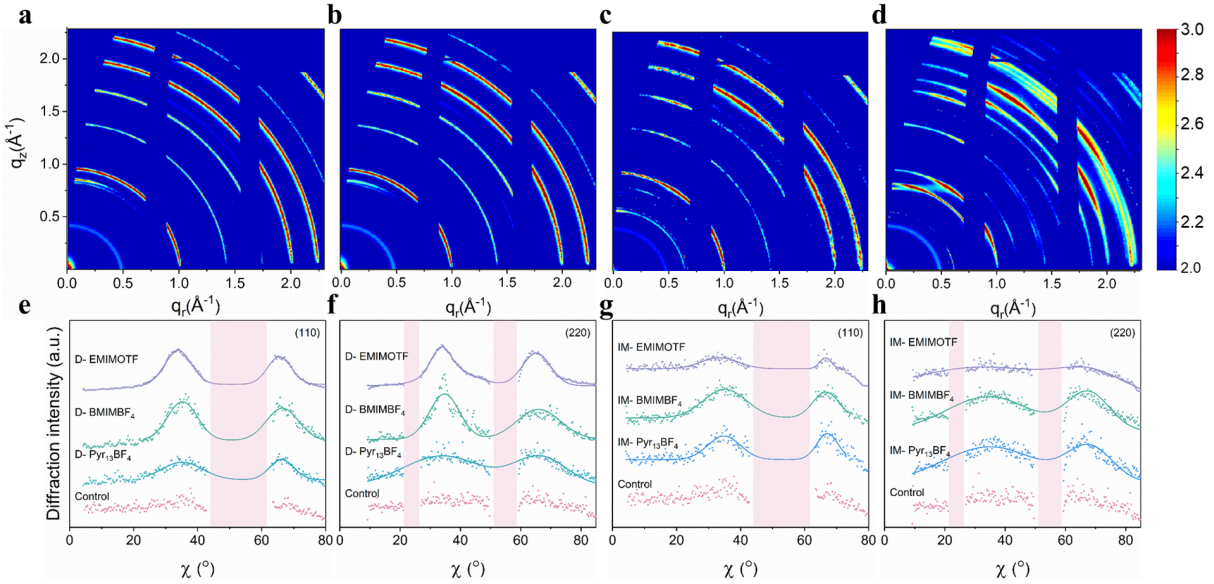

Figure 7.7: 2D GIWAXS data of perovskite thin films for (a) the control, (b) D-$Pyr_{14}BF_4$, (c) D-$BMIMBF_4$ and (d) D-EMIMOTf. Azimuthal tube cuts of the 2D GIWAXS data measured at α_i = 0.60° of the (e) (002/110) and (f) (220) Bragg peak at around q =1.00 Å^{-1} for D-perovskite films doped with different ionic liquids, (g) (002/110) and (h) (220) Bragg peak for IM-perovskite films based on SnO_2 surface modified with different ionic liquids. Adopted with permission from Ref [175]. Copyright © 2023 Elsevier.

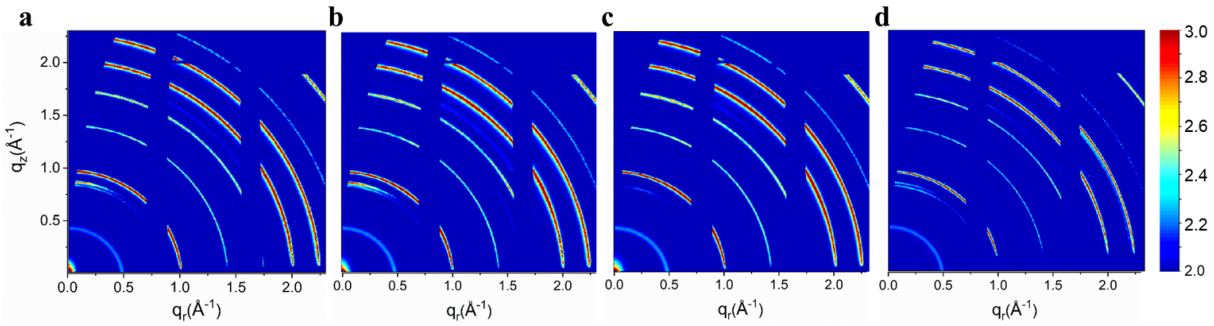

Figure 7.8: 2D GIWAXS data of IM-perovskite films in which the SnO_2 films are modified with different ionic-liquids: (a) Control, (b) IM-$Pyr_{14}BF_4$, (c) IM-$BMIMBF_4$ and (d) IM-EMIMOTf. Adopted with permission from Ref [175]. Copyright © 2023 Elsevier.

In the case of the IM-series perovskite films, the (110) and (220) Bragg peaks also exhibited a preferential crystal orientation at 35° and 65° (Figure 7.7g and h). The corresponding 2D GIWAXS data of IM-series perovskite films was shown is Figure 7.8.

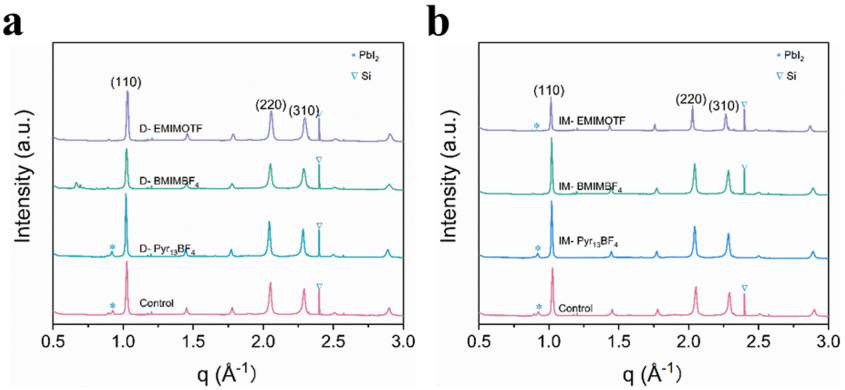

Figure 7.9: Pseudo-XRD data extracted from the 2D GIWAXS data by radial cake cut analysis for (a) D-perovskite and (b) IM-perovskite films. Adopted with permission from Ref [175]. Copyright © 2023 Elsevier.

In the pseudo-XRD data obtained from the 2D GIWAXS data via radial cake cut analysis (Figure 7.9a), I observed that the peak intensity of a secondary lead iodide (PbI_2) phase (marked with a blue asterisk) in the D-series perovskite films was significantly weakened and even fades away. Such a decrease in PbI_2 content could result from hydrogen bonds formed between the high-boiling point ionic liquid and residual solvent molecules during the annealing of the perovskite films. Such bond formation delayed the rapid evaporation of the residual solvent when the film transformed from a colloidal into a solid-state film, thereby lowering the loss of volatile MAI and thus hindering the precipitation of PbI_2. For the case of the IM-series perovskite films, a weakening PbI_2 peak was also observed in the pseudo-XRD data for two of the ionic liquid-containing perovskite films (Figure 7.9b). These findings implied that the pre-treatment of the SnO_2 film surface with ionic liquids also promoted an isotropic growth of the perovskite crystals with preferential orientation.

In summary, based on the crystal orientation distribution, the utilization of ionic liquids for both bulk doping and SnO_2 interface modification facilitated the transition of the thin film texture from randomly oriented to preferentially corner-up oriented. Importantly, perovskite films with such a preferred corner-up crystal orientation have been demonstrated to exhibit higher out-of-plane charge carrier mobility, thereby significantly promoting photo-excited carrier transport and efficient charge extraction, [20, 137] as will be discussed in the recombination kinetics section below. From the viewpoint of crystal structure, the introduction of ionic liquids into the active layer effectively inhibited the segregation of the PbI_2 phase from the perovskite component during the film formation process.

7.3 Photovoltaic performance

Among the three different ionic liquids studied regarding the perovskite crystal growth, $Pyr_{14}BF_4$ was selected as the primary additive to investigate its role in photovoltaic performance, charge carrier dynamics and long-term stability of PSC devices for its high electrical conductivity, high charge carrier mobility and superior optical transparency. [187] As a starting point, the correlation between ionic liquid concentration and photovoltaic performance was explored from the perspectives of SnO_2 interface modification and perovskite component doping (Figure 7.2).

The $Pyr_{14}BF_4$ concentration was adjusted from 0.0 to 4.3 mM for the interface modification series (IM-series) and from 0.0 to 3 mM for the doping concentration series (D-series). The distribution of photovoltaic parameters and the typical current density-voltage (J-V) characteristics of the champion devices for each of the interface modifications with 4.3, 2.9 and 1.4 mM $Pyr_{14}BF_4$ (IM-4.3, IM-2.9, IM-1.4), control and for the doping series with 1, 2, and 3 mM $Pyr_{14}BF_4$ (D-1, D-2 and D-3) were depicted in Figure 7.10, with the corresponding statistical results listed in Table 7.1. For the D-series, a low $Pyr_{14}BF_4$ concentration resulted in a positive influence on the photovoltaic performance. However, at higher $Pyr_{14}BF_4$ concentrations, the device performance was reduced.

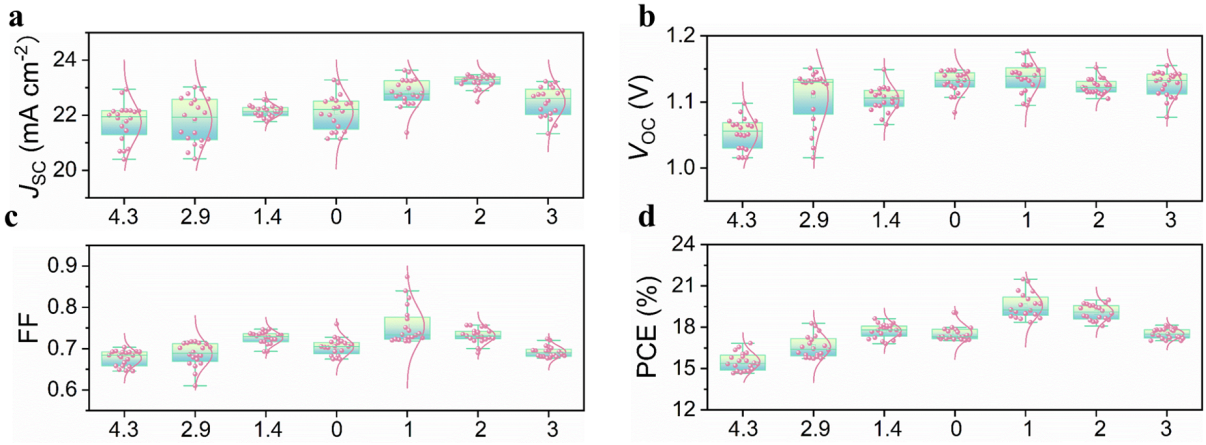

Figure 7.10: Statistics of device parameters for solar cells based on ITO/SnO_2/perovskite/Spiro-OmeTAD/Au structure, from left to right are spin-coated different $Pyr_{14}BF_4$ concentrations dissolved in methanol ranging from 4.3 to 1.4 mM on the SnO_2 surface, control, perovskite precursors doped with $Pyr_{14}BF_4$ concentration ranging from 0 to 3 mM. (a) J_{SC}, (b) V_{OC}, (c) FF, (d) PCE were determined from the J–V scan curves of 20 cells for each condition. Adopted with permission from Ref [175]. Copyright © 2023 Elsevier.

Device	J_{SC} (mA cm^{-2})	V_{OC} (V)	FF	PCE (%)
IM-4.3 mM $Pyr_{14}BF_4$				
Average	21.75 ± 0.69	1.05 ± 0.02	0.68 ± 0.02	15.50 ± 0.64
Champion	22.12	1.07	0.70	16.57
IM-2.9 mM $Pyr_{14}BF_4$				
Average	21.81 ± 0.82	1.11 ± 0.04	0.69 ± 0.03	16.59 ± 0.81
Champion	23.02	1.13	0.70	18.28
IM-1.4 mM $Pyr_{14}BF_4$				
Average	22.13 ± 0.22	1.10 ± 0.02	0.73 ± 0.01	17.74 ± 0.50
Champion	22.35	1.12	0.75	18.63
Control devices				
Average	22.11 ± 0.63	1.13 ± 0.02	0.70 ± 0.02	17.59 ± 0.59
Champion	23.18	1.15	0.72	19.06
D-1 mM $Pyr_{14}BF_4$				
Average	22.88 ± 0.51	1.14 ± 0.02	0.75 ± 0.04	19.49 ± 0.80
Champion	23.27	1.14	0.81	21.34
D-2 mM $Pyr_{14}BF_4$				
Average	23.22 ± 0.25	1.12 ± 0.01	0.73 ± 0.02	19.09 ± 0.56
Champion	23.44	1.13	0.75	20
D-3 mM $Pyr_{14}BF_4$				
Average	22.48 ± 0.55	1.13 ± 0.02	0.69 ± 0.01	17.53 ± 0.36
Champion	23.39	1.13	0.69	18.22

Table 7.1: Summarized photovoltaic parameters of solar cells based on glass/SnO_2 modified with $Pyr_{14}BF_4$/perovskite/spiro-OMeTAD/Au structure, ITO/SnO_2/perovskite /spiro-OMeTAD/Au structure, and ITO/SnO_2/perovskite doped with $Pyr_{14}BF_4$/spiro-OMeTAD/Au structure. Adopted with permission from Ref [175]. Copyright © 2023 Elsevier.

Figure 7.11a depicted the J-V characteristics of the champion PSCs. For the champion device comprising 1 mM $Pyr_{14}BF_4$, I measured an V_{OC} of 1.14 V, a J_{SC} of 23.27 mA cm^{-2} and a high FF of 0.81 yielding a PCE of 21.34 %. The champion control device exhibited a PCE of 19.06 %, due to a lower FF of 0.72. The considerably increased FF achieved in $Pyr_{14}BF_4$-containing devices was attributed to the following aspects: i) The tailoring and repairing effects of the ionic liquid during nucleation and crystal growth, resulting in larger grains and improved crystallinity with fewer grain boundaries and fewer defects. ii) The crystal stacking transfer from isotropic to preferential corner-up orientation, exhibiting higher charge carrier mobility and leading to higher FF values. iii) Better energy level

alignment between the perovskite layer and charge blocking layers and superior charge carrier transport and extraction capabilities, which helps to avoid introducing energy barriers to charge transport and improves the charge carrier extraction efficiency, which will be demonstrated by the following UPS, EIS, TPC and TPV sections. iv) Lower trap density and lower charge carrier recombination rate in the perovskite film, which will be discussed in SCLC and TRPL section.

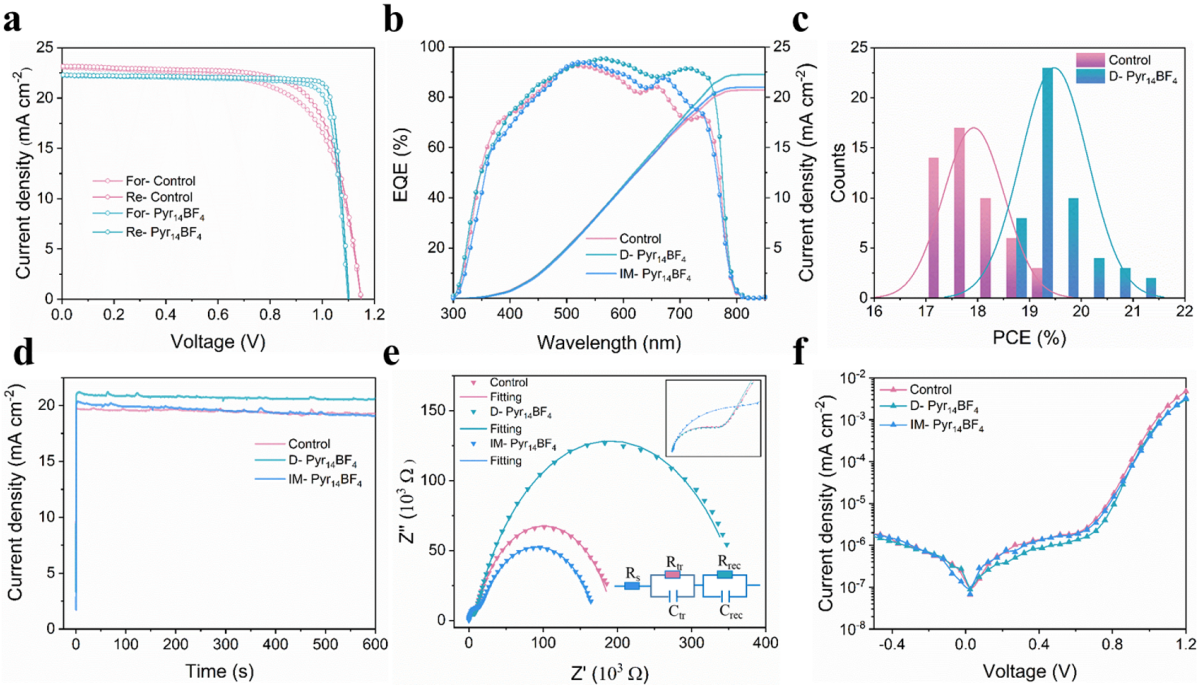

Figure 7.11: Current density-voltage (*J-V*) curves of the best performing devices measured from forward to reverse scan under simulated AM 1.5 sunlight. (b) EQE spectra and integrated J_{SC} of the fabricated perovskite solar cells. (c) PCE distribution histograms based on 50 cells per type. (d) Steady-state photocurrent density measured at the maximum power point. (e) Nyquist plots of EIS with the equivalent circuit. (f) Dark *J-V* curves. Adopted with permission from Ref [175]. Copyright © 2023 Elsevier.

Figure 7.11b displayed the external quantum efficiency (EQE) of devices and the integrated results of the EQE curves. The enhanced response in the wavelength ranges from 450 to 750 nm observed in $Pyr_{14}BF_4$-containing devices suggested that the incorporation of $Pyr_{14}BF_4$ was favorable for promoting photo-generated charge carrier transport and efficient extraction by the charge blocking layer. Considering the enhanced EQE for longer wavelengths, this effect is especially pronounced for charge carriers generated deep within the absorber layer. [192] The J_{SC} integrated over the solar spectrum was 20.71 mA cm^{-2} for the control, 22.25 mA cm^{-2} for the D-$Pyr_{14}BF_4$ and 21.01 mA cm^{-2} for the IM-$Pyr_{14}BF_4$ device, respectively, in excellent agreement with the J_{SC} values derived

from J-V curves. Figure 7.11c displayed the histograms of the PCE distributions of the control and the $Pyr_{14}BF_4$-containing devices based on 50 solar cells prepared for each condition. Upon the incorporation of 1 mM $Pyr_{14}BF_4$, the average PCE was improved from 17.91 % to 19.52 % with high reproducibility. As an initial assessment of stability, steady-state output current densities were recorded as a function of time at the maximum power point (Figure 7.11d), with the current density of the control, D-$Pyr_{14}BF_4$ and IM-$Pyr_{14}BF_4$ devices stabilizing at around 20 mA cm^{-2}, 21 mA cm^{-2} and 20 mA cm^{-2}, respectively. While the D-$Pyr_{14}BF_4$ device maintained high stability, both the control and the interface-modified devices were characterized by slight decreases of photocurrent during illumination for more than 600 s.

Sample	R_s (Ω)	R_{tr}	R_{rec} (Ω)
Control	54.16	7736	188090
D-$Pyr_{14}BF_4$	256.68	7376	365490
IM-$Pyr_{14}BF_4$	101.60	10328	167070

Table 7.2: EIS parameters for the PSCs based on three types of devices. Adopted with permission from Ref [175]. Copyright © 2023 Elsevier.

EIS measurements on the whole cells were performed to provide additional insights into the interfacial charge transport, recombination and series resistance. The Nyquist plots depicted in Figure 7.11e were analyzed with an equivalent circuit model (see inset of Figure 7.11e) composed of series resistance (R_s) and two elements for the transfer resistance (R_{tr}) and recombination resistance (R_{rec}), each of which are in parallel with capacitors (C_{tr} and C_{rec}). The Rs primarily reflects the electrical contacts, wires and sheet resistance of the electrodes, the R_{tr} is ascribed to the high-frequency element and reflects the charge extraction/transfer properties at the HBL-perovskite and/or perovskite-EBL interface, and the R_{rec} is assigned to the low-frequency region and is related to charge carrier recombination arising from defects within the active layer. [111, 193] The R_{tr} and R_{rec} were determined to be 7.74 kΩ and 188 kΩ for the control, 7.38 kΩ and 365 kΩ for D-$Pyr_{14}BF_4$, and 10.33 kΩ and 167 kΩ for IM-$Pyr_{14}BF_4$ (Table 7.2), respectively. For the case of the doped device, the smaller R_{tr} and larger R_{rec} values reflected more efficient charge carrier extraction/transport at the interface and considerably suppressed photo-excited charge carrier recombination. The findings highlighted the paramount role of ionic liquids in boosting charge carrier injection and minimizing transfer resistances, leading to a high FF. [111, 177] Furthermore, the lower dark current density of the $Pyr_{14}BF_4$–containing device suggested reduced shunting, which would contribute to improved J_{SC} and V_{OC} observed for PSCs constructed from this material (Figure 7.11f). [171]

7.4 Surface electronic properties of films

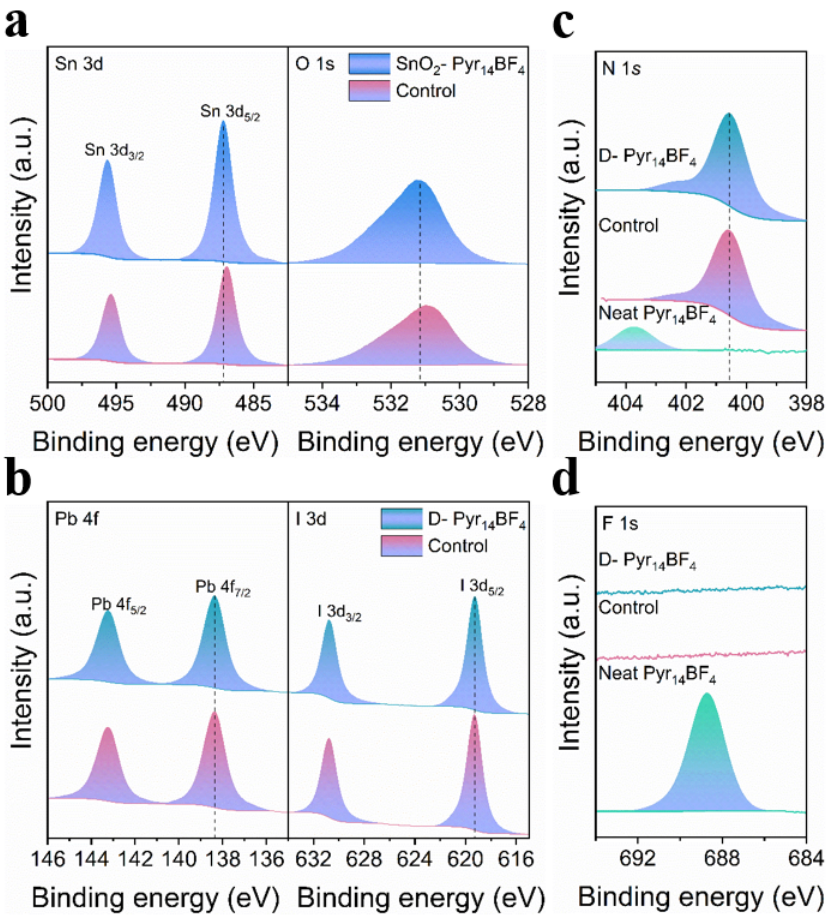

Figure 7.12: (a) Sn 3d and O 1s XPS spectra of SnO_2 and SnO_2-$Pyr_{14}BF_4$ films. (b) Pb 4f and I 3d XPS spectra of control and D-$Pyr_{14}BF_4$ perovskite films. (c) N 1s and (d) F 1s XPS spectra of neat $Pyr_{14}BF_4$, perovskite and D-$Pyr_{14}BF_4$ perovskite films. Adopted with permission from Ref [175]. Copyright © 2023 Elsevier.

Sample	N 1s (eV)	F 1s (eV)	Sn $3d_{5/2}$ (eV)	O 1s (eV)	pb 4f $_{7/2}$ (eV)	I $3d_{5/2}$ (eV)
$Pyr_{14}BF_4$	403.7	687.4	No	No	No	No
SnO_2	No	No	487.0	530.9	No	No
SnO_2-$Pyr_{14}BF_4$	402.7	686.5	487.2	531.2	No	No
Perovskite	400.5	No	No	No	138.4	619.3
D-$Pyr_{14}BF_4$	400.5	No	No	No	138.4	619.3

Table 7.3: Binding energies of elements obtained from X-ray photoelectron spectroscopy (XPS). Adopted with permission from Ref [175]. Copyright © 2023 Elsevier.

XPS and UPS measurements were carried out to investigate the influence of $Pyr_{14}BF_4$ on the surface electronic properties of SnO_2 and the perovskite layer (Figure 7.12). The binding energies of all main components were listed in Table 7.3. For the XPS spectra of the SnO_2 film treated with $Pyr_{14}BF_4$ (abbreviated as SnO_2-$Pyr_{14}BF_4$), I noted a peak shift towards higher binding energies in the Sn 3d and O 1s spectrum relative to pure SnO_2 (Figure 7.12a). In detail, the Sn $3d_{3/2}$ (487.0 eV) and Sn $3d_{5/2}$ (495.4 eV) peaks of SnO_2 film were shifted to 487.2 eV and 495.6 eV, respectively, and the main peak of O 1s was shifted from 530.9 eV to 531.2 eV after $Pyr_{14}BF_4$ treatment. The observed shifts could arise from the chemical interaction established between Sn and more electronegative F (F: 3.98, O: 3.44), increasing the coordination number surrounding Sn atoms. [185, 194, 195] For the pristine and D-$Pyr_{14}BF_4$ perovskite films, no binding energy shift was observed for the Pb $4f_{7/2}$ and I $3d_{5/2}$ spectra (Figure 7.12b), as well as for the N 1s spectrum after $Pyr_{14}BF_4$ incorporation (Figure 7.12c). Additionally, no fluorine signal was detected in the $Pyr_{14}BF_4$-containing perovskite film (Figure 7.12d). [19] Previous studies pointed out that the BF_4^- utilized for perovskite component doping was predominantly distributed at the bottom of the perovskite layer and was thus challenging to detect on the top surface. [19, 185, 196] Therefore, it was difficult to determine the chemical interaction between Pb, I and BF_4^- in terms of the electron density variation of Pb and I.

The UPS spectra of SnO_2 and SnO_2-$Pyr_{14}BF_4$ were depicted in Figure 7.13a and the energy level parameters were listed in Table 7.4. From the secondary electron cutoff, I observed a 600 meV decrease in the work function (WF) of SnO_2, from 4.5 eV to 3.9 eV, after $Pyr_{14}BF_4$ modification. The energetic positions of the valence band maxima below the Fermi level (E_{VBM}), obtained from valence band spectroscopy, were 3.3 eV for pure SnO_2 and 3.4 eV for SnO_2-$Pyr_{14}BF_4$ films. The electron affinity (energetic position of the conduction band minimum below the vacuum level) was calculated to be 4.2 eV (3.7 eV) for SnO_2 (SnO_2-$Pyr_{14}BF_4$). The electronic properties of control and $Pyr_{14}BF_4$–containing perovskite films were also determined by WF and valence band maximum (VBM) measurements using UPS and UV-vis (Figure 7.13b and Figure 7.14). The WF significantly decreased from 4.4 eV to 4.0 eV for the case of the $Pyr_{14}BF_4$–containing perovskite film, indicating an upward shift of 400 meV. Relative to the vacuum level, the VBM and CBM were determined to lie at -5.7 eV and -4.1 eV for the control, and at -5.2 eV and -3.6 eV for the D-$Pyr_{14}BF_4$ film, as determined by combining photoemission results with optical bandgaps derived from Tauc plots. The corresponding changes of energy alignment at heterojunctions between the perovskite films and charge transport layers was schematically summarized in Figure 7.13c. The maximum achievable photovoltage of PSCs was determined by the quasi-Fermi-level splitting of electrons and holes, $V_{OC} = \frac{1}{q}(E_{fn} - F_{fp})$. [63, 185]The shallower valence band position in D-$Pyr_{14}BF_4$ per-

ovskite reduced the potential barrier to block the transfer of holes at the perovskite/HTL interface, while greatly boosting interfacial charge separation and collection, [185, 197] consequently leading to the increased V_{OC} and FF.

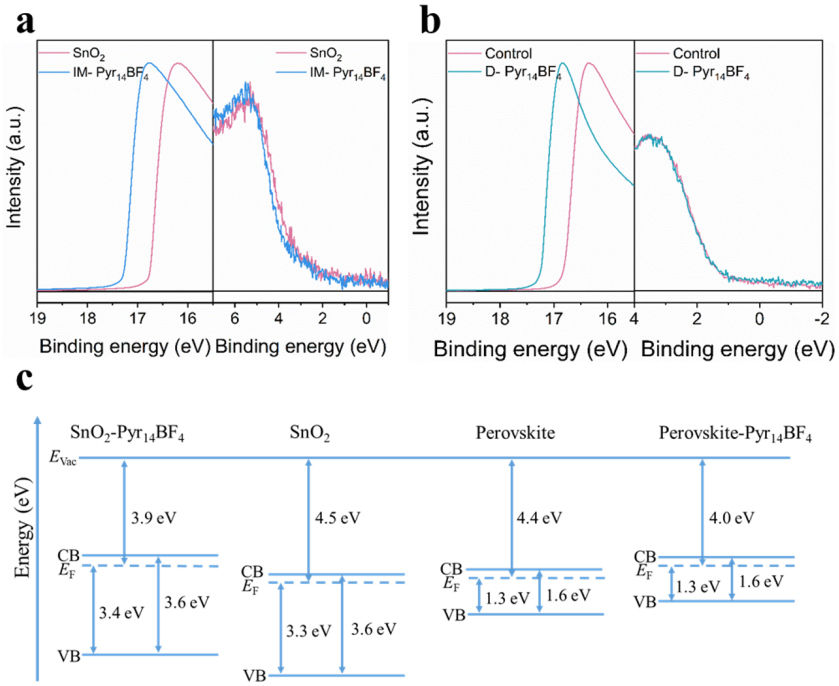

Figure 7.13: UPS spectra of secondary electron cut-off and valence band edge of (a) SnO_2 and SnO_2-$Pyr_{14}BF_4$ films and (b) control and D-$Pyr_{14}BF_4$ perovskite films. (c) Schematic illustration of energy levels based on UPS and UV-vis measurements. Adopted with permission from Ref [175]. Copyright © 2023 Elsevier.

Sample	E_{cutoff} (eV)	E_{onset} (eV)	WF (eV)	E_g (eV)	VBM (eV)	CBM (eV)
SnO_2	16.7	3.3	4.5	3.6	7.8	4.2
SnO_2-$Pyr_{14}BF_4$	17.3	3.4	3.9	3.6	7.3	3.7
Perovskite	16.8	1.3	4.4	1.6	5.7	4.1
D-$Pyr_{14}BF_4$	17.3	1.3	4.0	1.6	5.2	3.6

Table 7.4: Energy level parameters obtained from ultraviolet photoelectron spectroscopy (UPS) and UV-vis. Adopted with permission from Ref [175]. Copyright © 2023 Elsevier. (Note: the band gap of SnO_2 is the theoretical value, [198] and our experiment shows the introduction can't influence the bandgap of SnO_2)

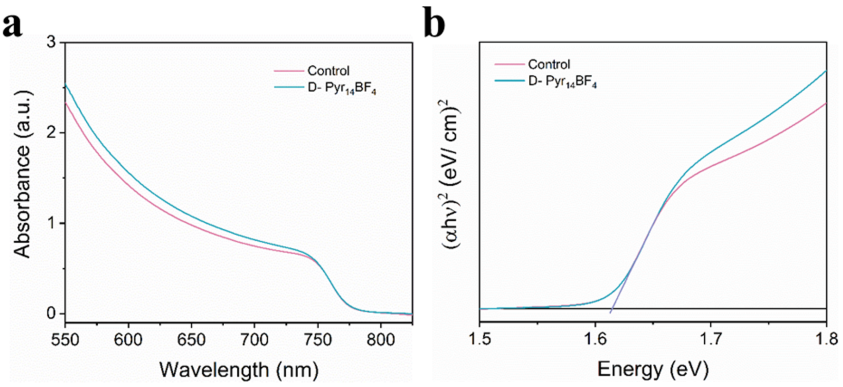

Figure 7.14: (a) UV-vis spectra of glass/perovskite and glass/perovskite doped with $Pyr_{14}BF_4$ (b) Tauc plot of glass/perovskite and glass/perovskite doped with $Pyr_{14}BF_4$. Adopted with permission from Ref [175]. Copyright © 2023 Elsevier.

7.5 Recombination kinetics

The build-up and disappearance of charge carrier densities in PSCs involve multiple processes: Light absorption and charge carrier generation, separation, transport, extraction and recombination in the bulk or at interfaces. Maximizing charge carrier generation and transport while minimizing recombination is universally perceived being important for optimizing device efficiencies. [32,137,181] Time-resolved measurements, which are extensively implemented in photovoltaic characterization, can reveal fundamental mechanisms such as voltage and current generation, as well as competitive charge carrier recombination within devices. [32, 199] Herein, the crucial role of ionic liquids on such dynamic processes in perovskite thin films and devices is investigated using transient optical and electrical measurements.

7.5.1 Optical characterization

Contactless optical methods such as steady-state PL and TRPL were implemented to provide insights into excited state and charge carrier dynamics in the active materials. Figure 7.15a and b shown the TRPL curves that are fitted with bi-exponential functions and the fit parameters were listed in Table 7.5.

The extracted τ_{ave} were 44.5, 38.6, 48.1, 73.2, 132.2, 128.4, and 64.7 ns for IM-4.3, IM-2.9, IM-1.4 mM, control, D-1, D-2, D-3 mM $Pyr_{14}BF_4$ perovskite films, respectively. The increase of τ_{ave} with respect to the control sample, especially for $Pyr_{14}BF_4$ concentration between 1 mM and 2 mM, was consistent with the suppression of defect-assisted

non-radiative recombination pathways in the perovskite film. This suggested that the introduction of $Pyr_{14}BF_4$into active materials resulted in lower concentrations of defect states that act as recombination centers and thus was beneficial to photo-generated charge carrier extraction. [192, 200] Indeed, the concentration dependence of the decay time reproduced the trend observed for the $Pyr_{14}BF_4$ concentration dependence of the PCE (see Figure 7.10d). This corroborated the assignment to suppression of defect-assisted recombination through $Pyr_{14}BF_4$.

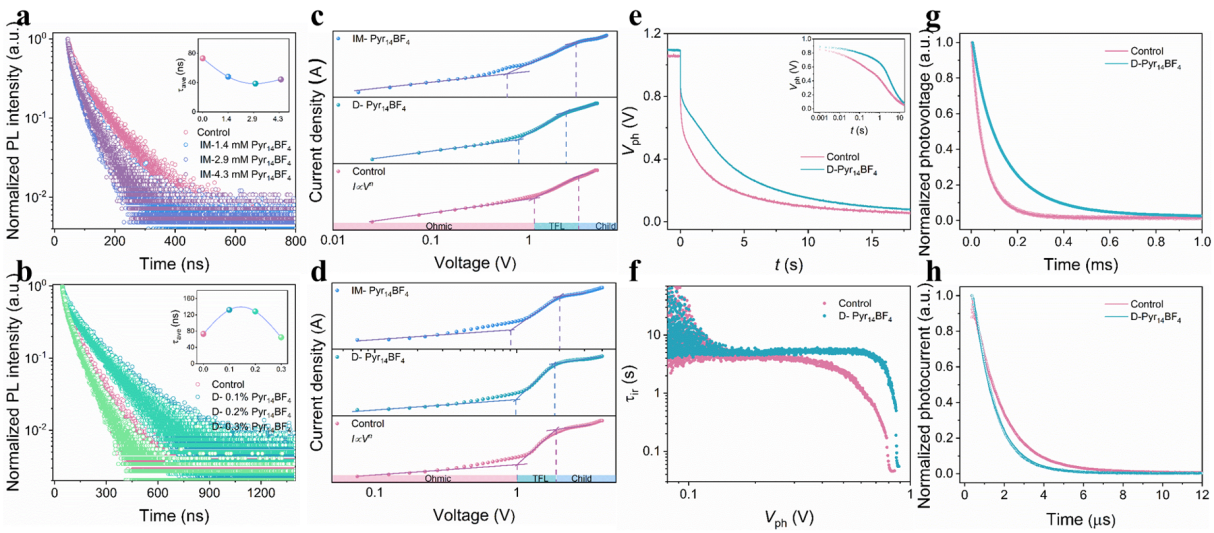

Figure 7.15: Time-resolved PL decay spectra of (a) perovskite films with SnO_2 treated with different $Pyr_{14}BF_4$ concentrations and (b) perovskite films doped with different $Pyr_{14}BF_4$ ratios. Characteristic *J-V* trace of (c) electron-only devices based on glass/ITO/SnO_2/Perovskite/PCBM/Au architecture and (d) hole-only devices based on glass/ITO/PTAA/Perovskite/Spiro-OMeTAD/Au architecture. Showing three different regions obtained from the log I versus log V plots with marked for Ohmic ($I \propto V^{n=1}$), TFL ($I \propto V^{n>3}$), and Child's regimes ($I \propto V^{n=2}$). (e) Open-circuit voltage decay (OCVD) traces. (f) Instantaneous relaxation time as a function of voltage. (g) Transient photovoltage traces. (h) Transient photocurrent traces of the control and $Pyr_{14}BF_4$-containing devices. Adopted with permission from Ref [175]. Copyright © 2023 Elsevier.

Fundamental quantities such as charge carrier trap density (n_{trap}) and charge carrier mobility (μ), which directly affect the potential of the material for application in PSCs, were investigated via SCLC measurements (Figure 7.15c and d). [201] The calculated conductivities (σ), n_{trap}, and μ of the three investigated samples were listed in Table 7.6 and Table 7.7, respectively, with the calculations detailed in the methods section.

Sample	A_1	τ_1 (ns)	A_2	τ_2 (ns)	τ_{ave} (ns)
IM-4.3 mM $Pyr_{14}BF_4$	0.48	10.44	0.56	50.46	44.5
IM-2.9 mM $Pyr_{14}BF_4$	0.62	9.77	0.51	46.19	38.6
IM-1.3 mM $Pyr_{14}BF_4$	0.40	11.15	0.58	53.40	48.1
Control	0.40	14.43	0.59	80.34	73.2
D-1 mM $Pyr_{14}BF_4$	0.34	20.98	0.62	141.23	132.2
D-2 mM $Pyr_{14}BF_4$	0.32	26.58	0.61	138.68	128.4
D-3 mM $Pyr_{14}BF_4$	0.47	16.41	0.55	73.94	64.7

Table 7.5: Parameters of TRPL spectroscopy based on the TTO/perovskite. Adopted with permission from Ref [175]. Copyright © 2023 Elsevier.

Sample	Thickness L (nm)	Conductivities σ (Ω^{-1} cm^{-1})	Trap density n_t (cm^{-3})	Mobilities μ (cm^2 V^{-1} s^{-1})
Control	600	14.04	8.85×10^{15}	3.11×10^{-3}
D-$yr_{14}BF_4$	611	3.19	5.89×10^{15}	3.73×10^{-3}
IM-$Pyr_{14}BF_4$	592	1.84	6.68×10^{15}	1.31×10^{-3}

Table 7.6: Calculated parameters of the electron-only devices. Adopted with permission from Ref [175]. Copyright © 2023 Elsevier.

Sample	Thickness L (nm)	Conductivities σ (Ω^{-1} cm^{-1})	Trap density n_t (cm^{-3})	Mobilities μ (cm^2 V^{-1} s^{-1})
Control	600	7.85	7.99×10^{15}	3.15×10^{-3}
D-$yr_{14}BF_4$	611	12.02	7.48×10^{15}	3.75×10^{-3}
IM-$Pyr_{14}BF_4$	592	15.41	7.33×10^{15}	2.70×10^{-3}

Table 7.7: Calculated parameters of the hole-only devices. Adopted with permission from Ref [175]. Copyright © 2023 Elsevier.

Based on electron-only devices (Table 7.6), the calculated trap density was 8.85×10^{15} cm^{-3} for the control, 5.89×10^{15} cm^{-3} for D-$Pyr_{14}BF_4$ and 6.68×10^{15} cm^{-3} for IM-$Pyr_{14}BF_4$ devices. The corresponding charge carrier mobility was 3.11×10^{-3} cm^2 V^{-1} s^{-1} for the control, 3.73×10^{-3} cm^2 V^{-1} s^{-1} for D-$Pyr_{14}BF_4$ and 1.31×10^{-3} cm^2 V^{-1} s^{-1} for IM-$Pyr_{14}BF_4$ devices. The substantially decreased trap density and the enhanced charge

carrier mobility estimated from D-$Pyr_{14}BF_4$ devices implied that ionic liquids positively reduced detrimental defect concentrations while also driving rapid charge carrier collection. These conclusions extracted from electron-only devices were almost identical to those drawn from hole-only devices (Figure 7.15d and Table 7.7). The lower trap density and higher charge carrier mobility acquired in D-$Pyr_{14}BF_4$ devices demonstrated the optimization effect of $Pyr_{14}BF_4$ on the optoelectronic properties, suppressing the recombination of charge carriers besides facilitating charge separation and transport, leading to a higher FF.

7.5.2 Electrical characterization

Direct electrical time-domain measurements of contacted photovoltaic materials such as OCVD, TPV and TPC, were used to determine recombination dynamics in terms of charge carrier lifetimes.

Two different types of perturbation, including larger perturbation photovoltage decays (OCVD) and small perturbation photovoltage decays (TPV), were conducted to describe the photovoltage behavior of PSCs. TPV is differentiated from OCVD, as the latter is a continuous measurement that provides extremely high resolution in voltage. The OCVD traces were obtained by recording the voltage variation due to the disappearance of the excess photo-generated charge carriers by recombination after turning off a green LED, which was used as an illumination source to generate the photovoltage. Two distinct photo-induced changes were observed (Figure 7.15e). One is the rapid increase in the decay rate manifested as a rapid drop in the decay curves, which is associated with the rapid recombination occurring on both interfaces as the high charge carrier concentration remained after turning off the LED. The other one is the build-up of electrostatic potential, as a result of the ion accumulation at the interface. [199, 202] Both devices displayed a long photovoltage decay with times of up to tens of seconds, with the $Pyr_{14}BF_4$-containing device exhibiting a substantially slower voltage decay than the control. To further quantify the analysis of the OCVD data, the corresponding instantaneous relaxation times, τ_{ir}, were calculated from the following expression (1), which was used to describe the instantaneous variation of the relaxation, depicted in Figure 7.15f

$$\tau_{ir}(V) = \left(-\frac{1}{V}\frac{dV}{dt}\right)^{-1} \tag{7.1}$$

Both devices displayed a similar shape of the relaxation time and consisted of two decay components. At high voltage, the τ_{ir} undergo a rapid transition at short times towards larger time-scale decay. The relatively fast decay components observed are associated with electrical phenomena, i.e., the discharge and recombination of photo-generated electrons

and holes. [203] After that, the traces entered a region close to the plateau and shown a power-law decay (non-exponential) at longer times. The slow decay component is related to the overall polarization status of devices induced by ion accumulation. [203] It was reported that the electronic trap in the center of the gap cannot cause relaxation at long time scales but has effects on the electron recombination dynamics at shorter time scales. [203] Thus, the observed longer lifetimes in the $Pyr_{14}BF_4$-containing device at short time scales implied a lower concentration of deep traps that cause strong Shockley-Read-Hall recombination. At the long-time decay, the log τ vs. log V plots of both devices overlap.

As a complement to the OCVD results, I performed small perturbation TPV to detect faster decay components with relaxation times in the ms scale. The TPV depicted in Figure 7.15g. Table 7.8 listed the calculated electron lifetimes τ_e gained by fitting the TPV traces with bi-exponential functions.

Sample		Control	D-$yr_{14}BF_4$
TPC	τ(μs)	1.53	1.09
	A_1(%)	0.47	0.57
	τ_1 (ms)	0.03	0.09
TPV	A_2(%)	0.56	0.45
	τ_2 (ms)	0.08	0.21
	τ_{ave} (ms)	0.06	0.15

Table 7.8: Parameters of TPV and TPC curves obtained from exponential fits. Adopted with permission from Ref [175]. Copyright © 2023 Elsevier.

The high concentration of defects would provide vacancy-mediated pathways and sites for ion migration and superoxide generation, respectively, which is detrimental to the overall performance and operational stability of PSCs. [183, 204] The prolonged τfound in the $Pyr_{14}BF_4$-containing device (0.06 ms for control, 0.15 ms for $Pyr_{14}BF_4$-containing device) implied a reduced trap density in the active material and substantially suppressed charge carrier recombination, leading to relatively low recombination rates and superior stability. High charge carrier generation, low charge carrier recombination rates and fast charge carrier transport are considered to be the key indicators for evaluating the electrical properties of PSCs. The combination of a short recombination lifetime and fast transport assures a high electron collection efficiency. [205]

TPC was performed to further verify the photo-generated electron extraction and transportation at μs time scales (Figure 7.15h). The charge carrier lifetimes τ, extracted from TPC traces fitted by a single exponential function, decreased from 1.53 to 1.09 μs after $Pyr_{14}BF_4$ incorporation (Table 7.8), suggesting that more effective charge carrier extraction arises from the faster charge carrier transfer rate from perovskite to the SnO_2 layer. This highlighted the importance of ionic liquids in rapidly removing electrons from the photoactive layer before being captured by traps.

The transient measurements described above confirmed the crucial impact of ionic liquid on the charge carrier kinetics (recombination, extraction, and transport) and the photovoltage behavior of PSCs on picosecond to millisecond time scales. The accelerated charge carrier transport and more efficient electron extraction realized in the $Pyr_{14}BF_4$-containing devices minimized the probability of charge carriers being trapped by defects, which was vital to the overall photovoltaic performance of PSCs, especially for improvement in FF. This also confirmed the hypothesis I propose from the analysis of GIWAXS data that films with preferential corner-up orientation exhibited improved charge transport and extraction characteristics.

7.6 Stability of perovskite thin films and devices

The composition of the active materials in PSCs is extremely sensitive to the external environment. Exposure to moisture, oxygen, and heat will cause rapid degradation. Therefore, the long-term operational stability of PSCs was also investigated.

7.6.1 Structure and morphology variation during device operation

To study operation-induced changes of the perovskite structure and morphology, the operando GIWAXS measurements on PSCs with continuous voltage-bias scans and illumination were performed under ambient conditions (Figure 7.16 and Figure 7.17). The selected incident angle α_i was 0.6°, ensuring that the X-ray beam penetrates the entire film and yields information on the entire active layer. The time evolution of 2D GIWAXS data for the control device demonstrated a remarkable lattice contraction as seen in the azimuthally integrated line profiles (Figure 7.18a). The position of the (110) Bragg peak decreased slightly from 1.022 to 1.021 $Å^{-1}$ during the first 30 min of illumination, after which it increased significantly from 1.021 to 1.024 $Å^{-1}$ during the subsequent illumination (Figuree 7.18c). In contrast, the temporal evolution of the line profiles indicated that

the $Pyr_{14}BF_4$-containing PSC undergo a slight lattice expansion during the first 10 min of illumination and thereafter remained practically unchanged (Figuree 7.18b ande 7.18d).

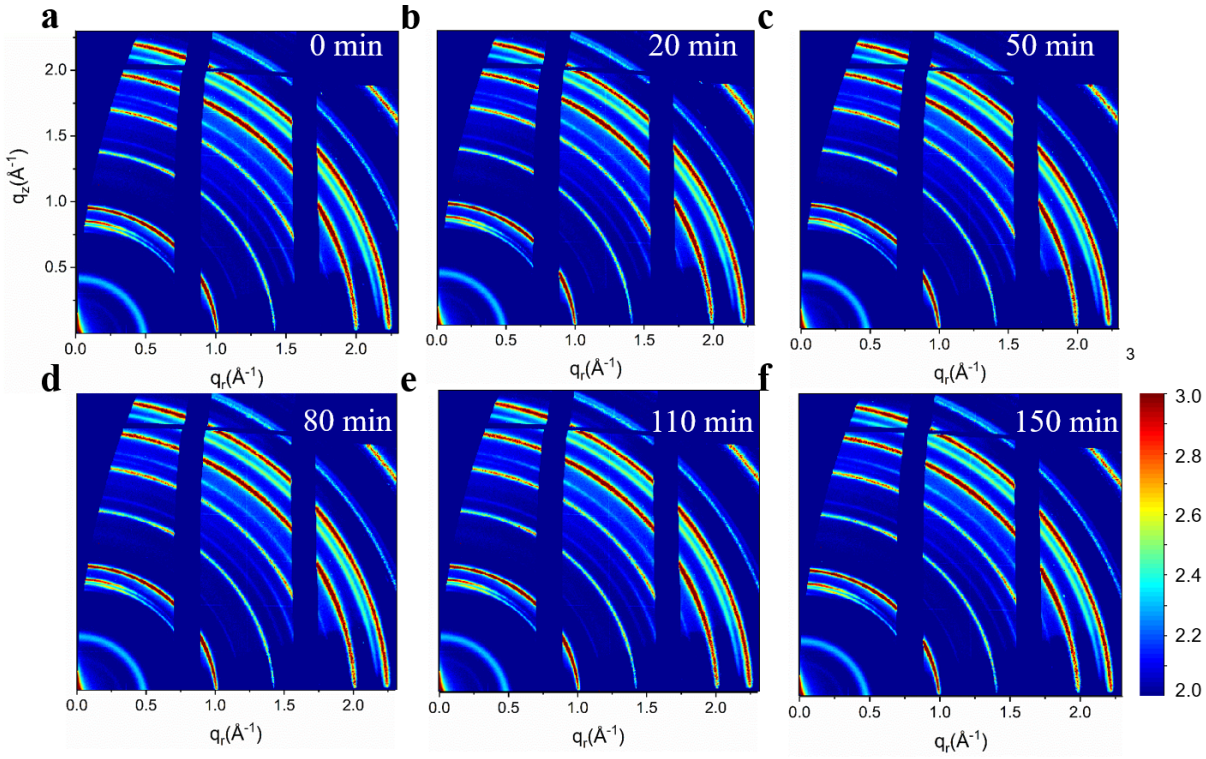

Figure 7.16: Temporal evolution of the 2D GIWAXS data of device based on ITO/SnO_2/perovskite/Spiro-OMeTAD/Au under illumination with full-spectrum sunlight at 25 °C in air with a relative humidity (RH) ranging from 20 % to 30 %: (a) 0 min, (b) 20 min, (c) 50 min, (d) 80 min, (e) 110 min and (f) 150 min. Adopted with permission from Ref [175]. Copyright © 2023 Elsevier.

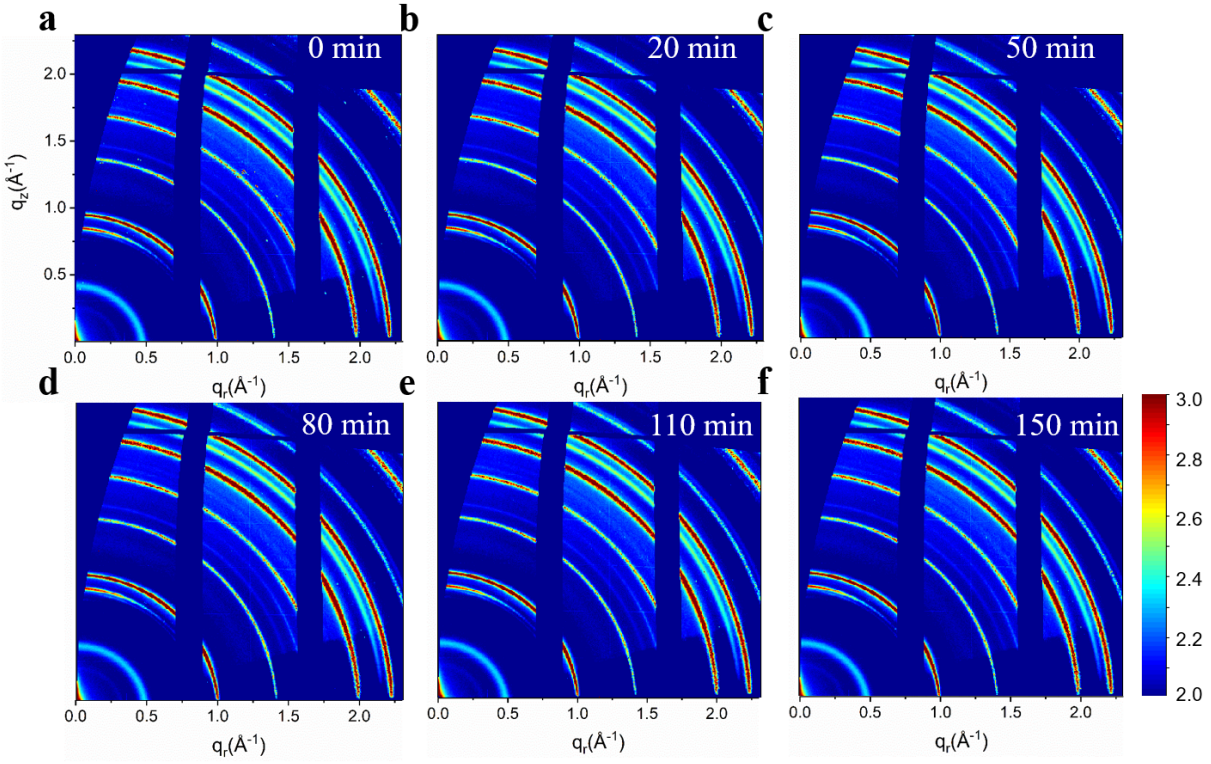

Figure 7.17: Temporal evolution of the 2D GIWAXS data of device based on ITO/SnO_2/perovskite doped with $Pyr_{14}BF_4$/Spiro-OMeTAD/Au under illumination with full-spectrum sunlight at 25 °C in air with relative humidity (RH) ranging from 20 % to 30 %: (a) 0 min, (b) 20 min, (c) 50 min, (d) 80 min, (e) 110 min and (f) 150 min. Adopted with permission from Ref [175]. Copyright © 2023 Elsevier.

Next, I performed GISAXS measurements at an incident angle of 0.35°, which is above the critical angle (α_c) of all involved materials, to investigate the morphological evolution of PSCs during operation under ambient conditions. Selected 2D GISAXS data of both devices were displayed in Figure 7.19 and Figure 7.20. To quantify the results from operando GISAXS, I analyzed the temporal evolution of the horizontal line cuts and modeled these data with form and structure factors in the framework of the distorted wave Born approximation (DWBA), as seen in Figure 7.18e and Figure 7.18f. [51,206,207] Three cylindrical form factors with different radii were implemented to fit the curves within the local monodisperse approximation that regards the scattering signals as the superposition of scattering from monodisperse domains with different size ranges. The structure factor described the center-to-center distances between adjacent domains. The time evolution of the extracted characteristic lateral structural dimensions for the control device under illumination was significantly different from the D-$Pyr_{14}BF_4$ device (Figure 7.18g and Figure 7.18h). In the control device, the radii of large domains decreased while those

of the medium domains gradually increased. In contrast, only minor changes in domain sizes were observed for the $Pyr_{14}BF_4$-containing device.

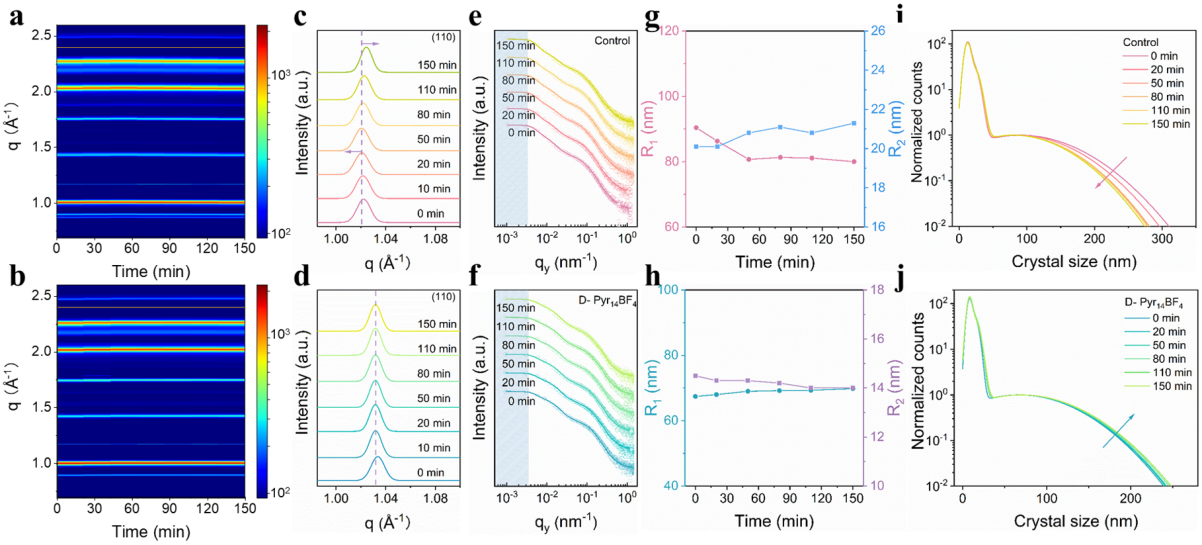

Figure 7.18: Time evolution of operando GIWAXS data plotted as azimuthally integrated line profiles of the 2D GIWAXS data for the operation of PSCs at ambient conditions for (a) the control and (b) D-$Pyr_{14}BF_4$ devices. Evolution of radial GIWAXS profiles integrated over all azimuthal angles (pseudo-XRD profiles) during operation for PSCs at ambient conditions for (c) the control and (d) D-$Pyr_{14}BF_4$ devices. Horizontal line cuts of the 2D GISAXS data extracted at the Yoneda peak position for (e) the control and (f) D-$Pyr_{14}BF_4$ devices. Characteristic lateral structure sizes extracted from the model curves of (g) the control (h) D-$Pyr_{14}BF_4$ devices, respectively. Evolution of lateral size distributions under operation at ambient conditions for (i) the control and (j) D-$Pyr_{14}BF_4$ devices. Adopted with permission from Ref [175]. Copyright © 2023 Elsevier.

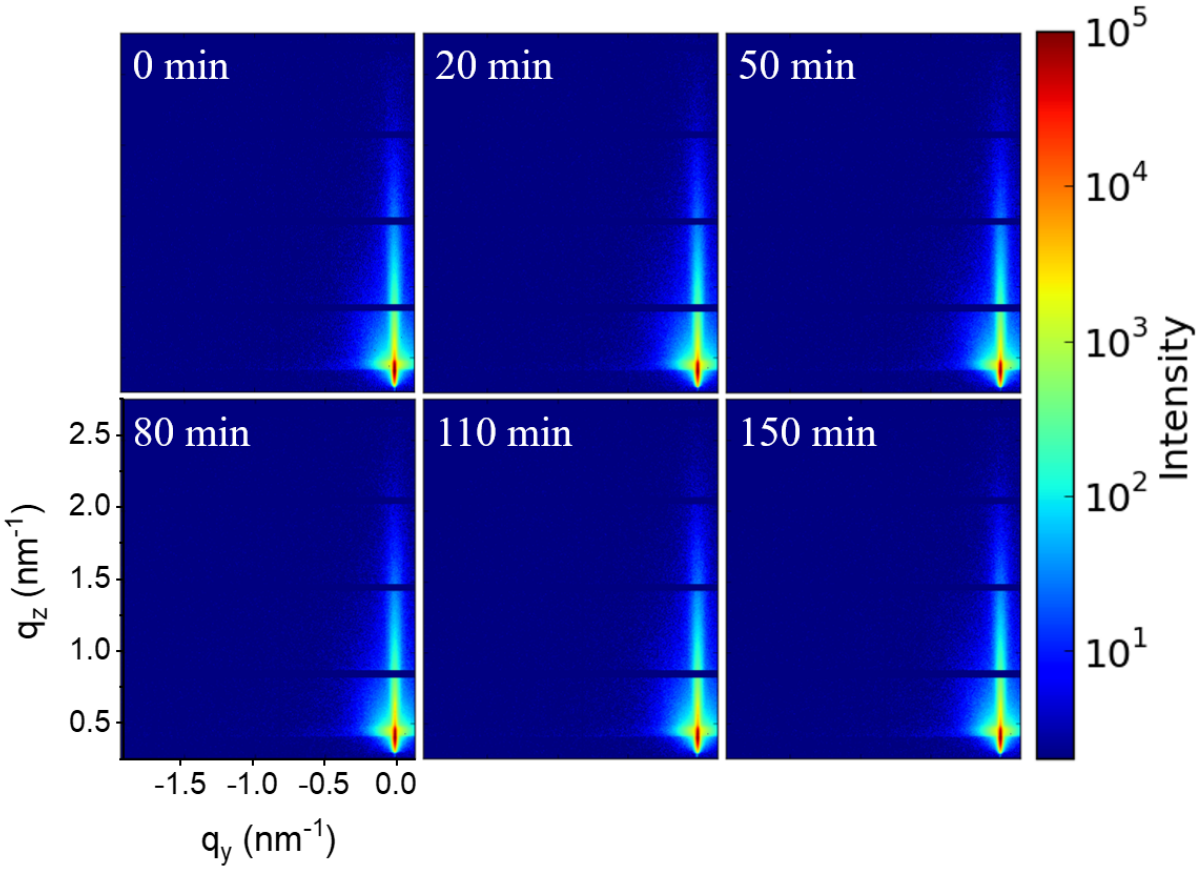

Figure 7.19: Temporal evolution of the 2D GISAXS data of device based on ITO/SnO_2/perovskite/Spiro-OMeTAD/Au under illumination with full-spectrum sunlight at 25 °C in air with relative humidity (RH) ranging from 20 % to 30 %: (a) 0 min, (b) 20 min, (c) 50 min, (d) 80 min, (e) 110 min and (f) 150 min. Adopted with permission from Ref [175]. Copyright © 2023 Elsevier.

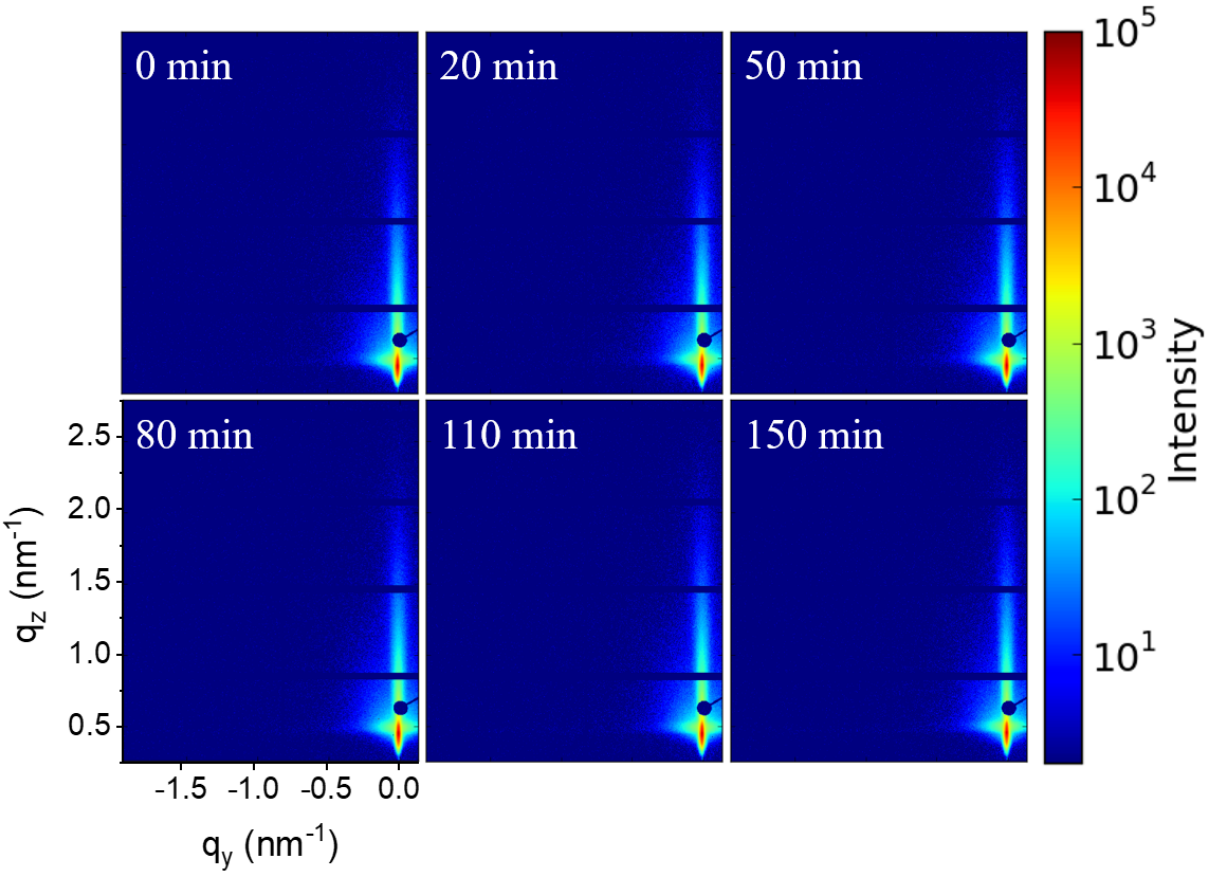

Figure 7.20: Temporal evolution of the 2D GIWAXS data of device based on ITO/SnO_2/perovskite doped with $Pyr_{14}BF_4$/Spiro-OMeTAD/Au under illumination with full-spectrum sunlight at 25 °C in air with relative humidity (RH) ranging from 20 % to 30 %: (a) 0 min, (b) 20 min, (c) 50 min, (d) 80 min, (e) 110 min and (f) 150 min. Adopted with permission from Ref [175]. Copyright © 2023 Elsevier.

To further analyze the operando GISAXS data, lateral size distributions were calculated from the individual form factors used in the data modeling (Figure 7.18i and Figure 7.18j). [208] In the control device, the number of large-sized domains gradually decreased as the operation time increased, while the number of small-sized domains concomitantly increase. This change in the domain size distribution was directly linked to a strain-induced splitting of large perovskite grains into smaller-sized crystals. [208] Such a grain fragmentation phenomenon was reported in a previous operando study of PSCs. [209] The slight increase in the number of large-sized domains observed in the $Pyr_{14}BF_4$-containing device might be explained by the strain-induced merging of smaller crystals on the surface with larger crystals in the film via an epitaxial assimilation process. [208] In an alternative explanation, small crystals could be consumed via the growth of larger crystals through Ostwald ripening under continuous illumination. [208] Such

a behavior was also expected to occur in the control device, which means that I observed a competition between large grain fragmentation and small crystal coalescence in the control device. The increased number of medium-sized domains resulting from grain fragmentation introduced additional grain boundaries that were the primary regions for charge carrier recombination, which was detrimental to device performance. [209] Importantly, this implied that the morphological stability of the ionic liquid-containing device will favorably impact operational PSC performance characteristics.

7.6.2 Device stability under operation

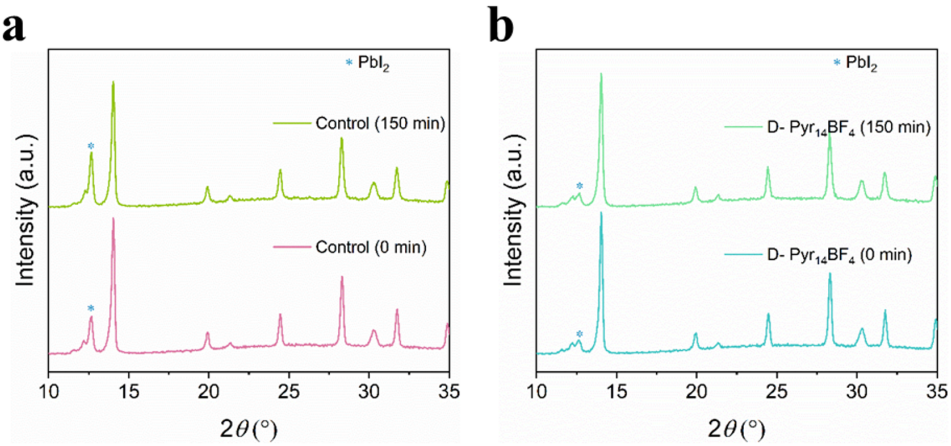

Figure 7.21: XRD data of pristine and aged films of (a) the control and (b) $Pyr_{14}BF_4$–containing films on SnO_2/ITO coated glass substrates. The blue stars and blue cross represent the PbI_2 and δ-$FAPbI_3$ phase, respectively. Adopted with permission from Ref [175]. Copyright © 2023 Elsevier.

XRD data of the control film before and after 2.5 h of light soaking revealed an enhanced PbI_2 peak (marked with blue stars) (Figure 7.21a), implying additional PbI_2 phase generation under continuous illumination. Such an increase could originate from MAPI decomposition induced by the superoxide generated in the presence of light or oxygen. [19, 184] In contrast, no excess PbI_2 phase was found in the light-soaked $Pyr_{14}BF_4$–containing perovskite films (Figure 7.21b).

To further quantity chemical changes to the film components, I conducted XPS measurements before and after light illumination (Figure 7.22). The results of the spectral analysis were listed in Tables 7.9 to 7.12. In brief, I found that the I/Pb ratio in the control film decreased by 14 % (from 4.62 to 3.96), while that of the $Pyr_{14}BF_4$–containing perovskite film only decreased by 6 % (from 4.81 to 4.53) during 2.5 h light soaking. The

decrease in the I/Pb ratios implied that more PbI_2 migrated to the perovskite surface. [209] Accumulation of PbI_2 at the interface could be caused by light-induced degradation of the near-surface region.

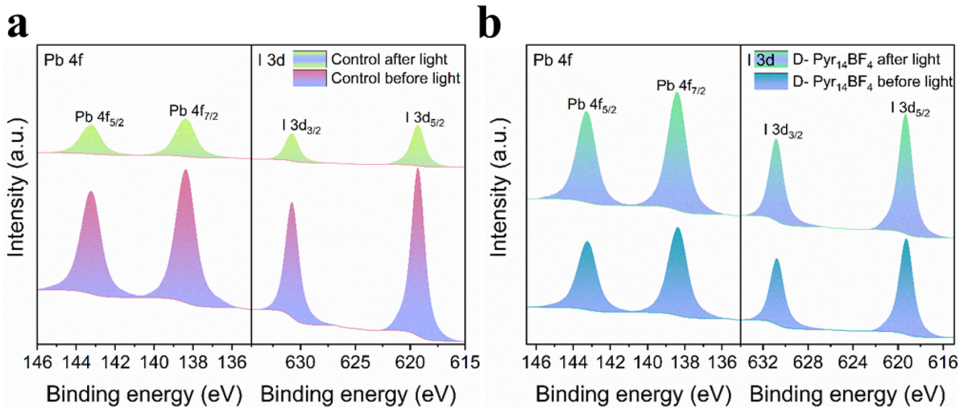

Figure 7.22: XPS spectra of Pb and I before and after light illumination: (a) Control and (b) $Pyr_{14}BF_4$–containing films based on Si substrates. Adopted with permission from Ref [175]. Copyright © 2023 Elsevier.

Perovskite Only				I/Pb ratio
Core level	Binding energy (eV)	% At Conc	Spectral component	Main peak
I 3d	617.7	6.70	I^{3-}	4.39
I3d	619.3	67.85	Perovskite	
I3d	620.7	7.66	PbI_2	Whole peak area
Pb 4f	136.9	1.18	Pb_0	4.62
Pb 4f	138.4	15.46	Perovskite	
Pb 4f	39.6	1.15	PbI_2	

Table 7.9: Peak information of iodine 3d (I 3d) and lead 4f (Pb 4f) gained through fits of the XPS spectra based on Si/perovskite before light exposure. Adopted with permission from Ref [175]. Copyright © 2023 Elsevier.

	Perovskite	Only	After Light	I/Pb ratio
Core level	Binding energy (eV)	% At Conc	Spectral component	Main peak
I 3d	617.8	6.29	I^{3-}	3.71
I3d	619.3	66.15	Perovskite	
I3d	620.7	7.39	PbI_2	Whole peak area
Pb 4f	137.0	1.12	Pb_0	3.96
Pb 4f	138.4	17.82	Perovskite	
Pb 4f	39.5	1.23	PbI_2	

Table 7.10: Peak information of iodine 3d (I 3d) and lead 4f (Pb 4f) gained through fits of the XPS spectra based on Si/perovskite after light exposure. Adopted with permission from Ref [175]. Copyright © 2023 Elsevier.

	D-$Pyr_{14}BF_4$	Perovskite		I/Pb ratio
Core level	Binding energy (eV)	% At Conc	Spectral component	Main peak
I 3d	617.7	6.93	I^{3-}	4.54
I3d	619.3	67.79	Perovskite	
I3d	620.7	8.07	PbI_2	Whole peak area
Pb 4f	137.0	1.05	Pb_0	4.81
Pb 4f	138.4	14.92	Perovskite	
Pb 4f	39.5	1.23	PbI_2	

Table 7.11: Peak information of iodine 3d (I 3d) and lead 4f (Pb 4f) gained through fits of the XPS spectra based on Si/perovskite doped with $Pyr_{14}BF_4$ before light exposure. Adopted with permission from Ref [175]. Copyright © 2023 Elsevier.

	D-$Pyr_{14}BF_4$	Perovskite	After Light	I/Pb ratio
Core level	Binding energy (eV)	% At Conc	Spectral component	Main peak
I 3d	617.7	6.62	I^{3-}	4.25
I3d	619.3	68.40	Perovskite	
I3d	620.8	6.90	PbI_2	Whole peak area
Pb 4f	137.1	0.89	Pb_0	4.53
Pb 4f	138.4	16.08	Perovskite	
Pb 4f	39.6	1.11	PbI_2	

Table 7.12: Peak information of iodine 3d (I 3d) and lead 4f (Pb 4f) gained through fits of the XPS spectra based on Si/perovskite doped with $Pyr_{14}BF_4$ after light exposure. Adopted with permission from Ref [175]. Copyright © 2023 Elsevier.

I further investigated the operational stability of PSC devices aged under simulated full-spectrum sunlight in ambient air (relative humidity of approximately 20-30 %). The evolution of normalized average photovoltaic parameters obtained from 5 devices for each condition was plotted in Figure 7.23. I observed a positive light-soaking effect on $Pyr_{14}BF_4$-containing devices so that the normalized PCE increased by 5 % during aging, which was a consequence of improvements in the FF and J_{SC}. In contrast, the normalized PCE of the control devices decreased sharply during the first 30 min of operation. The enhanced efficiency observed in the $Pyr_{14}BF_4$-containing devices under illumination can be a consequence of the photo-brightening effect resulting from defect passivation in the perovskite film via reaction with photo-generated superoxide and peroxide species. [179, 210, 211] In addition, the higher starting PCE of the $Pyr_{14}BF_4$-containing devices was attributed to the lower trap densities in these films, which reduced both recombination and ion-migration, thereby allowing more efficient collection of charge carriers at the electrodes. [212] Furthermore, the subsequent stabilization of the efficiency was explained by the established balance between the generation of photo-excited charge carriers and the trap densities originating from the perovskite degradation induced by light. In contrast, the observed initial decrease in efficiency in the control devices can be ascribed to two factors: First, a significantly higher defect concentration was present in the pristine films, which results in a higher capture rate of charge carriers. Under continuous illumination, the local fields created by the filling of traps can induce ion migration, further reducing efficiency. [212] Second, a higher concentration of defects was created by the continuous light-induced decomposition of the perovskite components. The eventual stabilization of efficiency could arise from the formation of the Pb-O bond networks from the

reaction between Pb atoms predominantly at the perovskite surface and peroxide under continuous illumination. [211, 213] The oxidation process compensated for the degradation loss by reducing the number of charge-trapping states. The decrease in the V_{OC} traces was likely caused by the trap-assisted non-radiative recombination that occurred in the perovskite absorber and the poor electronic quality of perovskite/charge-transport-layer heterojunctions, leading to heterojunction-induced non-radiative losses. [214] The relatively slight decrease of V_{OC} observed in the $Pyr_{14}BF_4$-containing devices originated from the lower defect concentration and more efficient extraction, leading to a lower non-radiative recombination rate. Thus, the incorporation of ionic liquid into the perovskite provided a promising route to reach higher open-circuit voltages and radiative efficiencies by minimizing the defects responsible for non-radiative recombination and developing an efficient perovskite/charge extraction layer.

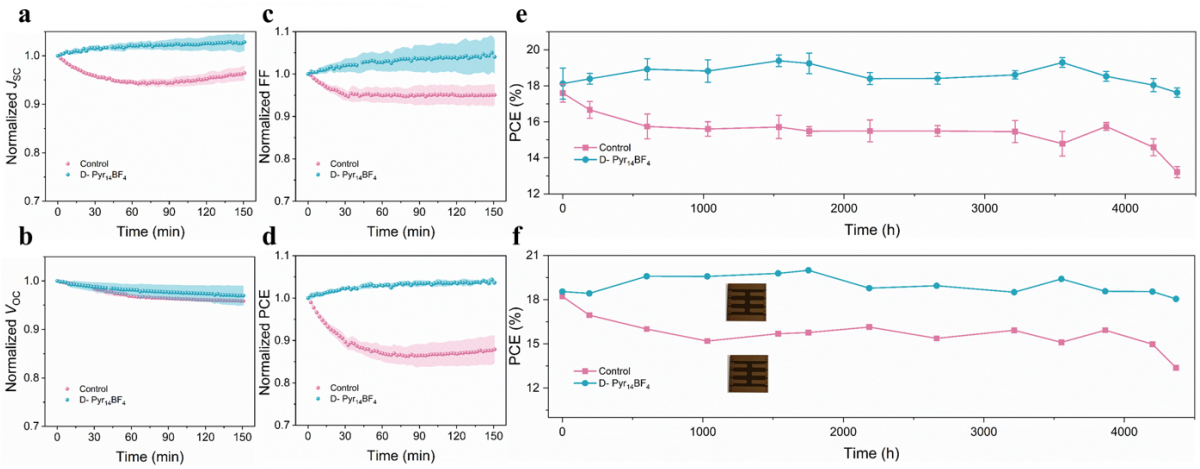

Figure 7.23: Evolution of photovoltaic parameters measured by the reverse scan (from 1.3 V to -0.2 V) under the ISOS-L-1 protocol at ambient conditions. The shaded areas indicate error bars extracted from the standard deviation of normalized (a) J_{SC}, (b) V_{OC}, (c) FF and (d) PCE values of five devices. (e) PCE evolution of non-encapsulated devices aged at 20-30 °C in air with a relative humidity (RH) in the range from 20 % to 30 %, including standard errors calculated from five devices. (f) PCE evolution of the best-performing device under the same aging conditions as in (e). Adopted with permission from Ref [175]. Copyright © 2023 Elsevier.

7.6.3 Long-term stability of devices in ambient conditions

Having demonstrated the stability of $Pyr_{14}BF_4$–containing perovskite films, I proceed to investigate the stability of non-encapsulated PSCs under ambient conditions. Figure 7.23e shown the average PCE variation calculated from 5 devices operated at 20-30 °C in the

air with relative humidity (RH) in the range from 20 % to 30 %. The corresponding statistical parameter values were listed in Tables 7.13 and 7.14.

Time (h)	Devices	J_{SC} (mA cm^{-2})	V_{OC} (V)	FF	PCE (%)
0	Average	22.91 ± 0.33	1.10 ± 0.02	0.70 ± 0.03	17.60 ± 0.50
	Champion	22.84	1.08	0.74	18.21
192	Average	22.40 ± 0.59	1.06 ± 0.03	0.70 ± 0.03	16.67 ± 0.47
	Champion	22.60	1.03	0.73	16.94
600	Average	22.35 ± 0.62	1.07 ± 0.02	0.66 ± 0.02	15.75 ± 0.69
	Champion	22.89	1.06	0.66	16
1032	Average	22.10 ± 0.43	1.07 ± 0.06	0.66 ± 0.04	15.61 ± 0.40
	Champion	21.75	1.01	0.69	15.19
1536	Average	22.21 ± 0.34	1.06 ± 0.02	0.67 ± 0.02	15.72 ± 0.65
	Champion	22.18	1.07	0.66	15.68
1752	Average	22.03 ± 0.48	1.09 ± 0.04	0.65 ± 0.04	15.49 ± 0.25
	Champion	21.75	1.05	0.69	15.76
2184	Average	21.82 ± 1.12	1.08 ± 0.04	0.66 ± 0.04	15.50 ± 0.61
	Champion	22.84	1.02	.70	16.13
2664	Average	21.75 ± 0.16	1.06 ± 0.03	0.67 ± 0.01	15.50 ± 0.30
	Champion	21.85	1.02	0.69	15.36
3216	Average	21.87 ± 0.71	1.08 ± 0.03	0.66 ±0.02	15.50 ± 0.61
	Champion	22.90	1.06	0.66	15.92
3552	Average	22.24 ± 0.37	1.08 ± 0.03	0.62 ± 0.05	14.79 ± 0.69
	Champion	22.10	1.04	0.66	15.09
3864	Average	22.48 ± 0.45	1.08 ± 0.02	0.65 ± 0.02	15.75 ± 0.22
	Champion	22.16	1.08	0.67	15.92
4200	Average	21.93 ± 0.70	1.05 ± 0.04	0.64 ±0.04	14.59 ± 0.47
	Champion	22.58	1.00	0.68	14.97
4368	Average	20.86 ± 0.68	1.04 ± 0.04	0.61 ±0.03	13.21 ± 0.31
	Champion	21.28	0.99	0.64	13.37

Table 7.13: Summarized photovoltaic parameters of the long-term stability performance of the most stable device based on ITO/SnO_2/perovskite/Spiro-OMeTAD/Au. Adopted with permission from Ref [175]. Copyright © 2023 Elsevier.

Time (h)	Devices	J_{SC}(mA cm^{-2})	V_{OC} (V)	FF	PCE (%)
0	Average	23.07 ± 0.49	1.11 ± 0.02	0.71 ± 0.02	18.13 ± 0.85
	Champion	23.51	1.11	0.71	18.54
192	Average	23.23 ± 0.32	1.09 ± 0.02	0.73 ± 0.02	18.39 ± 0.29
	Champion	23.50	1.11	0.71	18.42
600	Average	23.51 ± 0.27	1.11 ± 0.04	0.73 ± 0.02	18.92 ± 0.58
	Champion	23.19	1.14	0.74	19.58
1032	Average	23.23 ± 0.42	1.14 ± 0.04	0.71 ± 0.02	18.82 ± 0.62
	Champion	23.38	1.14	0.74	19.57
1536	Average	23.38 ± 0.12	1.11 ± 0.03	0.75 ± 0.02	19.39 ± 0.32
	Champion	23.33	1.12	0.76	19.77
1752	Average	23.25 ± 0.30	1.12 ± 0.01	0.74 ± 0.02	19.25 ± 0.57
	Champion	23.46	1.13	0.76	20
2184	Average	23.37 ± 0.33	1.10 ± 0.02	0.72 ± 0.01	18.40 ± 0.33
	Champion	23.12	1.11	0.73	18.77
2664	Average	23.54 ± 0.23	1.12 ± 0.01	0.70 ± 0.02	18.41 ± 0.32
	Champion	23.65	1.11	0.72	18.94
3216	Average	23.41 ± 0.19	1.13 ± 0.01	0.71 ± 0.01	18.61 ± 0.23
	Champion	23.28	1.12	0.71	18.50
3552	Average	23.43 ± 0.30	1.13 ± 0.01	0.73 ± 0.01	19.30 ± 0.27
	Champion	23.55	1.12	0.74	19.40
3864	Average	23.25 ± 0.36	1.12 ± 0.02	0.71 ± 0.02	18.53 ± 0.28
	Champion	23.68	1.11	0.71	18.56
4200	Average	22.66 ± 0.71	1.12 ± 0.02	0.71 ± 0.01	18.04 ± 0.36
	Champion	23.13	1.11	0.73	18.54
4368	Average	23.13 ± 0.31	1.10 ± 0.02	0.70 ± 0.01	17.62 ± 0.26
	Champion	22.93	1.11	0.71	18.04

Table 7.14: Summarized photovoltaic parameters of the long-term stability performance of the most stable device based on ITO/SnO_2/perovskite doped with $Pyr_{14}BF_4$/Spiro-OMeTAD/Au. Adopted with permission from Ref [175]. Copyright © 2023 Elsevier.

The average PCE of the control devices decreased rapidly over the first few hundred hours, and then slowly decreased in the subsequent aging period. After aging for six months, the final average PCE (13.21 %) decreased to 75 % of the initial PCE value (17.60 %). In contrast, I observed an increase in the average PCE of $Pyr_{14}BF_4$–containing devices during the first 1752 h of aging, after which it remained essentially constant.

The final average PCE (17.62 %) maintained 97 % of the initial PCE value (18.13 %) after 6 months. Figure 7.23f shown the PCE evolution of non-encapsulated champion devices based on *J-V* characteristics as a function of aging time. Distinct from the control device that experienced a significant PCE decrease at the onset of aging, the $Pyr_{14}BF_4$–containing champion device remained above the initial value after aging for 4200 h in ambient conditions, with the maximum PCE reaching up to 20 % (Table 7.14). In the subsequent 100 h of aging, the device performance undergo a slight decrease, with the final PCE retaining approximately 97.3 % of the initial performance (PCE of 18.04 % after aging, compared to 18.54 % before aging). Moreover, no visible discoloration was observed for the $Pyr_{14}BF_4$–containing device (insets in Figure 7.23f).

7.7 Mechanisms of ionic liquid in film and device

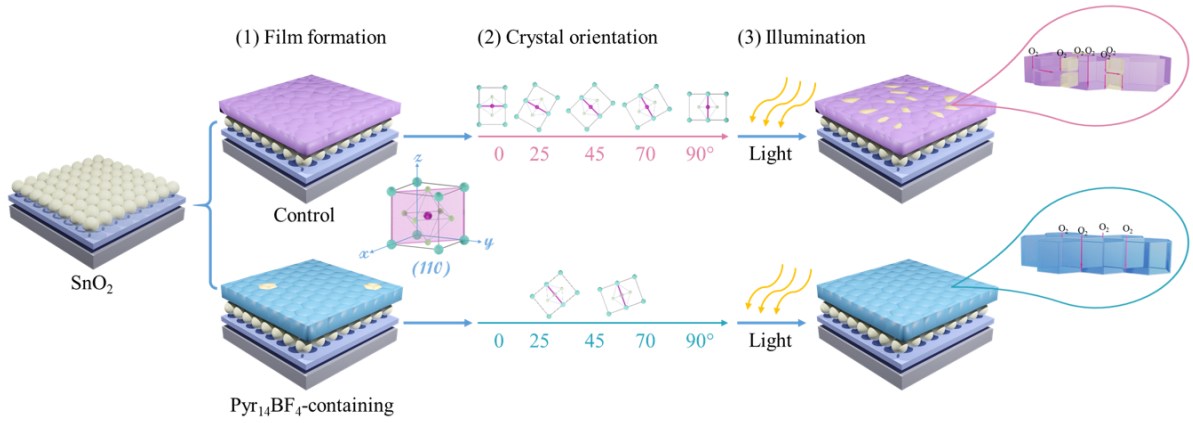

Figure 7.24: Schematic diagram of the working principle of $Pyr_{14}BF_4$ in perovskite solar cells. Adopted with permission from Ref [175]. Copyright © 2023 Elsevier.

To understand the underlying mechanisms by which ionic liquids enhance the photovoltaic performance and long-term operational stability of PSCs, I presented several possible insights as illustrated schematically in Figure 7.24. First is the formation of homogeneous and larger grain perovskite films (Figure 7.24 (1)). The introduction of ionic liquids in the film formation process promoted the uniform distribution of nucleation sites on the substrates and reduced the crystallization rate, which facilitated the synchronous and uniform growth of perovskite crystals. Such homogeneous and large-grained films dramatically reduced the number of grain boundaries and their associated defects, which served as photocarrier trap sites and chemically susceptible points for reactions with moisture

and oxygen. Indeed, the generation of large crystallites lowered the yield of superoxide species (O_2^-) and increased the diffusion lengths required for oxygen to reach the interiors of grains, thereby slowing the degradation of the perovskite films and devices over long time-scales. Second, along with affecting the grain morphology, the addition of ionic liquids during synthesis induced a transition from random to preferentially oriented perovskite grains within thin films (Figure 7.24 (2)). In particular, the induced preferential corner-up crystallographic orientation lowered the energy barrier for intergrain electronic transport, improved charge carrier mobility and decreased the probability of carrier trapping at defects, resulting in high photocurrent and photovoltage. [20, 156] Third, improved charge carrier transport and associated beneficial photo-carrier dynamics leaded to high PCE and improved long-term durability of PSCs. Degradation of the perovskite component can be triggered by the reaction of photo-generated electrons and oxygen under continuous illumination. The enhanced charge transport identified in $Pyr_{14}BF_4$–containing devices decreased the probability of electron transfer to oxygen by shortening the residence time of charge carriers in the active layer. In particular, the high charge carrier mobility and extended charge carrier lifetime promoted timely charge carrier extraction by ETL, thereby reducing carrier accumulation and interface recombination. The rapid extraction of photo-generated electrons from the photoactive layer suppressed the reaction with oxygen to form superoxide species (O_2^-), facilitating an improved device performance and operational stability of the PSCs under ambient conditions. In addition to kinetically stabilizing the perovskite films, the presence of ionic liquid improved the photo-stability of PSCs by suppressing light-induced fracturing of the perovskite film (Figure 7.24 (3)). In the absence of ionic liquid, light-induced grain fracturing leaded to an increase in the number of small crystallites, thereby generating additional grain boundaries that acted as sites for both chemical attack and photocarrier recombination. As a consequence of this photo-instability, the stability of PSCs was substantially compromised over a long time. In stark contrast, the $Pyr_{14}BF_4$–containing films were stabilized against light-induced grain fracturing and the generation of large crystallites leaded to sluggish oxygen diffusion kinetics, thereby inhibiting the light- and oxygen-induced degradation rates.

7.8 Summary

In summary, I demonstrated the crucial role of ionic liquids ($Pyr_{14}BF_4$, $BMIMBF_4$ and EMIMOTf) as effective additives in tailoring crystal orientation, minimizing detrimental defects, and forming large-sized crystals and uniform perovskite films. Furthermore, I found that the use of ionic liquid $Pyr_{14}BF_4$ inhibited the formation of the yellow δ-

$FAPbI_3$ phase, facilitated charge carrier transport and extraction, and extended charge carrier lifetimes in the active layer. These superior characteristics enable a champion PCE of 21.34 % for $Pyr_{14}BF_4$–containing PSCs with excellent reproducibility and long-term operational stability. Our approach represented a simple, broad application strategy for the fabrication of PSCs with excellent photovoltaic performance and long-term operational stability.

8 Conclusion and outlook

In this thesis, the effects of several functional ligands on the crystallization behavior during the formation of perovskite thin films and the photovoltaic performance and stability of the resulting device are investigated. GIWAXS as an essential characterization method is adopted to track the effects of additives on the crystal structure and crystal orientation of perovskite films from a microscopic perspective, and GISAXS is used to observe the microscopic changes in the perovskite morphology of the PSCs under operating conditions. In addition, PL, TRPL, TAS, TPV, TPC are also used to characterize the effects of additives on charge carrier dynamics within films and devices, respectively. Such as charge carrier recombination, transport, and extraction behaviors. Moreover, the long-term operational stability of the device, as the main challenge for the commercial application of perovskite solar cells, is also tracked as a focus in this thesis.

In the first part of the thesis, an anionic surfactant, sodium dodecylbenzene sulfonate (SDBS), is used to prepare high-quality PSCs based on MAPI perovskite component with excellent ambient stability. The SDBS is dissolved in isopropanol solvent and spin-coated on perovskite film to modify the perovskite interface. The experiment results show the SDBS located at grain boundaries and surface of the active layer can effectively passivate un-coordinated lead ions, tune the crystal orientation and improve the resistance of perovskite to moisture. Benefiting from these excellent properties, the SDBS passivated MAPI devices achieve a champion power conversion efficiency of 19.42 % with an V_{OC} of 1.12 V, a J_{SC} of 23.23 mA cm^{-2}, and a FF of 74 %. Moreover, the SDBS passivated devices also show a superior moisture stability. After storage in ambient conditions for 2000 hour, the SDBS passivated devices still remain 80 % of their initial average PCE based on 4 solar cells.

In the second part of the thesis, CsBr is introduced into the perovskite precursor solution to construct mixed-cation perovskite phases to reveal the effect of crystal orientation distribution on the optoelectronic behavior of the resulting perovskite films and PSCs. The GIWAXS measurement is used to detect the crystallographic properties of mixed perovskite films at the microscopic scale and shown that CsBr doping could change the stacking pattern of the crystals and promote a self-optimization of the crystal orientation

distribution. TRPL and SCLC measurement results show that the introduction of CsBr could passivat the trap-state densities and inhibit the generation of the non-radiative recombination sites. TPC and TPV measurement results show that the photo-generated charge carrier transport and extraction properties are also facilitated after CsBr incorporation. The improvements in the structure and optoelectronic behavior result in an enhanced V_{OC} and superior photovoltaic efficiency of the corresponding PSCs. The best performing devices based on 3 % CsBr achieve a champion PCE of 19.24 % compared with the reference device with 17.82 %.

In the third part of the thesis, a pyrrolidinium-based ionic compound ($Pyr_{14}BF_4$) is introduced into the perovskite precursor solution to investigate the impact of ionic liquids on the crystal growth of perovskite films. Using time-resolved measurements, such as PL, TRPL, TAS, TPC, and TPV, the charge generation, transport, recombination, and extraction behavior in perovskite films and corresponded devices are investigated. The characterization results show that the incorporation of ionic compound $Pyr_{14}BF_4$ could inhibit charge carrier recombination and accelerate electron transport and extraction. Moreover, the GIWAXS result of perovskite films based on different ionic liquids incorporation show that ionic liquids can tailor the crystal growth from a disordered to a preferential corner-up orientation during film formation. Additionally, the operando grazing-incidence small- and wide-angle X-ray scattering measurements of PSCs indicate that the reference devices exhibit light-induced lattice compression and grain fragmentation. Whereas the ionic liquid-containing devices only exhibit a slight light-induced crystal reconstitution as well as stronger tolerance against illumination. Under ambient conditions, the non-encapsulated $Pyr_{14}BF_4$-containing device retain 97 % of its initial efficiency after 4368 h.

Based on the experiments executed in the present thesis, further related investigations can be envisioned. In this thesis, three functional ligands are used to study their passivation effects on defects existing in film bulk, grain boundaries and interfaces, and also to explore the impact on the resulting device performance and long-term stability. Because most of the above data are based the experimental results, much time could be take up. Therefore, in the later experiment design, theoretical calculations could be introduced and combine with experiments. Through density functional theory calculation and molecular dynamics simulations to analysis problems such as defects, energy levels, and intermolecular interactions. On the one hand, theoretical calculations could be used for pre-screening to select the best functional ligands for performance optimization. On the other hand, it helps us to gain an in-depth understanding on the role of functional ligands in perovskite, especially intermolecular interactions. In addition, the stability of perovskite solar cells is closely related to future commercial applications. Tracking the composition and crystal

structure of perovskite under heat, oxygen, UV and humidity conditions, which is helpful for the in-depth understanding of the degradation mechanism and provide new insights into the structural optimization and encapsulation of devices.

Bibliography

[1] P. G. P. D. PE, *Sustainable energy systems engineering: the complete green building design resource*. McGraw-Hill Education, 2007.

[2] D. M. Chapin, C. S. Fuller, and G. L. Pearson, "A new silicon p-n junction photocell for converting solar radiation into electrical power," *Journal of Applied Physics*, vol. 25, no. 5, pp. 676–677, 1954.

[3] K. Yoshikawa, H. Kawasaki, W. Yoshida, T. Irie, K. Konishi, K. Nakano, T. Uto, D. Adachi, M. Kanematsu, H. Uzu, *et al.*, "Silicon heterojunction solar cell with interdigitated back contacts for a photoconversion efficiency over 26%," *Nature Energy*, vol. 2, no. 5, pp. 1–8, 2017.

[4] M. Green, E. Dunlop, J. Hohl-Ebinger, M. Yoshita, N. Kopidakis, and X. Hao, "Solar cell efficiency tables (version 57)," *Progress in Photovoltaics: Research and Applications*, vol. 29, no. 1, pp. 3–15, 2021.

[5] L. M. Fraas and L. D. Partain, *Solar cells and their applications*, vol. 217. Wiley Hoboken, NJ, 2010.

[6] L. Fraas, J. Avery, V. Sundaram, V. Kinh, T. Davenport, J. Yerkes, J. Gee, and K. Emery, "Over 35% efficient gaas/gasb stacked concentrator cell assemblies for terrestrial applications," pp. 190–195, 1990.

[7] L. Fraas and R. Knechtli, "Design of high efficiency monolithic stacked multijunction solar cells," in *13th Photovoltaic Specialists Conference*, pp. 886–891, 1978.

[8] M. Kim, J. Jeong, H. Lu, T. K. Lee, F. T. Eickemeyer, Y. Liu, I. W. Choi, S. J. Choi, Y. Jo, H.-B. Kim, *et al.*, "Conformal quantum dot–sno2 layers as electron transporters for efficient perovskite solar cells," *Science*, vol. 375, no. 6578, pp. 302–306, 2022.

[9] J.-H. Im, C.-R. Lee, J.-W. Lee, S.-W. Park, and N.-G. Park, "6.5% efficient perovskite quantum-dot-sensitized solar cell," *Nanoscale*, vol. 3, no. 10, pp. 4088–4093, 2011.

[10] H.-S. Kim, C.-R. Lee, J.-H. Im, K.-B. Lee, T. Moehl, A. Marchioro, S.-J. Moon, R. Humphry-Baker, J.-H. Yum, J. E. Moser, *et al.*, "Lead iodide perovskite sensitized all-solid-state submicron thin film mesoscopic solar cell with efficiency exceeding 9%," *Scientific Reports*, vol. 2, no. 1, pp. 1–7, 2012.

[11] J. Burschka, N. Pellet, S.-J. Moon, R. Humphry-Baker, P. Gao, M. K. Nazeeruddin, and M. Grätzel, "Sequential deposition as a route to high-performance perovskite-sensitized solar cells," *Nature*, vol. 499, no. 7458, pp. 316–319, 2013.

[12] H. Zhou, Q. Chen, G. Li, S. Luo, T.-b. Song, H.-S. Duan, Z. Hong, J. You, Y. Liu, and Y. Yang, "Interface engineering of highly efficient perovskite solar cells," *Science*, vol. 345, no. 6196, pp. 542–546, 2014.

[13] W. S. Yang, B.-W. Park, E. H. Jung, N. J. Jeon, Y. C. Kim, D. U. Lee, S. S. Shin, J. Seo, E. K. Kim, J. H. Noh, *et al.*, "Iodide management in formamidinium-lead-halide–based perovskite layers for efficient solar cells," *Science*, vol. 356, no. 6345, pp. 1376–1379, 2017.

[14] Y. Kato, L. K. Ono, M. V. Lee, S. Wang, S. R. Raga, and Y. Qi, "Silver iodide formation in methyl ammonium lead iodide perovskite solar cells with silver top electrodes," *Advanced Materials Interfaces*, vol. 2, no. 13, p. 1500195, 2015.

[15] C. Eames, J. M. Frost, P. R. Barnes, B. C. O'regan, A. Walsh, and M. S. Islam, "Ionic transport in hybrid lead iodide perovskite solar cells," *Nature Communications*, vol. 6, no. 1, pp. 1–8, 2015.

[16] E. Bi, H. Chen, F. Xie, Y. Wu, W. Chen, Y. Su, A. Islam, M. Grätzel, X. Yang, and L. Han, "Diffusion engineering of ions and charge carriers for stable efficient perovskite solar cells," *Nature Communications*, vol. 8, no. 1, pp. 1–7, 2017.

[17] W. Shockley and H. J. Queisser, "Detailed balance limit of efficiency of p-n junction solar cells," *Journal of Applied Physics*, vol. 32, no. 3, pp. 510–519, 1961.

[18] S. Ghosh and T. Singh, "Role of ionic liquids in organic-inorganic metal halide perovskite solar cells efficiency and stability," *Nano Energy*, vol. 63, p. 103828, 2019.

[19] S. Bai, P. Da, C. Li, Z. Wang, Z. Yuan, F. Fu, M. Kawecki, X. Liu, N. Sakai, J. T.-W. Wang, *et al.*, "Planar perovskite solar cells with long-term stability using ionic liquid additives," *Nature*, vol. 571, no. 7764, pp. 245–250, 2019.

[20] G. Zheng, C. Zhu, J. Ma, X. Zhang, G. Tang, R. Li, Y. Chen, L. Li, J. Hu, J. Hong, *et al.*, "Manipulation of facet orientation in hybrid perovskite polycrystalline films by cation cascade," *Nature Communications*, vol. 9, no. 1, pp. 1–11, 2018.

[21] C. Li, X. Lu, W. Ding, L. Feng, Y. Gao, and Z. Guo, "Formability of abx3 (x= f, cl, br, i) halide perovskites," *Acta Crystallographica Section B: Structural Science*, vol. 64, no. 6, pp. 702–707, 2008.

[22] T. Baikie, Y. Fang, J. M. Kadro, M. Schreyer, F. Wei, S. G. Mhaisalkar, M. Graetzel, and T. J. White, "Synthesis and crystal chemistry of the hybrid perovskite (ch 3 nh 3) pbi 3 for solid-state sensitised solar cell applications," *Journal of Materials Chemistry A*, vol. 1, no. 18, pp. 5628–5641, 2013.

[23] C. C. Stoumpos, C. D. Malliakas, and M. G. Kanatzidis, "Semiconducting tin and lead iodide perovskites with organic cations: phase transitions, high mobilities, and near-infrared photoluminescent properties," *Inorganic Chemistry*, vol. 52, no. 15, pp. 9019–9038, 2013.

[24] M. Green, "a.; ho-baillie, a.; snaith, hj the emergence of perovskite solar cells," *Nat. Photonics*, vol. 8, pp. 506–514, 2014.

[25] T. A. Berhe, W.-N. Su, C.-H. Chen, C.-J. Pan, J.-H. Cheng, H.-M. Chen, M.-C. Tsai, L.-Y. Chen, A. A. Dubale, and B.-J. Hwang, "Organometal halide perovskite solar cells: degradation and stability," *Energy & Environmental Science*, vol. 9, no. 2, pp. 323–356, 2016.

[26] K. Seeger, *Semiconductor physics*. Springer Science & Business Media, 2013.

[27] D. A. Neamen, *Semiconductor physics and devices: basic principles*. McGraw-hill, 2003.

[28] L. M. Herz *et al.*, "Charge-carrier dynamics in organic-inorganic metal halide perovskites," *Annu. Rev. Phys. Chem*, vol. 67, no. 1, pp. 65–89, 2016.

[29] G.-J. A. Wetzelaer, M. Scheepers, A. M. Sempere, C. Momblona, J. Ávila, and H. J. Bolink, "Trap-assisted non-radiative recombination in organic–inorganic perovskite solar cells," *Advanced Materials*, vol. 27, no. 11, pp. 1837–1841, 2015.

[30] W.-J. Yin, T. Shi, and Y. Yan, "Unique properties of halide perovskites as possible origins of the superior solar cell performance," *Advanced Materials*, vol. 26, no. 27, pp. 4653–4658, 2014.

[31] M. B. Johnston and L. M. Herz, "Hybrid perovskites for photovoltaics: charge-carrier recombination, diffusion, and radiative efficiencies," *Accounts of Chemical Research*, vol. 49, no. 1, pp. 146–154, 2016.

[32] S. D. Stranks, V. M. Burlakov, T. Leijtens, J. M. Ball, A. Goriely, and H. J. Snaith, "Recombination kinetics in organic-inorganic perovskites: excitons, free charge, and subgap states," *Physical Review Applied*, vol. 2, no. 3, p. 034007, 2014.

[33] T. S. Sherkar, C. Momblona, L. Gil-Escrig, J. Avila, M. Sessolo, H. J. Bolink, and L. J. A. Koster, "Recombination in perovskite solar cells: significance of grain boundaries, interface traps, and defect ions," *ACS Energy Letters*, vol. 2, no. 5, pp. 1214–1222, 2017.

[34] Y. Yuan and J. Huang, "Ion migration in organometal trihalide perovskite and its impact on photovoltaic efficiency and stability," *Accounts of Chemical Research*, vol. 49, no. 2, pp. 286–293, 2016.

[35] D. B. Mitzi, "Templating and structural engineering in organic–inorganic perovskites," *Journal of the Chemical Society, Dalton Transactions*, no. 1, pp. 1–12, 2001.

[36] B. Conings, J. Drijkoningen, N. Gauquelin, A. Babayigit, J. D'Haen, L. D'Olieslaeger, A. Ethirajan, J. Verbeeck, J. Manca, E. Mosconi, *et al.*, "Intrinsic thermal instability of methylammonium lead trihalide perovskite," *Advanced Energy Materials*, vol. 5, no. 15, p. 1500477, 2015.

[37] D. Trots and S. Myagkota, "High-temperature structural evolution of caesium and rubidium triiodoplumbates," *Journal of Physics and Chemistry of Solids*, vol. 69, no. 10, pp. 2520–2526, 2008.

[38] G. E. Eperon, S. D. Stranks, C. Menelaou, M. B. Johnston, L. M. Herz, and H. J. Snaith, "Formamidinium lead trihalide: a broadly tunable perovskite for efficient planar heterojunction solar cells," *Energy & Environmental Science*, vol. 7, no. 3, pp. 982–988, 2014.

[39] F. C. Hanusch, E. Wiesenmayer, E. Mankel, A. Binek, P. Angloher, C. Fraunhofer, N. Giesbrecht, J. M. Feckl, W. Jaegermann, D. Johrendt, *et al.*, "Efficient planar heterojunction perovskite solar cells based on formamidinium lead bromide," *The Journal of Physical Chemistry Letters*, vol. 5, no. 16, pp. 2791–2795, 2014.

[40] W. Li, J. Li, L. Wang, G. Niu, R. Gao, and Y. Qiu, "Post modification of perovskite sensitized solar cells by aluminum oxide for enhanced performance," *Journal of Materials Chemistry A*, vol. 1, no. 38, pp. 11735–11740, 2013.

[41] G. Niu, W. Li, F. Meng, L. Wang, H. Dong, and Y. Qiu, "Study on the stability of ch 3 nh 3 pbi 3 films and the effect of post-modification by aluminum oxide in all-solid-state hybrid solar cells," *Journal of Materials Chemistry A*, vol. 2, no. 3, pp. 705–710, 2014.

[42] L. N. Quan, M. Yuan, R. Comin, O. Voznyy, E. M. Beauregard, S. Hoogland, A. Buin, A. R. Kirmani, K. Zhao, A. Amassian, *et al.*, "Ligand-stabilized reduced-dimensionality perovskites," *Journal of the American Chemical Society*, vol. 138, no. 8, pp. 2649–2655, 2016.

[43] D. H. Cao, C. C. Stoumpos, O. K. Farha, J. T. Hupp, and M. G. Kanatzidis, "2d homologous perovskites as light-absorbing materials for solar cell applications," *Journal of the American Chemical Society*, vol. 137, no. 24, pp. 7843–7850, 2015.

[44] Q. Jiang, Y. Zhao, X. Zhang, X. Yang, Y. Chen, Z. Chu, Q. Ye, X. Li, Z. Yin, and J. You, "Surface passivation of perovskite film for efficient solar cells," *Nature Photonics*, vol. 13, no. 7, pp. 460–466, 2019.

[45] T. M. Koh, K. Fu, Y. Fang, S. Chen, T. C. Sum, N. Mathews, S. G. Mhaisalkar, P. P. Boix, and T. Baikie, "Formamidinium-containing metal-halide: an alternative material for near-ir absorption perovskite solar cells," *The Journal of Physical Chemistry C*, vol. 118, no. 30, pp. 16458–16462, 2014.

[46] A. Binek, F. C. Hanusch, P. Docampo, and T. Bein, "Stabilization of the trigonal high-temperature phase of formamidinium lead iodide," *The Journal of Physical Chemistry Letters*, vol. 6, no. 7, pp. 1249–1253, 2015.

[47] J.-W. Lee, D.-H. Kim, H.-S. Kim, S.-W. Seo, S. M. Cho, and N.-G. Park, "Formamidinium and cesium hybridization for photo-and moisture-stable perovskite solar cell," *Advanced Energy Materials*, vol. 5, no. 20, p. 1501310, 2015.

[48] N. Kitazawa, Y. Watanabe, and Y. Nakamura, "Optical properties of ch3nh3pbx3 (x= halogen) and their mixed-halide crystals," *Journal of Materials Science*, vol. 37, no. 17, pp. 3585–3587, 2002.

[49] L.-y. Huang and W. R. Lambrecht, "Electronic band structure, phonons, and exciton binding energies of halide perovskites cssncl 3, cssnbr 3, and cssni 3," *Physical Review B*, vol. 88, no. 16, p. 165203, 2013.

[50] S. D. Stranks, G. E. Eperon, G. Grancini, C. Menelaou, M. J. Alcocer, T. Leijtens, L. M. Herz, A. Petrozza, and H. J. Snaith, "Electron-hole diffusion lengths exceeding 1 micrometer in an organometal trihalide perovskite absorber," *Science*, vol. 342, no. 6156, pp. 341–344, 2013.

[51] P. Müller-Buschbaum, "The active layer morphology of organic solar cells probed with grazing incidence scattering techniques," *Advanced Materials*, vol. 26, no. 46, pp. 7692–7709, 2014.

[52] R. Lazzari, F. Leroy, and G. Renaud, "Grazing-incidence small-angle x-ray scattering from dense packing of islands on surfaces: Development of distorted wave born approximation and correlation between particle sizes and spacing," *Physical Review B*, vol. 76, no. 12, p. 125411, 2007.

[53] P. Müller-Buschbaum, "A basic introduction to grazing incidence small-angle x-ray scattering," in *Applications of Synchrotron Light to Scattering and Diffraction in Materials and Life Sciences*, pp. 61–89, Springer, 2009.

[54] C. Revenant, F. Leroy, G. Renaud, R. Lazzari, A. Létoublon, and T. Madey, "Structural and morphological evolution of co on faceted pt/w (1 1 1) surface upon thermal annealing," *Surface Science*, vol. 601, no. 16, pp. 3431–3449, 2007.

[55] R. Hosemann, W. Vogel, D. Weick, and F. Balta-Calleja, "Novel aspects of the real paracrystal," *Acta Crystallographica Section A: Crystal Physics, Diffraction, Theoretical and General Crystallography*, vol. 37, no. 1, pp. 85–91, 1981.

[56] Z. Jiang, "Gixsgui: a matlab toolbox for grazing-incidence x-ray scattering data visualization and reduction, and indexing of buried three-dimensional periodic nanostructured films," *Journal of Applied Crystallography*, vol. 48, no. 3, pp. 917–926, 2015.

[57] J. L. Baker, L. H. Jimison, S. Mannsfeld, S. Volkman, S. Yin, V. Subramanian, A. Salleo, A. P. Alivisatos, and M. F. Toney, "Quantification of thin film crystallographic orientation using x-ray diffraction with an area detector," *Langmuir*, vol. 26, no. 11, pp. 9146–9151, 2010.

[58] J. Schlipf, *The Morphology of Hybrid Perovskite Thin Films for Photovoltaic Application*. PhD thesis, Technische Universität München, 2018.

[59] A. Ikai, "Stm and afm of bio/organic molecules and structures," *Surface Science Reports*, vol. 26, no. 8, pp. 261–332, 1996.

[60] Q. Zhong, D. Inniss, K. Kjoller, and V. Elings, "Fractured polymer/silica fiber surface studied by tapping mode atomic force microscopy," *Surface Science Letters*, vol. 290, no. 1-2, pp. L688–L692, 1993.

[61] T. G. Mayerhöfer, H. Mutschke, and J. Popp, "Employing theories far beyond their limits—the case of the (boguer-) beer–lambert law," *ChemPhysChem*, vol. 17, no. 13, pp. 1948–1955, 2016.

[62] H. Fujiwara, *Spectroscopic ellipsometry: principles and applications*. John Wiley & Sons, 2007.

[63] X. Jiang, F. Wang, Q. Wei, H. Li, Y. Shang, W. Zhou, C. Wang, P. Cheng, Q. Chen, L. Chen, *et al.*, "Ultra-high open-circuit voltage of tin perovskite solar cells via an electron transporting layer design," *Nature Communications*, vol. 11, no. 1, pp. 1–7, 2020.

[64] J. R. Lakowicz, *Principles of fluorescence spectroscopy*. Springer, 2006.

[65] J. Bisquert, D. Cahen, G. Hodes, S. Rühle, and A. Zaban, "Physical chemical principles of photovoltaic conversion with nanoparticulate, mesoporous dye-sensitized solar cells," *The Journal of Physical Chemistry B*, vol. 108, no. 24, pp. 8106–8118, 2004.

[66] A. Luque, A. Martí, and C. Stanley, "Understanding intermediate-band solar cells," *Nature Photonics*, vol. 6, no. 3, pp. 146–152, 2012.

[67] A. Zaban, M. Greenshtein, and J. Bisquert, "Determination of the electron lifetime in nanocrystalline dye solar cells by open-circuit voltage decay measurements," *ChemPhysChem*, vol. 4, no. 8, pp. 859–864, 2003.

[68] J. Bisquert, F. Fabregat-Santiago, I. Mora-Sero, G. Garcia-Belmonte, and S. Gimenez, "Electron lifetime in dye-sensitized solar cells: theory and interpretation of measurements," *The Journal of Physical Chemistry C*, vol. 113, no. 40, pp. 17278–17290, 2009.

[69] L. Bertoluzzi, R. S. Sanchez, L. Liu, J.-W. Lee, E. Mas-Marza, H. Han, N.-G. Park, I. Mora-Sero, and J. Bisquert, "Cooperative kinetics of depolarization in ch 3 nh 3 pbi 3 perovskite solar cells," *Energy & Environmental Science*, vol. 8, no. 3, pp. 910–915, 2015.

[70] D. Shi, V. Adinolfi, R. Comin, M. Yuan, E. Alarousu, A. Buin, Y. Chen, S. Hoogland, A. Rothenberger, K. Katsiev, *et al.*, "Low trap-state density and long carrier diffusion in organolead trihalide perovskite single crystals," *Science*, vol. 347, no. 6221, pp. 519–522, 2015.

[71] Y. Liu, Z. Yang, D. Cui, X. Ren, J. Sun, X. Liu, J. Zhang, Q. Wei, H. Fan, F. Yu, *et al.*, "Two-inch-sized perovskite ch3nh3pbx3 (x= cl, br, i) crystals: growth and characterization," *Advanced Materials*, vol. 27, no. 35, pp. 5176–5183, 2015.

[72] L. Gao, K. Zeng, J. Guo, C. Ge, J. Du, Y. Zhao, C. Chen, H. Deng, Y. He, H. Song, *et al.*, "Passivated single-crystalline ch3nh3pbi3 nanowire photodetector with high detectivity and polarization sensitivity," *Nano Letters*, vol. 16, no. 12, pp. 7446–7454, 2016.

[73] M. I. Saidaminov, A. L. Abdelhady, B. Murali, E. Alarousu, V. M. Burlakov, W. Peng, I. Dursun, L. Wang, Y. He, G. Maculan, *et al.*, "High-quality bulk hybrid perovskite single crystals within minutes by inverse temperature crystallization," *Nature Communications*, vol. 6, no. 1, pp. 1–6, 2015.

[74] A. Buffet, A. Rothkirch, R. Döhrmann, V. Körstgens, M. M. Abul Kashem, J. Perlich, G. Herzog, M. Schwartzkopf, R. Gehrke, P. Müller-Buschbaum, *et al.*, "P03, the microfocus and nanofocus x-ray scattering (minaxs) beamline of the petra iii storage ring: the microfocus endstation," *Journal of Synchrotron Radiation*, vol. 19, no. 4, pp. 647–653, 2012.

[75] G. Benecke, W. Wagermaier, C. Li, M. Schwartzkopf, G. Flucke, R. Hoerth, I. Zizak, M. Burghammer, E. Metwalli, P. Müller-Buschbaum, *et al.*, "A customizable software for fast reduction and analysis of large x-ray scattering data sets: applications of the new dpdak package to small-angle x-ray scattering and grazing-incidence small-angle x-ray scattering," *Journal of Spplied Crystallography*, vol. 47, no. 5, pp. 1797–1803, 2014.

[76] P. Müller-Buschbaum, "Grazing incidence small-angle x-ray scattering: an advanced scattering technique for the investigation of nanostructured polymer films," *Analytical and Bioanalytical Chemistry*, vol. 376, no. 1, pp. 3–10, 2003.

[77] R. Lazzari, "Isgisaxs: a program for grazing-incidence small-angle x-ray scattering analysis of supported islands," *Journal of Applied Crystallography*, vol. 35, no. 4, pp. 406–421, 2002.

[78] Y. Zou, R. Guo, A. Buyruk, W. Chen, T. Xiao, S. Yin, X. Jiang, L. P. Kreuzer, C. Mu, T. Ameri, *et al.*, "Sodium dodecylbenzene sulfonate interface modification of methylammonium lead iodide for surface passivation of perovskite solar cells," *ACS Applied Materials & Interfaces*, vol. 12, no. 47, pp. 52643–52651, 2020.

[79] G. Grancini, S. Marras, M. Prato, C. Giannini, C. Quarti, F. De Angelis, M. De Bastiani, G. E. Eperon, H. J. Snaith, L. Manna, *et al.*, "The impact of the crystallization processes on the structural and optical properties of hybrid perovskite films for photovoltaics," *The Journal of Physical Chemistry Letters*, vol. 5, no. 21, pp. 3836–3842, 2014.

[80] J. M. Ball and A. Petrozza, "Defects in perovskite-halides and their effects in solar cells," *Nature Energy*, vol. 1, no. 11, pp. 1–13, 2016.

[81] W. Tress, N. Marinova, O. Inganäs, M. K. Nazeeruddin, S. M. Zakeeruddin, and M. Graetzel, "Predicting the open-circuit voltage of ch3nh3pbi3 perovskite solar cells using electroluminescence and photovoltaic quantum efficiency spectra: the role

of radiative and non-radiative recombination," *Advanced Energy Materials*, vol. 5, no. 3, p. 1400812, 2015.

[82] G. Xing, N. Mathews, S. Sun, S. S. Lim, Y. M. Lam, M. Grätzel, S. Mhaisalkar, and T. C. Sum, "Long-range balanced electron-and hole-transport lengths in organic-inorganic ch3nh3pbi3," *Science*, vol. 342, no. 6156, pp. 344–347, 2013.

[83] M. L. Petrus, J. Schlipf, C. Li, T. P. Gujar, N. Giesbrecht, P. Müller-Buschbaum, M. Thelakkat, T. Bein, S. Hüttner, and P. Docampo, "Capturing the sun: A review of the challenges and perspectives of perovskite solar cells," *Advanced Energy Materials*, vol. 7, no. 16, p. 1700264, 2017.

[84] J.-W. Lee, Z. Dai, T.-H. Han, C. Choi, S.-Y. Chang, S.-J. Lee, N. De Marco, H. Zhao, P. Sun, Y. Huang, *et al.*, "2d perovskite stabilized phase-pure formamidinium perovskite solar cells," *Nature Communications*, vol. 9, no. 1, pp. 1–10, 2018.

[85] Y. Liu, S. Akin, L. Pan, R. Uchida, N. Arora, J. V. Milić, A. Hinderhofer, F. Schreiber, A. R. Uhl, S. M. Zakeeruddin, *et al.*, "Ultrahydrophobic 3d/2d fluoroarene bilayer-based water-resistant perovskite solar cells with efficiencies exceeding 22%," *Science Advances*, vol. 5, no. 6, p. eaaw2543, 2019.

[86] T. Zhang, M. I. Dar, G. Li, F. Xu, N. Guo, M. Grätzel, and Y. Zhao, "Bication lead iodide 2d perovskite component to stabilize inorganic α-cspbi3 perovskite phase for high-efficiency solar cells," *Science Advances*, vol. 3, no. 9, p. e1700841, 2017.

[87] F. Zhang, Z. Yao, Y. Guo, Y. Li, J. Bergstrand, C. J. Brett, B. Cai, A. Hajian, Y. Guo, X. Yang, *et al.*, "Polymeric, cost-effective, dopant-free hole transport materials for efficient and stable perovskite solar cells," *Journal of the American Chemical Society*, vol. 141, no. 50, pp. 19700–19707, 2019.

[88] A. Kojima, K. Teshima, Y. Shirai, and T. Miyasaka, "Organometal halide perovskites as visible-light sensitizers for photovoltaic cells," *Journal of the American Chemical Society*, vol. 131, no. 17, pp. 6050–6051, 2009.

[89] B. Chen, S.-W. Baek, Y. Hou, E. Aydin, M. De Bastiani, B. Scheffel, A. Proppe, Z. Huang, M. Wei, Y.-K. Wang, *et al.*, "Enhanced optical path and electron diffusion length enable high-efficiency perovskite tandems," *Nature Communications*, vol. 11, no. 1, pp. 1–9, 2020.

[90] Y. Rong, Y. Hu, A. Mei, H. Tan, M. I. Saidaminov, S. I. Seok, M. D. McGehee, E. H. Sargent, and H. Han, "Challenges for commercializing perovskite solar cells," *Science*, vol. 361, no. 6408, p. eaat8235, 2018.

[91] T. Leijtens, G. E. Eperon, N. K. Noel, S. N. Habisreutinger, A. Petrozza, and H. J. Snaith, "Stability of metal halide perovskite solar cells," *Advanced Energy Materials*, vol. 5, no. 20, p. 1500963, 2015.

[92] M. M. Lee, J. Teuscher, T. Miyasaka, T. N. Murakami, and H. J. Snaith, "Efficient hybrid solar cells based on meso-superstructured organometal halide perovskites," *Science*, vol. 338, no. 6107, pp. 643–647, 2012.

[93] N.-G. Park, M. Grätzel, T. Miyasaka, K. Zhu, and K. Emery, "Towards stable and commercially available perovskite solar cells," *Nature Energy*, vol. 1, no. 11, pp. 1–8, 2016.

[94] X. Zheng, B. Chen, J. Dai, Y. Fang, Y. Bai, Y. Lin, H. Wei, X. C. Zeng, and J. Huang, "Defect passivation in hybrid perovskite solar cells using quaternary ammonium halide anions and cations," *Nature Energy*, vol. 2, no. 7, pp. 1–9, 2017.

[95] M. A. Green, A. Ho-Baillie, and H. J. Snaith, "The emergence of perovskite solar cells," *Nature Photonics*, vol. 8, no. 7, pp. 506–514, 2014.

[96] M. Saliba, T. Matsui, J.-Y. Seo, K. Domanski, J.-P. Correa-Baena, M. K. Nazeeruddin, S. M. Zakeeruddin, W. Tress, A. Abate, A. Hagfeldt, *et al.*, "Cesium-containing triple cation perovskite solar cells: improved stability, reproducibility and high efficiency," *Energy & Environmental Science*, vol. 9, no. 6, pp. 1989–1997, 2016.

[97] S. Tang, Y. Deng, X. Zheng, Y. Bai, Y. Fang, Q. Dong, H. Wei, and J. Huang, "Composition engineering in doctor-blading of perovskite solar cells," *Advanced Energy Materials*, vol. 7, no. 18, p. 1700302, 2017.

[98] G. Grancini, C. Roldán-Carmona, I. Zimmermann, E. Mosconi, X. Lee, D. Martineau, S. Narbey, F. Oswald, F. De Angelis, M. Graetzel, *et al.*, "One-year stable perovskite solar cells by 2d/3d interface engineering," *Nature Communications*, vol. 8, no. 1, pp. 1–8, 2017.

[99] M.-H. Li, H.-H. Yeh, Y.-H. Chiang, U.-S. Jeng, C.-J. Su, H.-W. Shiu, Y.-J. Hsu, N. Kosugi, T. Ohigashi, Y.-A. Chen, *et al.*, "Highly efficient 2d/3d hybrid perovskite solar cells via low-pressure vapor-assisted solution process," *Advanced Materials*, vol. 30, no. 30, p. 1801401, 2018.

[100] Y. Zou, Y. Cui, H.-Y. Wang, Q. Cai, C. Mu, and J.-P. Zhang, "Highly efficient and stable 2d–3d perovskite solar cells fabricated by interfacial modification," *Nanotechnology*, vol. 30, no. 27, p. 275202, 2019.

[101] S. Yang, Y. Wang, P. Liu, Y.-B. Cheng, H. J. Zhao, and H. G. Yang, "Functionalization of perovskite thin films with moisture-tolerant molecules," *Nature Energy*, vol. 1, no. 2, pp. 1–7, 2016.

[102] Y. Zou, Y. Liang, C. Mu, and J.-P. Zhang, "Enhancement of open-circuit voltage of perovskite solar cells by interfacial modification with p-aminobenzoic acid," *Advanced Materials Interfaces*, vol. 7, no. 1, p. 1901584, 2020.

[103] Y. Zou, H.-Y. Wang, Y. Qin, C. Mu, Q. Li, D. Xu, and J.-P. Zhang, "Reduced defects of mapbi3 thin films treated by fai for high-performance planar perovskite solar cells," *Advanced Functional Materials*, vol. 29, no. 7, p. 1805810, 2019.

[104] Y. Fu, T. Wu, J. Wang, J. Zhai, M. J. Shearer, Y. Zhao, R. J. Hamers, E. Kan, K. Deng, X.-Y. Zhu, *et al.*, "Stabilization of the metastable lead iodide perovskite phase via surface functionalization," *Nano Letters*, vol. 17, no. 7, pp. 4405–4414, 2017.

[105] J.-C. Blancon, H. Tsai, W. Nie, C. C. Stoumpos, L. Pedesseau, C. Katan, M. Kepenekian, C. M. M. Soe, K. Appavoo, M. Y. Sfeir, *et al.*, "Extremely efficient internal exciton dissociation through edge states in layered 2d perovskites," *Science*, vol. 355, no. 6331, pp. 1288–1292, 2017.

[106] Y. Lin, Y. Bai, Y. Fang, Q. Wang, Y. Deng, and J. Huang, "Suppressed ion migration in low-dimensional perovskites," *ACS Energy Letters*, vol. 2, no. 7, pp. 1571–1572, 2017.

[107] R. Wang, J. Xue, L. Meng, J.-W. Lee, Z. Zhao, P. Sun, L. Cai, T. Huang, Z. Wang, Z.-K. Wang, *et al.*, "Caffeine improves the performance and thermal stability of perovskite solar cells," *Joule*, vol. 3, no. 6, pp. 1464–1477, 2019.

[108] X. Zheng, Y. Deng, B. Chen, H. Wei, X. Xiao, Y. Fang, Y. Lin, Z. Yu, Y. Liu, Q. Wang, *et al.*, "Dual functions of crystallization control and defect passivation enabled by sulfonic zwitterions for stable and efficient perovskite solar cells," *Advanced Materials*, vol. 30, no. 52, p. 1803428, 2018.

[109] M. V. Khenkin, E. A. Katz, A. Abate, G. Bardizza, J. J. Berry, C. Brabec, F. Brunetti, V. Bulović, Q. Burlingame, A. Di Carlo, *et al.*, "Consensus statement for stability assessment and reporting for perovskite photovoltaics based on isos procedures," *Nature Energy*, vol. 5, no. 1, pp. 35–49, 2020.

[110] N. J. Jeon, J. H. Noh, Y. C. Kim, W. S. Yang, S. Ryu, and S. I. Seok, "Solvent engineering for high-performance inorganic–organic hybrid perovskite solar cells," *Nature Materials*, vol. 13, no. 9, pp. 897–903, 2014.

[111] W. S. Yang, J. H. Noh, N. J. Jeon, Y. C. Kim, S. Ryu, J. Seo, and S. I. Seok, "High-performance photovoltaic perovskite layers fabricated through intramolecular exchange," *Science*, vol. 348, no. 6240, pp. 1234–1237, 2015.

[112] D. Muller, M. Malmsten, B. Bergenståhl, J. Hessing, J. Olijve, and F. Mori, "Competitive adsorption of gelatin and sodium dodecylbenzenesulfonate at hydrophobic surfaces," *Langmuir*, vol. 14, no. 11, pp. 3107–3114, 1998.

[113] H. Fan, H. Wang, J. Guo, N. Zhao, and J. Xu, "Sdbs-assisted preparation of novel polyaniline planar-structure: Morphology, mechanism and hydrophobicity," *Journal of Colloid and Interface Science*, vol. 414, pp. 46–49, 2014.

[114] H. Zhu, Y. Liu, F. T. Eickemeyer, L. Pan, D. Ren, M. A. Ruiz-Preciado, B. Carlsen, B. Yang, X. Dong, Z. Wang, *et al.*, "Tailored amphiphilic molecular mitigators for stable perovskite solar cells with 23.5% efficiency," *Advanced Materials*, vol. 32, no. 12, p. 1907757, 2020.

[115] J. Schlipf, L. Bießmann, L. Oesinghaus, E. Berger, E. Metwalli, J. A. Lercher, L. Porcar, and P. Muller-Buschbaum, "In situ monitoring the uptake of moisture into hybrid perovskite thin films," *The Journal of Physical Chemistry Letters*, vol. 9, no. 8, pp. 2015–2021, 2018.

[116] J. Schlipf, Y. Hu, S. Pratap, L. Bießmann, N. Hohn, L. Porcar, T. Bein, P. Docampo, and P. Muller-Buschbaum, "Shedding light on the moisture stability of 3d/2d hybrid perovskite heterojunction thin films," *ACS Applied Energy Materials*, vol. 2, no. 2, pp. 1011–1018, 2019.

[117] L. M. Matuana, J. J. Balatinecz, and C. B. Park, "Effect of surface properties on the adhesion between pvc and wood veneer laminates," *Polymer Engineering & Science*, vol. 38, no. 5, pp. 765–773, 1998.

[118] R. J. Good, "Contact angle, wetting, and adhesion: a critical review," *Journal of Adhesion Science and Technology*, vol. 6, no. 12, pp. 1269–1302, 1992.

[119] Z. Wu, M. Jiang, Z. Liu, A. Jamshaid, L. K. Ono, and Y. Qi, "Highly efficient perovskite solar cells enabled by multiple ligand passivation," *Advanced Energy Materials*, vol. 10, no. 10, p. 1903696, 2020.

[120] M. Saliba, K. W. Tan, H. Sai, D. T. Moore, T. Scott, W. Zhang, L. A. Estroff, U. Wiesner, and H. J. Snaith, "Influence of thermal processing protocol upon the crystallization and photovoltaic performance of organic–inorganic lead trihalide perovskites," *The Journal of Physical Chemistry C*, vol. 118, no. 30, pp. 17171–17177, 2014.

[121] K. W. Tan, D. T. Moore, M. Saliba, H. Sai, L. A. Estroff, T. Hanrath, H. J. Snaith, and U. Wiesner, "Thermally induced structural evolution and performance of mesoporous block copolymer-directed alumina perovskite solar cells," *ACS Nano*, vol. 8, no. 5, pp. 4730–4739, 2014.

[122] J. Schlipf and P. Müller-Buschbaum, "Structure of organometal halide perovskite films as determined with grazing-incidence x-ray scattering methods," *Advanced Energy Materials*, vol. 7, no. 16, p. 1700131, 2017.

[123] M. Birkholz, *Thin film analysis by X-ray scattering*. John Wiley & Sons, 2006.

[124] L. Oesinghaus, J. Schlipf, N. Giesbrecht, L. Song, Y. Hu, T. Bein, P. Docampo, and P. Müller-Buschbaum, "Toward tailored film morphologies: the origin of crystal orientation in hybrid perovskite thin films," *Advanced Materials Interfaces*, vol. 3, no. 19, p. 1600403, 2016.

[125] Y. Hu, J. Schlipf, M. Wussler, M. L. Petrus, W. Jaegermann, T. Bein, P. Muller-Buschbaum, and P. Docampo, "Hybrid perovskite/perovskite heterojunction solar cells," *ACS Nano*, vol. 10, no. 6, pp. 5999–6007, 2016.

[126] J. W. Jo, J. W. Jung, E. H. Jung, H. Ahn, T. J. Shin, and W. H. Jo, "Fluorination on both d and a units in d–a type conjugated copolymers based on difluorobithiophene and benzothiadiazole for highly efficient polymer solar cells," *Energy & Environmental Science*, vol. 8, no. 8, pp. 2427–2434, 2015.

[127] C.-H. Chiang, Z.-L. Tseng, and C.-G. Wu, "Planar heterojunction perovskite/pc 71 bm solar cells with enhanced open-circuit voltage via a (2/1)-step spin-coating process," *Journal of Materials Chemistry A*, vol. 2, no. 38, pp. 15897–15903, 2014.

[128] K. G. Stamplecoskie, J. S. Manser, and P. V. Kamat, "Dual nature of the excited state in organic–inorganic lead halide perovskites," *Energy & Environmental Science*, vol. 8, no. 1, pp. 208–215, 2015.

[129] Q. Chen, H. Zhou, T.-B. Song, S. Luo, Z. Hong, H.-S. Duan, L. Dou, Y. Liu, and Y. Yang, "Controllable self-induced passivation of hybrid lead iodide perovskites toward high performance solar cells," *Nano Letters*, vol. 14, no. 7, pp. 4158–4163, 2014.

[130] T. J. Jacobsson, J.-P. Correa-Baena, E. Halvani Anaraki, B. Philippe, S. D. Stranks, M. E. Bouduban, W. Tress, K. Schenk, J. Teuscher, J.-E. Moser, *et al.*, "Unreacted pbi2 as a double-edged sword for enhancing the performance of perovskite solar cells," *Journal of the American Chemical Society*, vol. 138, no. 32, pp. 10331–10343, 2016.

[131] D. Bi, W. Tress, M. I. Dar, P. Gao, J. Luo, C. Renevier, K. Schenk, A. Abate, F. Giordano, J.-P. Correa Baena, *et al.*, "Efficient luminescent solar cells based on tailored mixed-cation perovskites," *Science Advances*, vol. 2, no. 1, p. e1501170, 2016.

[132] J. Cao, X. Jing, J. Yan, C. Hu, R. Chen, J. Yin, J. Li, and N. Zheng, "Identifying the molecular structures of intermediates for optimizing the fabrication of high-quality perovskite films," *Journal of the American Chemical Society*, vol. 138, no. 31, pp. 9919–9926, 2016.

[133] A. Poglitsch and D. Weber, "Dynamic disorder in methylammoniumtrihalogeno-plumbates (ii) observed by millimeter-wave spectroscopy," *The Journal of Chemical Physics*, vol. 87, no. 11, pp. 6373–6378, 1987.

[134] Y. Kawamura, H. Mashiyama, and K. Hasebe, "Structural study on cubic-tetragonal transition of ch 3 nh 3 pbi 3," *Journal of the Physical Society of Japan*, vol. 71, no. 7, pp. 1694–1697, 2002.

[135] Q. Wang, M. Lyu, M. Zhang, J.-H. Yun, H. Chen, and L. Wang, "Transition from the tetragonal to cubic phase of organohalide perovskite: the role of chlorine in crystal formation of ch3nh3pbi3 on tio2 substrates," *The Journal of Physical Chemistry Letters*, vol. 6, no. 21, pp. 4379–4384, 2015.

[136] S. A. Kulkarni, T. Baikie, P. P. Boix, N. Yantara, N. Mathews, and S. Mhaisalkar, "Band-gap tuning of lead halide perovskites using a sequential deposition process," *Journal of Materials Chemistry A*, vol. 2, no. 24, pp. 9221–9225, 2014.

[137] Y. Zou, S. Yuan, A. Buyruk, J. Eichhorn, S. Yin, M. A. Reus, T. Xiao, S. Pratap, S. Liang, C. L. Weindl, *et al.*, "The influence of csbr on crystal orientation and optoelectronic properties of mapbi3-based solar cells," *ACS Applied Materials & Interfaces*, vol. 14, no. 2, pp. 2958–2967, 2022.

[138] C. H. Hendon, R. X. Yang, L. A. Burton, and A. Walsh, "Assessment of polyanion (bf 4- and pf 6-) substitutions in hybrid halide perovskites," *Journal of Materials Chemistry A*, vol. 3, no. 17, pp. 9067–9070, 2015.

[139] J. H. Heo, D. H. Song, and S. H. Im, "Planar ch3nh3pbbr3 hybrid solar cells with 10.4% power conversion efficiency, fabricated by controlled crystallization in the spin-coating process," *Advanced Materials*, vol. 26, no. 48, pp. 8179–8183, 2014.

[140] Q. Jiang, D. Rebollar, J. Gong, E. L. Piacentino, C. Zheng, and T. Xu, "Pseudohalide-induced moisture tolerance in perovskite ch3nh3pb (scn) 2i thin films," *Angewandte Chemie*, vol. 127, no. 26, pp. 7727–7730, 2015.

[141] N. Pellet, P. Gao, G. Gregori, T.-Y. Yang, M. K. Nazeeruddin, J. Maier, and M. Grätzel, "Mixed-organic-cation perovskite photovoltaics for enhanced solar-light harvesting," *Angewandte Chemie*, vol. 126, no. 12, pp. 3215–3221, 2014.

[142] Q. Lin, A. Armin, R. C. R. Nagiri, P. L. Burn, and P. Meredith, "Electro-optics of perovskite solar cells," *Nature Photonics*, vol. 9, no. 2, pp. 106–112, 2015.

[143] A. Miyata, A. Mitioglu, P. Plochocka, O. Portugall, J. T.-W. Wang, S. D. Stranks, H. J. Snaith, and R. J. Nicholas, "Direct measurement of the exciton binding energy and effective masses for charge carriers in organic–inorganic tri-halide perovskites," *Nature Physics*, vol. 11, no. 7, pp. 582–587, 2015.

[144] G. Giorgi, J.-I. Fujisawa, H. Segawa, and K. Yamashita, "Small photocarrier effective masses featuring ambipolar transport in methylammonium lead iodide perovskite: a density functional analysis," *The Journal of Physical Chemistry Letters*, vol. 4, no. 24, pp. 4213–4216, 2013.

[145] H. Min, D. Y. Lee, J. Kim, G. Kim, K. S. Lee, J. Kim, M. J. Paik, Y. K. Kim, K. S. Kim, M. G. Kim, *et al.*, "Perovskite solar cells with atomically coherent interlayers on sno2 electrodes," *Nature*, vol. 598, no. 7881, pp. 444–450, 2021.

[146] L. K. Reb, M. Böhmer, B. Predeschly, S. Grott, C. L. Weindl, G. I. Ivandekic, R. Guo, C. Dreißigacker, R. Gernhäuser, A. Meyer, *et al.*, "Perovskite and organic solar cells on a rocket flight," *Joule*, vol. 4, no. 9, pp. 1880–1892, 2020.

[147] L. K. Ono, S. Liu, and Y. Qi, "Reducing detrimental defects for high-performance metal halide perovskite solar cells," *Angewandte Chemie International Edition*, vol. 59, no. 17, pp. 6676–6698, 2020.

[148] C. Ran, J. Xu, W. Gao, C. Huang, and S. Dou, "Defects in metal triiodide perovskite materials towards high-performance solar cells: origin, impact, characterization, and engineering," *Chemical Society Reviews*, vol. 47, no. 12, pp. 4581–4610, 2018.

[149] M. I. Saidaminov, V. Adinolfi, R. Comin, A. L. Abdelhady, W. Peng, I. Dursun, M. Yuan, S. Hoogland, E. H. Sargent, and O. M. Bakr, "Planar-integrated single-crystalline perovskite photodetectors," *Nature Communications*, vol. 6, no. 1, pp. 1–7, 2015.

[150] J. Chen and N.-G. Park, "Materials and methods for interface engineering toward stable and efficient perovskite solar cells," *ACS Energy Letters*, vol. 5, no. 8, pp. 2742–2786, 2020.

[151] J. Wei, C. Shi, Y. Zhao, W. Zhou, H. Li, R. Fu, D. Yu, and Q. Zhao, "Potentials and challenges towards application of perovskite solar cells," *Science China Materials*, vol. 59, no. 9, pp. 769–778, 2016.

[152] Z. Xiao, Q. Dong, C. Bi, Y. Shao, Y. Yuan, and J. Huang, "Solvent annealing of perovskite-induced crystal growth for photovoltaic-device efficiency enhancement," *Advanced Materials*, vol. 26, no. 37, pp. 6503–6509, 2014.

[153] J. Schlipf, A. M. Askar, F. Pantle, B. D. Wiltshire, A. Sura, P. Schneider, L. Huber, K. Shankar, and P. Müller-Buschbaum, "Top-down approaches towards single crystal perovskite solar cells," *Scientific Reports*, vol. 8, no. 1, pp. 1–8, 2018.

[154] S. Pratap, J. Schlipf, L. Bießmann, and P. Muller-Buschbaum, "Hierarchical structures from nanocrystalline colloidal precursors within hybrid perovskite thin films: implications for photovoltaics," *ACS Applied Nano Materials*, vol. 3, no. 12, pp. 11701–11708, 2020.

[155] D. W. de Quilettes, S. M. Vorpahl, S. D. Stranks, H. Nagaoka, G. E. Eperon, M. E. Ziffer, H. J. Snaith, and D. S. Ginger, "Impact of microstructure on local carrier lifetime in perovskite solar cells," *Science*, vol. 348, no. 6235, pp. 683–686, 2015.

[156] N. Cho, F. Li, B. Turedi, L. Sinatra, S. P. Sarmah, M. R. Parida, M. I. Saidaminov, B. Murali, V. M. Burlakov, A. Goriely, *et al.*, "Pure crystal orientation and anisotropic charge transport in large-area hybrid perovskite films," *Nature Communications*, vol. 7, no. 1, pp. 1–11, 2016.

[157] K. Liu, L. Xie, P. Song, K. Lin, L. Shen, Y. Liang, J. Lu, W. Feng, X. Guan, C. Yan, *et al.*, "Stable perovskite solar cells enabled by simultaneous surface and bulk defects passivation," *Solar RRL*, vol. 4, no. 9, p. 2000224, 2020.

[158] L. A. Muscarella, E. M. Hutter, S. Sanchez, C. D. Dieleman, T. J. Savenije, A. Hagfeldt, M. Saliba, and B. Ehrler, "Crystal orientation and grain size: do they determine optoelectronic properties of mapbi3 perovskite?," *The Journal of Physical Chemistry Letters*, vol. 10, no. 20, pp. 6010–6018, 2019.

[159] C. Fei, L. Guo, B. Li, R. Zhang, H. Fu, J. Tian, and G. Cao, "Controlled growth of textured perovskite films towards high performance solar cells," *Nano Energy*, vol. 27, pp. 17–26, 2016.

[160] H. Mehdi, M. Matheron, A. Mhamdi, M. Manceau, C. Roux, S. Berson, S. Cros, and A. Bouazizi, "Correlation between efficiency and device characterization in mapbi3-xclx standard perovskite solar cells," *Journal of Materials Science: Materials in Electronics*, vol. 31, no. 13, pp. 10251–10259, 2020.

[161] X.-Y. Zhu, M.-W. Chen, B. Wang, N. Liu, M.-Q. Ran, H. Yang, and Y.-P. Yang, "Improved photovoltaic properties of nominal composition ch 3 nh 3 pb 0.99 zn 0.01 i 3 carbon-based perovskite solar cells," *Optics Express*, vol. 26, no. 26, pp. A984–A995, 2018.

[162] X. Zhang, X. Ren, B. Liu, R. Munir, X. Zhu, D. Yang, J. Li, Y. Liu, D.-M. Smilgies, R. Li, *et al.*, "Stable high efficiency two-dimensional perovskite solar cells via cesium doping," *Energy & Environmental Science*, vol. 10, no. 10, pp. 2095–2102, 2017.

[163] W. Rehman, D. P. McMeekin, J. B. Patel, R. L. Milot, M. B. Johnston, H. J. Snaith, and L. M. Herz, "Photovoltaic mixed-cation lead mixed-halide perovskites: links between crystallinity, photo-stability and electronic properties," *Energy & Environmental Science*, vol. 10, no. 1, pp. 361–369, 2017.

[164] B. Wang, X. Xiao, and T. Chen, "Perovskite photovoltaics: a high-efficiency newcomer to the solar cell family," *Nanoscale*, vol. 6, no. 21, pp. 12287–12297, 2014.

[165] A. Amat, E. Mosconi, E. Ronca, C. Quarti, P. Umari, M. K. Nazeeruddin, M. Gratzel, and F. De Angelis, "Cation-induced band-gap tuning in organohalide perovskites: interplay of spin–orbit coupling and octahedra tilting," *Nano Letters*, vol. 14, no. 6, pp. 3608–3616, 2014.

[166] C. Yi, J. Luo, S. Meloni, A. Boziki, N. Ashari-Astani, C. Grätzel, S. M. Zakeeruddin, U. Röthlisberger, and M. Grätzel, "Entropic stabilization of mixed a-cation abx 3 metal halide perovskites for high performance perovskite solar cells," *Energy & Environmental Science*, vol. 9, no. 2, pp. 656–662, 2016.

[167] Z. Wang, Q. Lin, F. P. Chmiel, N. Sakai, L. M. Herz, and H. J. Snaith, "Efficient ambient-air-stable solar cells with 2d–3d heterostructured butylammonium-caesium-formamidinium lead halide perovskites," *Nature Energy*, vol. 2, no. 9, pp. 1–10, 2017.

[168] D. H. Kim, J. Park, Z. Li, M. Yang, J.-S. Park, I. J. Park, J. Y. Kim, J. J. Berry, G. Rumbles, and K. Zhu, "300% enhancement of carrier mobility in uniaxial-oriented perovskite films formed by topotactic-oriented attachment," *Advanced Materials*, vol. 29, no. 23, p. 1606831, 2017.

[169] S. Liu, L. Wang, W.-C. Lin, S. Sucharitakul, C. Burda, and X. P. Gao, "Imaging the long transport lengths of photo-generated carriers in oriented perovskite films," *Nano Letters*, vol. 16, no. 12, pp. 7925–7929, 2016.

[170] A. Solanki, P. Yadav, S.-H. Turren-Cruz, S. S. Lim, M. Saliba, and T. C. Sum, "Cation influence on carrier dynamics in perovskite solar cells," *Nano Energy*, vol. 58, pp. 604–611, 2019.

[171] R. Li, P. Wang, B. Chen, X. Cui, Y. Ding, Y. Li, D. Zhang, Y. Zhao, and X. Zhang, "Nio x/spiro hole transport bilayers for stable perovskite solar cells with efficiency exceeding 21%," *ACS Energy Letters*, vol. 5, no. 1, pp. 79–86, 2019.

[172] M. A. Lampert, "Simplified theory of space-charge-limited currents in an insulator with traps," *Physical Review*, vol. 103, no. 6, p. 1648, 1956.

[173] W. Li, W. Zhang, S. Van Reenen, R. J. Sutton, J. Fan, A. A. Haghighirad, M. B. Johnston, L. Wang, and H. J. Snaith, "Enhanced uv-light stability of planar heterojunction perovskite solar cells with caesium bromide interface modification," *Energy & Environmental Science*, vol. 9, no. 2, pp. 490–498, 2016.

[174] J. Zhang, W. Liang, W. Yu, S. Yu, Y. Wu, X. Guo, S. Liu, and C. Li, "A two-stage annealing strategy for crystallization control of ch3nh3pbi3 films toward highly reproducible perovskite solar cells," *Small*, vol. 14, no. 26, p. 1800181, 2018.

[175] Y. Zou, J. Eichhorn, S. Rieger, Y. Zheng, S. Yuan, L. Wolz, L. V. Spanier, J. E. Heger, S. Yin, C. R. Everett, L. Dai, M. Schwartzkopf, C. Mu, S. V. Roth, I. D. Sharp, C. chao Chen, J. Feldmann, S. D. Stranks, and P. Müller-Buschbaum, "Ionic liquids tailoring crystal orientation and electronic properties for stable perovskite solar cells," *Nano Energy*, p. 108449, 2023.

[176] M. Jeong, I. W. Choi, E. M. Go, Y. Cho, M. Kim, B. Lee, S. Jeong, Y. Jo, H. W. Choi, J. Lee, *et al.*, "Stable perovskite solar cells with efficiency exceeding 24.8% and 0.3-v voltage loss," *Science*, vol. 369, no. 6511, pp. 1615–1620, 2020.

[177] J. Peng, F. Kremer, D. Walter, Y. Wu, Y. Ji, J. Xiang, W. Liu, T. Duong, H. Shen, T. Lu, *et al.*, "Centimetre-scale perovskite solar cells with fill factors of more than 86 per cent," *Nature*, vol. 601, no. 7894, pp. 573–578, 2022.

[178] N. Li, X. Niu, L. Li, H. Wang, Z. Huang, Y. Zhang, Y. Chen, X. Zhang, C. Zhu, H. Zai, *et al.*, "Liquid medium annealing for fabricating durable perovskite solar cells with improved reproducibility," *Science*, vol. 373, no. 6554, pp. 561–567, 2021.

[179] Y.-H. Lin, N. Sakai, P. Da, J. Wu, H. C. Sansom, A. J. Ramadan, S. Mahesh, J. Liu, R. D. Oliver, J. Lim, *et al.*, "A piperidinium salt stabilizes efficient metal-halide perovskite solar cells," *Science*, vol. 369, no. 6499, pp. 96–102, 2020.

[180] Y.-W. Jang, S. Lee, K. M. Yeom, K. Jeong, K. Choi, M. Choi, and J. H. Noh, "Intact 2d/3d halide junction perovskite solar cells via solid-phase in-plane growth," *Nature Energy*, vol. 6, no. 1, pp. 63–71, 2021.

[181] D. Luo, R. Su, W. Zhang, Q. Gong, and R. Zhu, "Minimizing non-radiative recombination losses in perovskite solar cells," *Nature Reviews Materials*, vol. 5, no. 1, pp. 44–60, 2020.

[182] X. Zhu, S. Yang, Y. Cao, L. Duan, M. Du, J. Feng, Y. Jiao, X. Jiang, Y. Sun, H. Wang, *et al.*, "Ionic-liquid-perovskite capping layer for stable 24.33%-efficient solar cell," *Advanced Energy Materials*, vol. 12, no. 6, p. 2103491, 2022.

[183] N. Aristidou, C. Eames, I. Sanchez-Molina, X. Bu, J. Kosco, M. S. Islam, and S. A. Haque, "Fast oxygen diffusion and iodide defects mediate oxygen-induced degradation of perovskite solar cells," *Nature Communications*, vol. 8, no. 1, pp. 1–10, 2017.

[184] D. Bryant, N. Aristidou, S. Pont, I. Sanchez-Molina, T. Chotchunangatchaval, S. Wheeler, J. R. Durrant, and S. A. Haque, "Light and oxygen induced degradation limits the operational stability of methylammonium lead triiodide perovskite solar cells," *Energy & Environmental Science*, vol. 9, no. 5, pp. 1655–1660, 2016.

[185] X. Liu, J. Min, Q. Chen, T. Liu, G. Qu, P. Xie, H. Xiao, J.-J. Liou, T. Park, and Z.-X. Xu, "Synergy effect of a π-conjugated ionic compound: Dual interfacial energy level regulation and passivation to promote voc and stability of planar perovskite solar cells," *Angewandte Chemie*, vol. 134, no. 11, p. e202117303, 2022.

[186] G. Yang, Z. Ren, K. Liu, M. Qin, W. Deng, H. Zhang, H. Wang, J. Liang, F. Ye, Q. Liang, *et al.*, "Stable and low-photovoltage-loss perovskite solar cells by multifunctional passivation," *Nature Photonics*, vol. 15, no. 9, pp. 681–689, 2021.

[187] Q. Yang, Z. Zhang, X.-G. Sun, Y.-S. Hu, H. Xing, and S. Dai, "Ionic liquids and derived materials for lithium and sodium batteries," *Chemical Society Reviews*, vol. 47, no. 6, pp. 2020–2064, 2018.

[188] R. Xia, Z. Fei, N. Drigo, F. D. Bobbink, Z. Huang, R. Jasiūnas, M. Franckevičius, V. Gulbinas, M. Mensi, X. Fang, *et al.*, "Retarding thermal degradation in hybrid perovskites by ionic liquid additives," *Advanced Functional Materials*, vol. 29, no. 22, p. 1902021, 2019.

[189] C. Liu, Y.-B. Cheng, and Z. Ge, "Understanding of perovskite crystal growth and film formation in scalable deposition processes," *Chemical Society Reviews*, vol. 49, no. 6, pp. 1653–1687, 2020.

[190] Z. Huang, X. Hu, C. Liu, L. Tan, and Y. Chen, "Nucleation and crystallization control via polyurethane to enhance the bendability of perovskite solar cells with excellent device performance," *Advanced Functional Materials*, vol. 27, no. 41, p. 1703061, 2017.

[191] T. A. Doherty, S. Nagane, D. J. Kubicki, Y.-K. Jung, D. N. Johnstone, A. N. Iqbal, D. Guo, K. Frohna, M. Danaie, E. M. Tennyson, *et al.*, "Stabilized tilted-octahedra halide perovskites inhibit local formation of performance-limiting phases," *Science*, vol. 374, no. 6575, pp. 1598–1605, 2021.

[192] H. Li, R. Zhang, Y. Li, Y. Li, H. Liu, J. Shi, H. Zhang, H. Wu, Y. Luo, D. Li, *et al.*, "Graphdiyne-based bulk heterojunction for efficient and moisture-stable planar perovskite solar cells," *Advanced Energy Materials*, vol. 8, no. 30, p. 1802012, 2018.

[193] M. Park, J.-Y. Kim, H. J. Son, C.-H. Lee, S. S. Jang, and M. J. Ko, "Low-temperature solution-processed li-doped sno2 as an effective electron transporting layer for high-performance flexible and wearable perovskite solar cells," *Nano Energy*, vol. 26, pp. 208–215, 2016.

[194] Y. W. Noh, J. H. Lee, I. S. Jin, S. H. Park, and J. W. Jung, "Tailored electronic properties of zr-doped sno2 nanoparticles for efficient planar perovskite solar cells with marginal hysteresis," *Nano Energy*, vol. 65, p. 104014, 2019.

[195] S. Zhang, H. Si, W. Fan, M. Shi, M. Li, C. Xu, Z. Zhang, Q. Liao, A. Sattar, Z. Kang, *et al.*, "Graphdiyne: bridging sno2 and perovskite in planar solar cells," *Angewandte Chemie*, vol. 132, no. 28, pp. 11670–11679, 2020.

[196] S. Nagane, S. Macpherson, M. A. Hope, D. J. Kubicki, W. Li, S. D. Verma, J. Ferrer Orri, Y.-H. Chiang, J. L. MacManus-Driscoll, C. P. Grey, *et al.*, "Tetrafluoroborate-induced reduction in defect density in hybrid perovskites through halide management," *Advanced Materials*, vol. 33, no. 32, p. 2102462, 2021.

[197] L. Liang, H. Luo, J. Hu, H. Li, and P. Gao, "Efficient perovskite solar cells by reducing interface-mediated recombination: a bulky amine approach," *Advanced Energy Materials*, vol. 10, no. 14, p. 2000197, 2020.

[198] W. Zhang, Z. Lin, Q. Cai, X. Xu, H. Dong, C. Mu, and J.-P. Zhang, "Electron transport assisted by transparent conductive oxide elements in perovskite solar cells," *ChemSusChem*, vol. 15, no. 3, p. e202102002, 2022.

[199] R. Gottesman, P. Lopez-Varo, L. Gouda, J. A. Jimenez-Tejada, J. Hu, S. Tirosh, A. Zaban, and J. Bisquert, "Dynamic phenomena at perovskite/electron-selective contact interface as interpreted from photovoltage decays," *Chem*, vol. 1, no. 5, pp. 776–789, 2016.

[200] T. Bu, X. Liu, Y. Zhou, J. Yi, X. Huang, L. Luo, J. Xiao, Z. Ku, Y. Peng, F. Huang, *et al.*, "A novel quadruple-cation absorber for universal hysteresis elimination for high efficiency and stable perovskite solar cells," *Energy & Environmental Science*, vol. 10, no. 12, pp. 2509–2515, 2017.

[201] J. Siekmann, S. Ravishankar, and T. Kirchartz, "Apparent defect densities in halide perovskite thin films and single crystals," *ACS Energy Letters*, vol. 6, no. 9, pp. 3244–3251, 2021.

[202] J. Hu, R. Gottesman, L. Gouda, A. Kama, M. Priel, S. Tirosh, J. Bisquert, and A. Zaban, "Photovoltage behavior in perovskite solar cells under light-soaking showing photoinduced interfacial changes," *ACS Energy Letters*, vol. 2, no. 5, pp. 950–956, 2017.

[203] R. Bertoluzzi, L. L. Sanchez, and L. J-W, "E. mas-marza, h. han, n.-g. park, i. mora-sero, and j. bisquert," *Energy Environ. Sci*, vol. 8, p. 910, 2015.

[204] A. Walsh, D. O. Scanlon, S. Chen, X. Gong, and S.-H. Wei, "Self-regulation mechanism for charged point defects in hybrid halide perovskites," *Angewandte Chemie*, vol. 127, no. 6, pp. 1811–1814, 2015.

[205] V. Roiati, S. Colella, G. Lerario, and L. De Marco, "a. rizzo, a. listorti and g. gigli," *Energy Environ. Sci*, vol. 7, p. 1889, 2014.

[206] S. Sinha, E. Sirota, Garoff, S, and H. Stanley, "X-ray and neutron scattering from rough surfaces," *Physical Review B*, vol. 38, no. 4, p. 2297, 1988.

[207] G. Renaud, R. Lazzari, and F. Leroy, "Probing surface and interface morphology with grazing incidence small angle x-ray scattering," *Surface Science Reports*, vol. 64, no. 8, pp. 255–380, 2009.

[208] J. Schlipf, P. Docampo, C. J. Schaffer, V. Korstgens, L. Bießmann, F. Hanusch, N. Giesbrecht, S. Bernstorff, T. Bein, and P. Muller-Buschbaum, "A closer look into two-step perovskite conversion with x-ray scattering," *The Journal of Physical Chemistry Letters*, vol. 6, no. 7, pp. 1265–1269, 2015.

[209] R. Guo, D. Han, W. Chen, L. Dai, K. Ji, Q. Xiong, S. Li, L. K. Reb, M. A. Scheel, S. Pratap, *et al.*, "Degradation mechanisms of perovskite solar cells under vacuum and one atmosphere of nitrogen," *Nature Energy*, vol. 6, no. 10, pp. 977–986, 2021.

[210] Z. Andaji-Garmaroudi, M. Anaya, A. J. Pearson, and S. D. Stranks, "Photobrightening in lead halide perovskites: observations, mechanisms, and future potential," *Advanced Energy Materials*, vol. 10, no. 13, p. 1903109, 2020.

[211] S. Macpherson, T. A. Doherty, A. J. Winchester, S. Kosar, D. N. Johnstone, Y.-H. Chiang, K. Galkowski, M. Anaya, K. Frohna, A. N. Iqbal, *et al.*, "Local nanoscale phase impurities are degradation sites in halide perovskites," *Nature*, pp. 1–3, 2022.

[212] D. W. DeQuilettes, W. Zhang, V. M. Burlakov, D. J. Graham, T. Leijtens, A. Osherov, V. Bulović, H. J. Snaith, D. S. Ginger, and S. D. Stranks, "Photo-induced halide redistribution in organic–inorganic perovskite films," *Nature Communications*, vol. 7, no. 1, pp. 1–9, 2016.

[213] J. S. Godding, A. J. Ramadan, Y.-H. Lin, K. Schutt, H. J. Snaith, and B. Wenger, "Oxidative passivation of metal halide perovskites," *Joule*, vol. 3, no. 11, pp. 2716–2731, 2019.

[214] S. Mahesh, J. M. Ball, R. D. Oliver, D. P. McMeekin, P. K. Nayak, M. B. Johnston, and H. J. Snaith, "Revealing the origin of voltage loss in mixed-halide perovskite solar cells," *Energy & Environmental Science*, vol. 13, no. 1, pp. 258–267, 2020.

List of publications

Publications related to the dissertation

- Y. Zou, R. Guo, A. Buyruk, W. Chen, T. Xiao, S. Yin, X. Jiang, L. P. Kreuzer,C. Mu, T. Ameri, M. Schwartzkopf,S. V. Roth, P. Müller-Buschbaum, "Sodium Dodecylbenzene Sulfonate Interface Modification of Methylammonium Lead Iodide for Surface Passivation of Perovskite Solar Cells."*ACS Appl. Mater. Interfaces*, vol.12, pp. 52643–52651, 2021.
- Y. Zou, S. Yuan, A. Buyruk, J. Eichhorn, S. Yin, M. A. Reus, T. Xiao, S. Pratap, S. Liang, C. L. Weindl, W. Chen, C. Mu, I. D. Sharp, T. Ameri, M. Schwartzkopf, S. V. Roth, P. Müller-Buschbaum " The Influence of CsBr on Crystal Orientation and Optoelectronic Properties of MAPbI3-Based Solar Cells" *ACS Appl. Mater. Interfaces*, vol. 14, pp.2958-2967, 2022.
- Y. Zou, J. Eichhorn, S. Rieger, Y. Zheng, S.Yuan, L.Wolz, L. V. Spanier, J. E. Heger, S Yin, C. R. Everett, L. Dai, M. Schwartzkopf, C. Mu, S. V. Roth, I. D. Sharp, C. Chen, J. Feldmann, S. D. Stranks, P. Müller-Buschbaum,"Ionic liquids tailoring crystal orientation and electronic properties for stable perovskite solar cells " *Nano Energy*, 108449, 2023.

Further publications

- S. Yin, Y. Zou, M. A. Reus, X. Jiang, S. Tu, T. Tian, R. Qi, Z. Xu, S. Liang, Y. Cheng, J. E. Heger, M. Schwartzkopf, S. V. Roth, P. Müller-Buschbaum,"Tailored Fabrication of Quasi-Isoporous and Double Layered α-Fe_2O_3 Thin Films and Their Application in Photovoltaic Devices"*Chem. Eng. J.*, pp. 455, 2023.
- G. Shen, X. Lin, Y. Zou, H. Dong, D. Zhu, Y. Jiang, X. Ng, F. Lin, P. Müller-Buschbaum, C. Mu,"High-performance and Large-area Inverted Perovskite Solar Cells based on NiOx Films Enabled with A Novel Microstructure-Control Technology"*Energy Environ. Mater.*, pp. e12504, 2022.

- H. Dong, G. Shen, Y. Zou, Y. Li, Z. Lin, Q. Cai, X. Xu, Q. Song, H. Duan, P. Müller-Buschbaum, C. Mu,"Synergistic Defect Passivation by Metformin Halides for Improving Perovskite Solar Cell Performance"*J. Phys. Chem.*, 2023.

Scientific reports

- Y. Zou, R. Guo, A. Buyruk, W. Chen, T. Xiao, S. Yin, X. Jiang, L. P. Kreuzer,C. Mu, T. Ameri, M. Schwartzkopf, S. V. Roth, P. Müller-Buschbaum, "Sodium Dodecylbenzene Sulfonate Interface Modification of Methylammonium Lead Iodide for Surface Passivation of Perovskite Solar Cells", *CeNS, Annual Report*, 2020.
- Y. Zou, S. Yin, R. Guo, P. Müller-Buschbaum "Surfactant for surface-defect passivation of perovskite solar cells", *Lehrstuhl für Funktionelle Materialien, Annual Report*, 2020.
- Y. Zou, P. Müller-Buschbaum "The effect of the CsBr-doping on the crystal orientation and optoelectronic properties of perovskite film", *Lehrstuhl für Funktionelle Materialien, Annual Report*, 2021.
- Y. Zou, S Yin, L. V. Spanier, J. E. Heger, C. R. Everett, P. Müller-Buschbaum, "The role of ionic liquid additives in crystal orientation and photovoltaic properties in perovskite solar cells", *Lehrstuhl für Funktionelle Materialien, Annual Report*, 2022.

Conference talks

-

Conference poster presentations

- Y. Zou, P. Müller-Buschbaum, "The effect of surfactant doping on the crystallization kinetics and stability of perovskite solar cells", Virtual DPG Spring Meeting 2020, 15-20 March, 2020.
- Y. Zou, B. Ali, W. Chen, T. Xiao, S.Yin, L. P. Kreuzer, C. Mu, T. Amerib, M. Schwartzkopf, S. V. Roth, P. Müller-Buschbaum, "Sodium dodecylbenzene sulfonate interface modification of methylammonium lead iodide as surface passivation of perovskite solar cells", 10th Energy Colloquium of the Munich School of Engineering, 30 July, Garching, Germany, 2020.

- Y. Zou, M. E. Scheel, R Guo, T. Xiao, S. Pratap, B. Ali, S.Yin, C. Mu, T. Amerib, M. Schwartzkopf, S. V. Roth P. Müller-Buschbaum, "Compositional engineering for high performance perovskite solar cells via Cs doping", MLZ User Meeting, Garching, Germany, 2020.
- Y. Zou, M. E. Scheel, T. Xiao, S. Pratap, B. Ali, S.Yin, C. Mu, T. Amerib, M. Schwartzkopf, S. V. Roth P. Müller-Buschbaum, "The Role of CsBr in Crystal Orientation and Optoelectronic Properties of $MAPbI_3$-based devices", Virtual DPG Spring Meeting 2021, 22-24 March, 2021.
- Y. Zou, M. E. Scheel, T. Xiao, S. Pratap, B. Ali, S.Yin, L. P. Kreuzer, C. Mu, T. Amerib, M. Schwartzkopf, S. V. Roth P. Müller-Buschbaum, "Compositional engineering for high performance perovskite solar cells via Cs doping" 11th Energy Colloquium of the Munich School of Engineering, 26 July, Garching, Germany, 2021
- Y. Zou, M. E. Scheel, T. Xiao, S. Pratap, B. Ali, S.Yin, L. P. Kreuzer, C. Mu, T. Amerib, M. Schwartzkopf, S. V. Roth P. Müller-Buschbaum, "The Role of CsBr in Crystal Orientation and Optoelectronic Properties of $MAPbI_3$-based devices", Virtual DPG SKM21 Meeting 2021, September 27th to October 1st 2021,
- Y. Zou, S. Yuan, B. Ali, J, Eichhorn, S. Yin, M. Scheel, T. Xiao, S. Pratap, S. Liang, C. L. Weindl, W. Chen, C. Mu, I. D. Sharp, T. Amerib, M. Schwartzkopf, S. V. Roth P. Müller-Buschbaum, "The Influence of CsBr on Crystal Orientation and Optoelectronic Properties of $MAPbI_3$-based Solar Cells", MLZ User Meeting, 7-8 December, Germany, 2021.
- Y. Zou, P. Müller-Buschbaum, "Effect of ionic liquids on crystallization, charge carrier dynamics and stability of perovskite solar cells" 12th Energy Colloquium of the Munich School of Engineering, 28 July, Garching, Germany, 2022.
- Y. Zou, P. Müller-Buschbaum, "Ionic liquids tailoring crystal orientation and electronic properties for stable and high fill factor perovskite solar cells", DPG Meeting in Regensburg, 4-9 September, Germany, 2022.
- Y. Zou, P. Müller-Buschbaum, "Ionic liquids tailoring crystal orientation and electronic properties for stable and high fill factor perovskite solar cells", MLZ User Meeting, 8-9 December, Germany, 2022.
- Y. Zou, P. Müller-Buschbaum, "Active layer aging for the fabricating durable perovskite solar cells with improved reproducibility ", DESY Photon Science Users´ Meeting, 26-27 January, Germany, 2023.

- Y. Zou, P. Müller-Buschbaum, "A general approach towards highly reproducible and high-quality perovskite films based on an aging treatment", DPG-Frühjahrstagung Dresden 2023 (SKM23), 26-31 March, Germany, 2023.

Acknowledgments

It's great pleasure for me to complete my Ph.D. studies at the Chair of Functional Materials, a.k.a. E13, Technical University of Munich (TUM), in Germany. During my Ph.D. study, I owe many interesting travel experiences, met many humorous and smart friends, tasted many delicious foods from all over the world, met local customs from different regions and countries, and also saw many fascinating and beautiful mountains and lakes. What I saw, heard, and tasted broadened my knowledge and enriched my experience, it was a valuable learning experience. Of course, it is necessary for me to express gratitude to those who contributed to this work at the end of my thesis.

First, I would like to thank my supervisor Prof. Dr. Peter Muller-Buschbaum for allowing me to join the Chair of Functional Materials, for providing materials to me to complete my experiment design and for organizing my Ph.D. defense, very thanks for his help during my Ph.D. study.

Second, I am very grateful for the financial support provided by the China Scholarship Council (CSC), which gave me the opportunity to come to Germany for my Ph.D. study and support the cost of living in Germany, allowing me to devote myself to my Ph.D. study.

Third, I am grateful to Prof. Dr. Jianping Zhang (Renmin University of China) and Prof. Dr. Chun-Chao Chen (Shanghai JiaoTong university) from China. They provided many valuable insights into experimental design and gave great help and support in experiment characterizations (TPC, TPV, OCVD, XPS, UPS, PL, TRPL, EQE section), as well as professional data analysis techniques, which refined the experimental protocol and enriched my Ph.D. experience. In addition, I also want to thank Shuai Yuan (from RUC) and Yiting Zheng (From SJTU) for their great help in the characterization measurement, which is very important in my work.

Fourth, I would like to thank Prof. Dr. Samuel D. Stranks and Dr. Linjie Dai from the University of Cambridge, UK. Very thanks for their great help in TAS measurement, which is an essential part of our work. They are very kind-hearted and important collaborators.

Fifth, I would like to thank Prof. Dr. Ian D. Sharp, Dr. Johanna Eichhorn, and Wolz Lukas from WSI in TUM, Germany. Very thanks for their great help in XPS and UPS measurement. I learned the professional analysis of XPS and UPS data from them , which will be very useful and valuable for my future study, not limited to the previous work.

Sixth, I would like to thank Prof. Dr. Jochen Feldmann and Dr. Sebastian Rieger from LMU. Germany. Very thanks for their great help and professional data analysis on PL, TRPL, and TAS. With their contributions, I could successfully collect experimental data and complete the experiment design, which is very important for our work.

I would like to thank Prof. Dr. Tayebeh Ameri and Ali Buyruk from LMU, Germany. Very thanks for the great help in PL/TRPL and EQE measurement. They are very nice and kind-hearted collaborators.

I would like to thank Prof. Dr. Stephan V. Roth and Dr. Matthias Schwartzkopf, the beamline scientists at DESY (Hamburg, Germany). They provided me access to learning and operating the synchrotron-based large facility. Without their great contributions and great support, I can't successfully collect the GIWAXS and GISAXS data, which is important and highlighted part of the present thesis.

I enjoyed working with my colleagues who highly supported me at the beamtime. Here, I want to thank Simon J. Schaper, Julian E. Heger, Apostolos Vagias, Manuel E. Scheel, Marc Gensch, and Lukas V. Spanier for their kind help, extreme patience, and nice discussion, as well as teach me how to measure GIWAXS and GISAXS and how to process and analysis GIWAXS and GISAXS data. They are very nice and important team members. I am very happy to have and work with the team member, with whom I spent a wonderful and unforgettable time.

I am very thanks to Dr. Shanshan Yin, Julian E. Heger, Zerui Li, Guangjiu Pan, and Jinsheng Zhang for revising my PhD thesis and the proposing valuable suggestions. Appreciating the help and contribution from them.

I am thankful for the help from my bachelor's student Samuel Reiser during my Ph.D. study period. He is a very smart and diligent student with strong experimental operation ability, which provide lots of valuable data for our experiment. Very thanks for his contributions, is an essential part of our work.

Simultaneously, I appreciate the help and contributions of the internal group members. First, I would like to thank Prof. Dr. Christine Papadakis to be my mentor. Second, I want to thank Dr. Florian Jung for the help with the Contact-angle measurement. Third, I want to thank Shanshan Yin for the help in SEM measurement, Everett Christopher and Zerui Li for the help in AFM, Suzhe Liang for the help in the Blender operation, Julian E. Heger for the GIWAXS/GISAXS analysis, Lucas P. Kreuzer and Julija Reitenbach for

the help in FTIR measurement, Christina Geiger and Christopher R. Everett for the help in XRD, Dominik. Schwaiger for the help with the computer, Tianle Zheng for the help in EIS fitting, Yanan Li and Guangjiu Pan for the help in GIWAXS/GISAXS, and Weindl Christian for the help in SEM-EDS.

Besides, very thanks all other kind colleagues from E13, I enjoyed the wonderful time with them and the nice and friendly atmosphere in our group.

I am sincerely grateful that our secretaries Marion Waletzki and Carola Kappauf gave me so much help during my Ph.D. period, including experimental materials purchase, reimbursements, and organize many activities such as summer school, hiking, and so on.

Last but not least, I would like to thank my parents and my friends. They highly support me to pursue my dream and watch me move forward step by step. Their love and encouragements drive me to become better in both work and daily life.